Computer-Based Estimation of Circulating Blood Volume from Ultrasound Imagery

by

©Ebrahim Karami

A thesis submitted to the School of Graduate Studies in partial fulfillment of the requirements for the degree of

Doctor of Philosophy

Faculty of Engineering and Applied Science
Memorial University of Newfoundland

Memorial University of Newfoundland

October 2019

St. John's Newfoundland and Labrador

Abstract

Detection of relative changes in circulating blood volume is important to guide resuscitation and manage a variety of medical conditions including sepsis, trauma, dialysis and congestive heart failure. In recent years, ultrasound images of inferior vena cava (IVC) and internal jugular vein (IJV) have been used to assess volume status and guide fluid administration. This approach has limitations in that a skilled operator must perform repeated measurements over time.

In this dissertation, we develop semi-automatic image processing algorithms for estimation and tracking of the IVC anterior-posterior (AP)-diameter and IJV cross-sectional area in ultrasound videos. The proposed algorithms are based on active contours (ACs), where either the IVC AP-diameter or IJV CSA is estimated by minimization of an energy functional.

More specifically, in chapter 2, we propose a novel energy functional based on the third centralized moment and show that it outperforms the functionals that are traditionally used with active contours (ACs). We combine the proposed functional with the polar contour representation and use it for segmentation of the IVC.

In chapters 3 and 4, we propose active shape models based on ellipse; circle; and rectangles fitted inside the IVC as efficient, consistent and novel approaches to tracking and approximating the anterior-posterior (AP)-diameter even in the context of poor quality images. The proposed algorithms are based on a novel heuristic evolution functional that works very well with ultrasound images. In chapter 3, we show that the proposed active circle algorithm accurately, estimates the IVC AP-diameter. Although the estimated AP-diameter is very close to its actual value, the clinicians define the IVC AP-diameter as the largest vertical diameter of the IVC contour which deviates from its actual definition. To solve this problem and estimate the AP-diameter in the same way as its clinical definition, in chapter 4, we propose the active rectangle algorithm, where clinically measured AP-diameter is modeled as the height of a vertical thin rectangle. The results show that the AP-diameter estimated by the active rectangle algorithm is closer to its clinically measurement than the active circle and active ellipse algorithms.

In chapter 5, we propose a novel adaptive polar active contour (Ad-PAC) algorithm for the segmentation and tracking of the IJV in ultrasound videos. In the proposed algorithm, the parameters of the Ad-PAC algorithm are adapted based on the results of segmentation in previous frames. The Ad-PAC algorithm has been applied to 65 ultrasound videos and shown to be a significant improvement over existing segmentation algorithms.

So far, all proposed algorithms are semi-automatic as they need an operator to either locate the vessel in the first frame, or manually segment the first first and work automatically for the next frames. In chapter 6, we proposed a novel algorithm to automatically locate the vessel in ultrasound videos. The proposed algorithm is based on convolutional neural networks (CNNs) and is trained and applied for IJV videos. In this chapter we show that although the proposed algorithm is trained for data acquired from healthy subjects, it works efficiently for the data collected from coronary heart failure (CHF) patients without additional training.

Finally, conclusions are drawn and possible extensions are discussed in chapter 7.

Acknowledgements

I would like to offer my sincere thanks to my supervisors Dr. Andrew J. Smith and Dr. Mohamed S. Shehata for their valuable guidance, dedication, and encouragement. I would like to thank my family for their kind and unconditional support.

Co-authorship Statement

I, Ebrahim Karami, have the principal author status for all manuscripts included in this thesis. However, all manuscripts in this work are co-authored by my supervisors who have made valuable contributions which facilitated the development of this work. The list of the peer-reviewed manuscripts included in this dissertation are described as below.

1. Ebrahim Karami, Mohamed S. Shehata, and Andrew J. Smith, "Automatic Localization of the Internal Jugular Vein in Ultrasound Imagery Using 3-D CNNs," *submitted to Computers in Biology and Medicine*, June 2019.

2. Ebrahim Karami, Mohamed S. Shehata, and Andrew J. Smith, "Adaptive Polar Active Contour for Segmentation and Tracking in Ultrasound Videos," *IEEE Trans. on Circuit and Systems in Video Technology* , vol. 29, no. 4, pp. 1209-1222, April 2019.

3. Ebrahim Karami, Mohamed S. Shehata, and Andrew J. Smith, "Semi-automatic Algorithms for Estimation and Tracking of AP-diameter of the IVC in Ultrasound images," *Journal of Imaging*, vol. 5, no. 1, pp. 1-14, January 2019.

4. Ebrahim Karami, Mohamed S. Shehata, and Andrew J. Smith, "Estimation and Tracking of AP-diameter of the Inferior Vena Cava in Ultrasound Images Using

a Novel Active Circle Algorithm," *Computers in Biology and Medicine*, vol. 98, pp. 16-25, July 2018.

5. Ebrahim Karami, Mohamed S. Shehata, and Andrew J. Smith, "Segmentation and Tracking of Inferior Vena Cava in Ultrasound Images Using a Novel Polar Active Contour Algorithm," *in Proc. IEEE Global Conference on Signal and Information Processing (GlobalSIP)*, pp. 745-749, November 14-16, 2017.
6. Ebrahim Karami, Mohamed S. Shehata, and Andrew J. Smith, "Tracking of the Internal Jugular Vein in Ultrasound Images Using Optical Flow," *in Proc. Canadian Conference on Electrical and Computer Engineering (CCECE)*, pp. 1-4, April 30-May 3, 2017.
7. Ebrahim Karami, Mohamed S. Shehata, Peter McGuire, and Andrew J. Smith, "A Semi-automated Technique for Internal Jugular Vein Segmentation in Ultrasound Images Using Active Contours," *in Proc. IEEE-EMBS International Conference on Biomedical and Health Informatics (BHI)*, pp. 1-4, February 16-19, 2016.
8. Ebrahim Karami, Mohamed S. Shehata, and Andrew J. Smith, "Ultrasound Image Segmentation Techniques for Tracking and Measurement of the Internal Jugular Vein," *The 24th Annual Newfoundland Electrical and Computer Engineering Conference (NECEC)*, November 16, 2015.
9. Ebrahim Karami, Mohamed S. Shehata, and Andrew J. Smith, "Image Identification Using SIFT Algorithm: Performance Analysis against Different Image Deformations," *The 24th Annual Newfoundland Electrical and Computer Engineering Conference (NECEC)*, November 16, 2015.
10. Ebrahim Karami, Siva Prasad, and Mohamed S. Shehata, "Image Matching

Using SIFT, SURF, BRIEF and ORB: Performance Comparison for Distorted Images," *The 24th Annual Newfoundland Electrical and Computer Engineering Conference (NECEC)*, November 16, 2015.

Table of Contents

Abstract iii

Acknowledgments iv

Table of Contents xii

List of Tables xiii

List of Figures xix

List of Abbreviations xx

1 Introduction 1

- 1.1 Research Motivation 1
- 1.2 Research Objective 2
- 1.3 Thesis Structure 2
- 1.4 Contributions 3
- References 6

2 Segmentation and Tracking of IVC in Ultrasound Images Using a Novel Polar Active Contour 8

- 2.1 Introduction 8

2.2 Background and Related work 10
    2.2.1 IVC Image Structure 10
    2.2.2 Energy and Evolution Functionals 11
2.3 Proposed Algorithm 13
    2.3.1 Proposed Energy Functional 13
    2.3.2 Proposed Algorithm 16
2.4 Results 17
2.5 Conclusion 19
References 21

3 Estimation and Tracking of the IVC AP-diameter Using a Novel Active Circle Algorithm 25

3.1 Introduction 26
3.2 Background and Related work 28
    3.2.1 IVC Image 28
    3.2.2 Energy and Evolution Functionals 29
3.3 Proposed Algorithm 31
    3.3.1 Why a Circular Model? 31
    3.3.2 Proposed Evolution Functional 32
    3.3.3 Circle Evolution 34
    3.3.4 Proposed Active Circle Algorithm 38
    3.3.5 Complexity Analysis 38
3.4 Results 40
    3.4.1 Comparison of the proposed functional with state-of-the-art functionals 41
    3.4.2 Influence of the parameter α on the accuracy of the proposed algorithm 41

3.4.3 comparison of the proposed algorithm with state-of-the-art segmentation algorithms 42
3.4.4 More Comparison Metrics 45
3.4.5 Influence of speckle removal filtering on the performance of the proposed algorithm 47
3.5 Conclusion 49
References 50

4 Estimation and Tracking of the IVC AP-diameter Using Active Shape Models 55

4.1 Introduction 56
4.2 Background and Related Work 58
4.3 Proposed Algorithms 59
4.3.1 Active Ellipse Model 60
4.3.2 Active Rectangle Model 63
4.4 Results 66
4.4.1 Tracking Performance 68
4.5 Discussion 76
4.5.1 The Performance of the Proposed Algorithms 76
4.5.2 Complexity Comparison 77
4.6 Conclusions 77
References 79

5 Segmentation and Tracking of the IJV 84

5.1 Introduction 85
5.2 Related Work 90
5.3 The Proposed Algorithm: Adaptive Polar AC (Ad-PAC) 93

5.3.1 The Energy Functional 94

5.3.2 Local Parameterization of the Energy Functional 96

5.3.2.1 Overview 96

5.3.2.2 Energy Functionals in Polar Coordinates 98

5.3.3 Parameter Adaptation 102

5.4 Implementation of The Ad-PAC Algorithm 107

5.5 Results 109

5.5.1 Evaluation of Extraction 110

5.5.2 Influence of Initial Parameter Selection on the Performance of Ad-PAC 111

5.5.3 Influence of Contour Points Spacing 113

5.5.4 Tracking Performance 114

5.5.5 Influence of Image Quality 116

5.5.6 Influence of IJV Shape 117

5.5.7 Influence of IJV Variation 121

5.6 Conclusion and Future Work 121

References 127

6 Localization of the IJV in Ultrasound Videos Using Deep Learning 136

6.1 Introduction 137

6.2 The Architecture of the Proposed 3D CNNs 141

6.2.1 Layers Used to Built The Proposed 3D CNN 141

6.2.2 3D CNNs Architecture 143

6.3 Data Preparation and Training of the CNNs 146

6.3.1 Data Preparation 147

6.3.2 Training the Implemented Models 150

6.4 The Proposed Algorithm 150

6.5 Results and Discussion 152
6.5.1 Classification Accuracy 152
6.5.2 Performance of the Proposed Algorithm 153
6.6 Conclusion and Future Work 161
References 162

7 Overall Conclusions **166**

List of Tables

3.1 RMS of the AP-diameter estimation error obtained using the proposed algorithm and seven other methods. 45
3.2 Summary of the results of eight studied IVC videos. 47
3.3 RMS of error obtained from the proposed algorithm with different speckle removal filters. 49

4.1 RMS of the AP-diameter estimation error. 74
4.2 Maximum absolute value of AP-diameter estimation error. 74
4.3 Correlation between the AP-diameters estimated by the three shape-based algorithms and manual measurement. 75
4.4 The average position error for the three shape-based algorithms w.r.t. the manual measurement. 76

6.1 The average classification accuracy for the healthy and CHF subjects. 153
6.2 The average classification accuracy metric for the healthy and CHF subjects. 154

List of Figures

2.1 A typical ultrasound image of IVC. 11

2.2 PDF of the intensity levels inside the disks concentric with the IVC with radius equal to (a): 80%, (b): 100%, and (c): 120% of the IVC. . 12

2.3 E_{M3} inside a circular contour C versus the normalized radius with $\alpha = 1$. 15

2.4 Tracking of the IVC for manual segmentation, proposed algorithm and four other algorithms. 18

2.5 IVC area (Fig 1.) as measured by the proposed algorithm, manual segmentation, and four other algorithms. 19

2.6 IVC area as estimated by the proposed algorithm, manual segmentation, and four other algorithms. 20

3.1 A typical ultrasound image of IVC with circle evolution model. 29

3.2 PDF of the intensity levels inside the disks concentric with the IVC (see Fig. 3.1) with radius equal to (a): 75%, (b): 100%, and (c): 150% of the IVC AP-diameter. 30

3.3 Estimation of AP-diameter using circle fitting in IVC images with different shapes and qualities. 33

3.4 Proposed evolution functional versus (a)- δx, (b)- δy, and (c)- normalized circle diameter D/D_{AP} with $\alpha = 10^{-3}$. 35

3.5 The forces generated by the evolution functional in (3.7) with $\alpha = 0.05$ and $K = 8$ (values are adjusted for illustration purposes). 36

3.6 Flowchart of the proposed active-circle algorithm. 39

3.7 First frame of three sample IVC videos rated as (a)- good, (b)- average, and (c)- poor quality videos. 40

3.8 IVC diameter of a typical IVC video as measured by the proposed functional and two functionals in equations (3.4) and (3.6). 42

3.9 The RMS of error for the proposed algorithm w.r.t. the parameter α for the three sample videos depicted in Fig. 3.7. 43

3.10 AP-diameter for the three samples videos depicted in Fig. 3.7, as measured by the proposed algorithm, manual extraction, and four other algorithms. 44

3.11 Estimated AP-diameter versus the type of speckle removal filter. . . . 48

4.1 Flowchart for the proposed active ellipse algorithm for estimation and tracking of the IVC AP-diameter from ultrasound videos. 62

4.2 The ellipse evolution versus number of iterations. 63

4.3 Flowchart for the proposed active rectangle algorithm for estimation and tracking of the IVC AP-diameter from ultrasound videos. 65

4.4 The rectangle evolution versus number of iterations. 66

4.5 The first frame of all eight IVC videos. 67

4.6 AP-diameter for the first video depicted in Fig. 4.5, as measured by the manual measurement (red line), active circle algorithm (black line), active ellipse algorithm (green line) and active rectangle algorithm (blue line). 68

4.7 AP-diameter for the second video depicted in Fig. 4.5, as measured by the manual measurement (red line), active circle algorithm (black line), active ellipse algorithm (green line) and active rectangle algorithm (blue line). 69

4.8 AP-diameter for the third sample video depicted in Fig. 4.5, as measured by the manual measurement (red line), active circle algorithm (black line), active ellipse algorithm (green line) and active rectangle algorithm (blue line). 70

4.9 PDF of the AP-diameter estimation error w.r.t. manual measurement for the first sample video depicted in Fig. 4.5, as measured by active circle algorithm (black line), active ellipse algorithm (red line) and active rectangle algorithm (green line). 71

4.10 PDF of the AP-diameter estimation error w.r.t. manual measurement for the second sample video depicted in Fig. 4.5, as measured by active circle algorithm (black line), active ellipse algorithm (red line) and active rectangle algorithm (green line). 72

4.11 PDF of the AP-diameter estimation error w.r.t. manual measurement for the third sample video depicted in Fig. 4.5, as measured by active circle algorithm (black line), active ellipse algorithm (red line) and active rectangle algorithm (green line). 73

5.1 Sample images for IJV images with (a) low brightness, (b) high brightness, (c) fully collapsed, (d) partially missing contour (broken edge), (e) sharp contour (triangular) shape, and (f) non-convex contour shape. 86

5.2 Temporal variations of IJV csa obtained from manual segmentation of two IJV videos with different CSA variability. 87

5.3 An example of polar contour with eight contour points. 91

5.4 Adaptive polar structure. 97

5.5 The validation rates in terms of DF, sensitivity, and specificity versus the parameter α. 113

5.6 The validation rates in terms of DF, sensitivity, and specificity versus the parameter β. 114

5.7 The validation rates in terms of DF, sensitivity, and specificity versus the parameter γ. 115

5.8 The validation rates in terms of DF, sensitivity, and specificity versus the parameter κ. 116

5.9 The validation rates in terms of DF, sensitivity, and specificity versus the parameter ζ. 117

5.10 The validation rates in terms of DF, sensitivity, and specificity versus the parameter ν. 118

5.11 Influence of contour spacing Λ on the accuracy of Ad-PAC segmentation. 119

5.12 Tracking of the IJV in a good quality video for manual segmentation, Ad-PAC and eight other algorithms. 120

5.13 Tracking of the IJV in a poor quality video for manual segmentation, Ad-PAC and eight other algorithms. 123

5.14 The mean level of agreement between algorithm and manual segmentation versus frame index. 124

5.15 The average level of agreement with manual segmentation versus frame index for ultrasound videos with (a) good, (b) average, and (c) poor qualities. 125

5.16 The average level of agreement with manual segmentation versus frame index for (a) oval shape, (b) 1+ apices shape, (c) fully collapsed videos. 125

5.17 The average level of agreement with manual segmentation for IJV videos with (a) less than 10% variation, (b) 10-90% variation, (c) greater than 90% variation. 126

6.1 Sample IJV images from six healthy subjects ((a)-(f)), and six CHF patients ((g)-(l)). 140

6.2 The architecture of the 3D CNN with video input size $32 \times 32 \times 15$ and four convolutional encoders (C32N15L3). 145

6.3 The architecture of the 3D CNN with video input size $32 \times 32 \times 15$ and four convolutional encoders (C64N10L3). 145

6.4 The architecture of the 3D CNN with video input size $90 \times 90 \times 15$ and four convolutional encoders (C90N15L4). 146

6.5 The architecture of the 3D CNN with image sequence input size $90 \times 90 \times 15$ and five convolutional encoders (C90N15L5). 146

6.6 The architecture of the 3D CNN with image sequence input size $90 \times 90 \times 15$ and six convolutional encoders (C90N15L5). 147

6.7 A sample ultrasound label patch where the IJV is entirely inside the patch. 148

6.8 A sample ultrasound label patch where a part of the IJV is inside the patch. 149

6.9 A sample ultrasound label patch where the IJV is entirely outside the patch. 149

6.10 The activation map of the first convolutional layer in the trained C90N15L4.151

6.11 The activation map of the fourth (last) convolutional layer in the trained C90N15L4. 151

6.12 The results of the proposed algorithm for the video captured from a the CHF patient in standing position. 156

6.13 The results of the proposed algorithm for a healthy subject with collapsed IJV. 157

6.14 The results of the proposed algorithm for the video captured from a healthy subject with a round IJV shape. 158

6.15 The results of the proposed algorithm for the video captured from a healthy subject with a the IJV with partially missing edges. 159

6.16 The results of the proposed algorithm for the video captured from a the CHF patient in standing position. In this case, the quality of the image is extremely low as even the point manually located by the expert is not for certain. 160

Chapter 1

Introduction

1.1 Research Motivation

Trauma patients suffering from hemorrhagic shock as a result of blood loss or patients with shortness of breath from volume overload in the setting of congestive heart failure frequently require immediate resuscitation. Fast and accurate assessment of circulating blood volume in critically-ill patients is a challenging task as excessive or insufficient fluid administration increases patient morbidity and mortality [1, 2, 3, 4, 5]. Clinical research has shown that the variations in the anterior-posterior (AP) diameter of inferior vena cava (IVC) and cross-section area, (CSA) of the internal jugular vein (IJV) can be helpful in approximating a patient's volume status and whether or not they will benefit from additional intravenous fluids [6, 7]. Traditionally, the AP-diameter is manually estimated from portable ultrasound imagery - often a challenging and time-consuming task in the setting of poor image quality. Artifacts such as shadowing and speckle noise frequently result in indistinct edges and gaps in the vessel walls reducing accurate estimation [8]. This approach has limitations in that a skilled operator must perform repeated measurements over time and image quality is often limited by patient factors such as body habitus, bowel gas, and depth of the IVC relative to the anterior abdominal wall.

1.2 Research Objective

We propose model-based segmentation algorithms to measuring the IVC AP-diameter and adaptive segmentation algorithms to segmenting the CSA of the IJV. In the IVC scenario, an active circle algorithm incorporates a novel evolution functional to estimate the AP-diameter of the IVC across a spectrum of image qualities.

For the IJV scenario, a novel adaptive polar AC algorithm (Ad-PAC) is proposed for semi-automatic segmentation and tracking of IJV videos. This algorithm involves the initial frame being manually segmented by an operator and subsequently serving as the reference for the initial energy function parameters selection. The parameters are then adapted from one frame to the next based on the segmentation results of previous frames.

1.3 Thesis Structure

In Chapter 2, we propose a novel polar AC algorithm for segmentation of IVC. In the proposed model, we show that the third centralized moment provides useful information and hence, can be used as the energy functional in ACs when they are used for segmentation of ultrasound images, particularly ultrasound images of the IVC.

In Chapters 3 and 4, we propose active shape models for estimation of the IVC AP-diameter in ultrasound images. In Chapter 3 a novel active circle model for estimation and tracking of the IVC AP-diameter, where the AP-diameter is estimated as the diameter of a circle fitted inside the IVC. This work continued and extended to additional active shape models such as rectangle and ellipse in Chapter 4 and is shown that the best performance is obtained with active rectangle model as the clinically measured AP-diameter is a vertical line segment that can be modeled as the vertical side of a rectangle.

Chapter 5 presents a novel adaptive polar AC algorithm (AdPAC) for segmentation and tracking of IJV in ultrasound images, where the parameters of the AC models can be locally and temporally adapted with the parameters of the IJV.

In Chapter 6, we propose a novel algorithm based on convolutional neural networks to automatically detect IJV in ultrasound images. The outcome of this algorithm can be combined with the semi-automatic segmentation algorithm in the previous Chapters to form fully automatic algorithm for either IVC AP-diameter estimation or segmentation and tracking if the IJV in ultrasound videos. In Chapter 7, conclusions are drawn and the remaining work is outlined.

1.4 Contributions

This dissertation presents the following novel contributions.

1. We have proposed a novel energy functional based on the third centralized moments. Speckle noise is pervasive throughout ultrasound imagery as the envelope of the ultrasound wave reflected from each body tissue which is a random variable closely approximated by a Rayleigh distribution. In this dissertation, we show that these distributions can be efficiently separated using the third centralized moment as this moment's local minima is at the boundaries between each two adjacent tissues. We combine this energy functional with a polar AC and propose a novel polar AC capable of efficiently segmenting objects in ultrasound images.

2. We have developed a novel active circle algorithm to estimate the AP-diameter

of the IVC. The proposed algorithm is based on a heuristic evolution functional that performs very well with ultrasound images. In this research, we show that the actual value of the AP-diameter can be efficiently modeled as the diameter of a circle fitted inside the IVC. Since a circle has only three degrees of freedom, the proposed algorithm has very low complexity supporting efficient and accurate estimation of the AP-diameter.

3. We have extended our proposed active circle algorithm to encompass both active ellipse and rectangle functionality. The motivation for developing an active rectangle algorithm is that the clinically measured AP-diameter is different from its actual values as clinicians measure the AP-diameter as the largest vertical diameter of the IVC. The height of a thin rectangle fitted inside the IVC can efficiently model its clinically measured AP-diameter. We also develop another algorithm based on ellipse fitting just for comparison purposes. Experimental results show that the proposed active rectangle algorithm performs very close to expert manual measurements.

4. In this dissertation, we also develop an adaptive polar AC (Ad-PAC) algorithm, where the parameters of the AC are spatially and temporally adapted based on the results obtained from the previous frame. The motivation behind this work is that the performance of ACs depend on several factors including image quality, the shape of the object, and its spatial and temporal characteristics. The proposed algorithm provides an adaptive solution capable of automatically optimizing any AC-based segmentation problem by providing local spatial and temporal parameter adaptation. The proposed Ad-PAC algorithm provides three contributions for researchers in the field of image segmentation as: i. Spatial parameterization of ACs. iii. Spatial and temporal parameters adaptation.

   iii. The novel energy terms that are modified from those traditionally used in polar ACs.

5. Finally, we develop a novel algorithm based on 3D-CNNs to automatically localize the IJV in ultrasound images. Although the proposed algorithm has been developed for IJV localization, it can be used for other object localization applications by additional training of the 3D-CNN.

References

[1] H. Kasuya, H. Onda, T. Yoneyama, T. Sasaki, and T. Hori. Bedside monitoring of circulating blood volume after subarachnoid hemorrhage. *Stroke*, 34(4):956–960, 2003. doi: 10.1161/01.str.0000064321.10700.63.

[2] Frank Bremer, Albert Schiele, Jan Sagkob, Thomas Palmaers, and Klaus Tschaikowsky. Perioperative monitoring of circulating and central blood volume in cardiac surgery by pulse dye densitometry. *Intensive Care Med Intensive Care Medicine*, 30(11):2053–2059, 2004. doi: 10.1007/s00134-004-2445-8.

[3] Vassilios Smyrniotis, Georgia Kostopanagiotou, Kassiani Theodoraki, Dimitrios Tsantoulas, and John C Contis. The role of central venous pressure and type of vascular control in blood loss during major liver resections. *The American journal of surgery*, 187(3):398–402, 2004.

[4] J. Kevin Bailey, John Mccall, Suzanne Smith, and Richard J. Kagan. Correlation of internal jugular vein/common carotid artery ratio to central venous pressure. *Journal of Burn Care & Research*, 33(1):89–92, 2012. doi: 10.1097/bcr.0b013e318234d965.

[5] Kasana Raksamani, Vachira Udompornmongkol, Suwannee Suraseranivongse, Manee Raksakietisak, and Benno Von Bormann. Correlation between cross-sectional area of the internal jugular vein and central venous pressure. *European Journal of Anaesthesiology*, 31(1):50–51, 2014. doi: 10.1097/eja.0b013e32835f9a50.

[6] Cyril Charron, Vincent Caille, Francois Jardin, and Antoine Vieillard-Baron. Echocardiographic measurement of fluid responsiveness. *Current opinion in critical care*, 12(3):249–254, 2006.

[7] Lakshmi Durairaj and Gregory A Schmidt. Fluid therapy in resuscitated sepsis: less is more. *Chest Journal*, 133(1):252–263, 2008.

[8] Weiming Wang, Lei Zhu, Jing Qin, Yim-Pan Chui, Bing Nan Li, and Pheng-Ann Heng. Multiscale geodesic active contours for ultrasound image segmentation using speckle reducing anisotropic diffusion. *Optics and Lasers in Engineering*, 54:105–116, 2014.

Chapter 2

Segmentation and Tracking of IVC in Ultrasound Images Using a Novel Polar Active Contour

In this Chapter, a novel polar active contour algorithm based on the third image moment is proposed and used for segmentation and tracking of the IVC in ultrasound images. To validate the proposed research in this Chapter, we compare the proposed algorithm to manual segmentation and three relevant state-of-the-art algorithms. It is shown that the algorithm outperforms other techniques and in some scenarios appears to have advantages over manual segmentation creating the potential to improve medical management in critically-ill patients.

2.1 Introduction

Accurate volume resuscitation of the critically-ill using fluids and blood products is a challenging endeavor as insufficient, excessive or delayed administration increases patient morbidity and mortality [1, 2]. Research has shown that respiratory variation in the inferior vena cana (IVC) resulting in changes in the anterior-posterior (AP) diameter is useful to predict fluid responsiveness [3, 4]. Current practice involves manual measurement of the IVC diameter and its temporal variation from ultrasound imagery however, this can be a challenging task as the image quality suffers from artifact and severe speckle noise making the vessel indistinct with unclear boundaries [5, 6]. Semi-automatic segmentation algorithms have the potential to address this issue.

Speckle noise present in ultrasound imagery is traditionally considered as Rayleigh distributed multiplicative noise [7], and hence, Rayleigh mixture models have been proposed as a potential solution for ultrasound image segmentation [8, 9]. But it has been shown that the scattering population and signal processing introduce speckle noise with non-Rayleigh distribution [10]. Furthermore, lossy compression algorithms present on many porTable ultrasound machines further deviate the recorded clip from the idealized Rayleigh distribution. In [11], it was shown that optical flow algorithms can be efficiently used for speckle tracking but this approach ignores information in vessel shape.

Active contours (AC), as planar deformable models, are widely used for segmentation of ultrasound images [12, 13, 14]. ACs perform image segmentation via minimization of an energy functional with their performance frequently dependent on a manually-defined initialization contour. In order to avoid local minima, the initiating contour needs to be as close to the actual contour as possible. ACs can be combined with other segmentation algorithms as a coarse-to-fine strategy to reduce the impact of the initial contour on segmentation error [15, 16, 17]. Researchers [18] have approached segmenting the IVC in which the coarse segmentation obtained from template matching was smoothed with an AC (TMAC). Unfortunately, this approach fails when the

IVC undergoes large frame-to-frame variations commonly present on porTable machines with lower frame rates. Despite these improvements, ACs continue to perform poorly in setting of fuzzy or unclear boundaries as is commonly the case for the IVC. Since the IVC contour is convex, polar ACs appear as a promising solution for IVC segmentation [19, 20]. In this Chapter, we propose a novel polar AC algorithm incorporating a novel energy functional for segmentation and tracking of the IVC in the setting of poor image quality. The proposed energy functional appears promising for other ultrasound image segmentation problems as well.

The remainder of this Chapter is organized as follows - Section II introduces the background and related work. The proposed polar AC algorithm is presented in Section III. The experimental results are presented in Section IV and the Chapter is concluded in Section V.

2.2 Background and Related work

2.2.1 IVC Image Structure

Fig. 2.1 displays a typical ultrasound image of the IVC demonstrating that the boundary is fuzzy as the cross-section of IVC is not seen as a circle. Moreover, the intravascular region is largely hypo-echoic and extravascular hyper-echoic resulting in regional distributions with different means. Fig. 2.2 illustrates the probability density functions (PDFs) of the intensity levels inside the disks concentric with the IVC with diameters as (a): $D = 0.8D_{IVC}$, (b): $D = D_{IVC}$, (c): $D = 1.2D_{IVC}$, where D_{IVC} is the actual diameter of the IVC. From Fig. 2.2-(a) and (b), one can see that the intensity distribution inside the IVC contour is sparse. Assuming that the intensity levels inside and outside the IVC have PDFs $F_{in}(.)$ with mean m_{in} and $F_{out}(.)$ with m_{out}, respectively. It is clear that $m_{in} < m_{out}$ suggesting that regardless of the PDFs

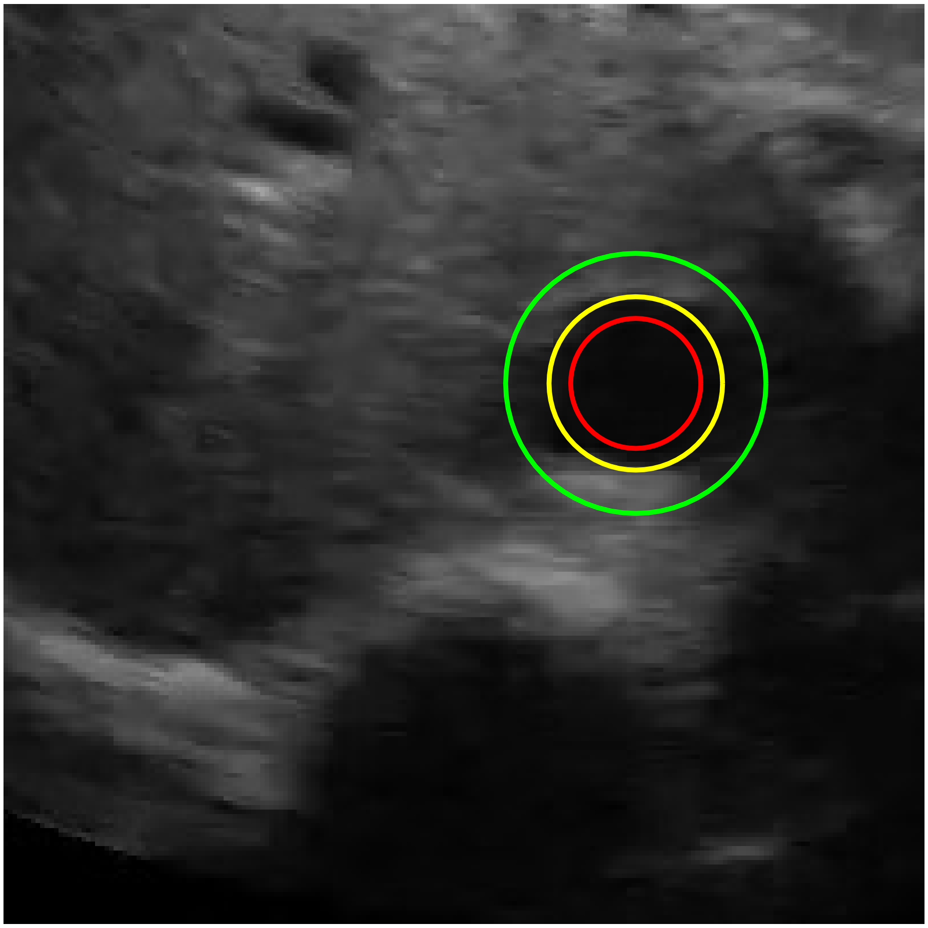

Figure 2.1: A typical ultrasound image of IVC.

$F_{in}(.)$ and $F_{out}(.)$, their distinct means can be used for image segmentation.

2.2.2 Energy and Evolution Functionals

In traditional level set methods for a given energy functional $C(.)$, the evolution functional is obtained as [21, 22]:

$$E\frac{\partial C}{\partial t} = -F(|\nabla C|), \tag{2.1}$$

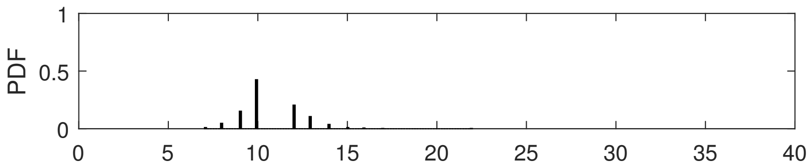

(a) Region 1

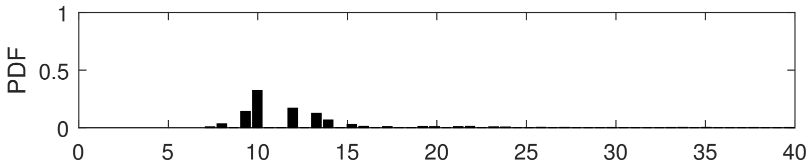

(b) Region 2

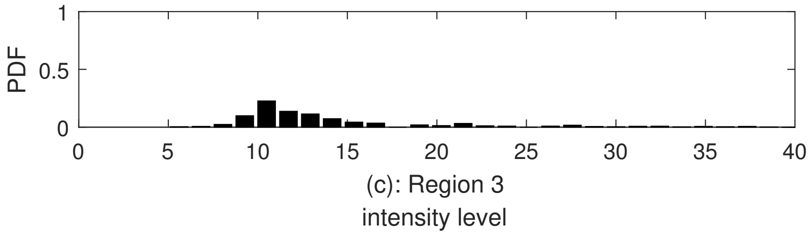

(c): Region 3

Figure 2.2: PDF of the intensity levels inside the disks concentric with the IVC with radius equal to (a): 80%, (b): 100%, and (c): 120% of the IVC.

where the function $F(.)$ depends on the image and is usually defined as a linear function. In this Chapter, we use the following linear function [21, 22]

$$E = -|\nabla C|\vec{n}, \tag{2.2}$$

where $\vec{n}$ is the vector normal to the contour.

Two conventional functionals, widely employed in variational ACs, are based on the mean and the variance [23, 24].

Functional Based on Means: Assuming u and v represent the mean intensity levels inside and outside the IVC, respectively, the energy functional is defined as [24]

$$C_{mean} = -\frac{\alpha}{2}(u - v)^2, \tag{2.3}$$

where α is a positive weighting factor. Using (2.1), the evolution functional corresponding to (2.3) is obtained as [24]

$$E_{mean} = -\alpha(u - v)\left(\frac{I - u}{A_u} + \frac{I - v}{A_v}\right)\vec{n}, \tag{2.4}$$

where I is the intensity at the contour point and A_u and A_v are the areas inside and outside the contour, respectively.

Functional Based on Variances: Assuming σ_u^2 and σ_v^2 as the variances of intensity levels inside and outside the IVC respectively, the energy functional is defined as [24]

$$C_{var} = \sigma_u^2 + \sigma_u^2, \tag{2.5}$$

This functional is commonly used for thresholding. Using (2.1), the evolution functional corresponding to (2.5) is obtained as

$$E_{var} = \alpha\left(\frac{I^2 - u^2 - \sigma_u^2}{A_u} - \frac{I^2 - v^2 - \sigma_v^2}{A_v}\right)\vec{n}, \tag{2.6}$$

where u and σ_u^2 are the mean and variance of the intensities inside the contour while v and σ_v^2 represent outside the contour.

2.3 Proposed Algorithm

2.3.1 Proposed Energy Functional

The proposed functional includes the energy in the third centralized moment of the object and the curvature energy as follows

$$E = E_{M3} + E_{curv}, \tag{2.7}$$

where E_{M3} and E_{curv} are defined as

$$E_{M3} = -\alpha M_3, \tag{2.8}$$

where M_n is the nth centralized moment of the object and is obtained as

$$M_n = \frac{\int_C (I-u)^n dA}{\int_C dA}, \tag{2.9}$$

$$E_{curv} = \beta \sum_{n=0}^{N-1} |p_{n+1} - 2p_n + p_{n-1}|^2, \tag{2.10}$$

where α and β are positive weights given to each energy term, u is the mean intensity inside the object and p_n is the point vector defined as

$$\left[x_c + \rho_n \cos(n\phi_0), y_c + \rho_n \sin(n\phi_0)\right], \tag{2.11}$$

with x_c and y_c being the coordinates of a point (center) inside the IVC, $\phi_0 = \frac{2\pi}{N}$, $|\nabla I|$, and ρ_n as the corresponding radial coordinate. In the rest of this section, we discuss each of these two energy terms in detail and derive their corresponding evolution functionals in the polar coordinates system.

E_{M3} *energy*: Fig. 2.3 shows the E_{M3} for the image shown in Fig. 2.1 with the x-axis being the normalized circle radius, R_{IVC}, and y-axis the E_{M3} inside the contour with α normalized to one. This figure shows that the E_{M3} finds its minimum at the IVC boundaries and hence is a suiTable choice for the segmentation of IVC in ultrasound imagery. The gradient of E_{M3} versus $\boldsymbol{\rho} = [\rho_0, \rho_1, ..., \rho_{N-1}]^T$ is obtained as

$$\frac{\partial E_{M3}}{\partial \boldsymbol{\rho}} = \boldsymbol{A_c \rho}, \tag{2.12}$$

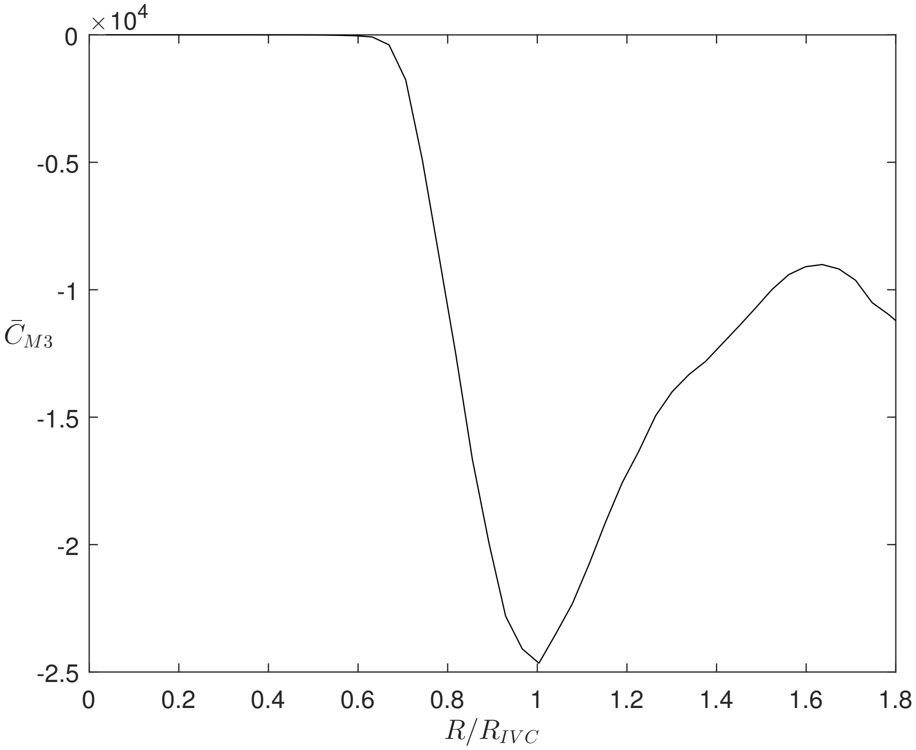

Figure 2.3: E_{M3} inside a circular contour C versus the normalized radius with $\alpha = 1$.

where $\mathbf{A}_c$ is a tri-diagonal matrix defined as follows,

$$a_c(i,j) = \begin{cases} \kappa_n, & \text{if} \quad mod(|i-j|, N) = 1, \\ 0, & \text{otherwise}, \end{cases} \tag{2.13}$$

with κ_n defined as

$$\kappa_n = \alpha_0[(I(p_n) - u)^3 - M_3 - 3(I(p_n) - u)M2], \tag{2.14}$$

where $\alpha_0 = -0.5\alpha \sin(\phi_0)$ and $I(p_n)$ is the pixel intensity at contour point p_n.

The curvature energy: By substitution of (2.11) in (2.10), the curvature energy function is rewritten as

$$E_{curv} = \sum_{n=0}^{N-1} \alpha_n [4\rho_n^2 + \rho_{n_{-1}}^2 + \rho_{n_{+1}}^2 - 4\rho_n(\rho_{n_{-1}} + \rho_{n_{+1}}) \tag{2.15}$$

$$\times \cos(\phi_0) + 2\rho_{n_{-1}}\rho_{n_{+1}} \cos(2\phi_0)], \tag{2.16}$$

and its gradient with respect to $\boldsymbol{\rho}$ is obtained as

$$\frac{\partial E_{curv}}{\partial \boldsymbol{\rho}} = \boldsymbol{B_c \rho}, \tag{2.17}$$

where $\mathbf{B}_c$ is a penta-diagonal matrix defined as follows,

$$b_c(i,j) = \begin{cases} 2\beta\cos(2\phi_0), & \text{if} \quad mod(i-j,N) = 2, \\ -8\beta\cos(\phi_0), & \text{if} \quad mod(i-j,N) = 1, \\ 12\beta, & \text{if} \quad i = j, \\ -8\beta\cos(\phi_0), & \text{if} \quad mod(j-i,N) = 1, \\ 2\beta\cos(2\phi_0), & \text{if} \quad mod(j-i,N) = 2, \\ 0, & \text{otherwise.} \end{cases} \tag{2.18}$$

Using (2.12) and (2.17), the energy functional in (2.7) can be iteratively minimized as

$$\boldsymbol{\rho}_{(i)} = \boldsymbol{\rho}_{(i-1)} - \mu(\mathbf{A}_c + \mathbf{B}_c)\boldsymbol{\rho}_{(i-1)}, \tag{2.19}$$

where μ is step-size parameter.

2.3.2 Proposed Algorithm

The proposed polar algorithm is summarized as

Table 1. Proposed Polar AC Algorithm

Input: The center of IVC in the initial frame and parameters α and β and μ and initial vector $\boldsymbol{\rho}_{(0)}$. In this research, we set them as $\alpha = 25$, $\beta = 0.025$, $\mu = 0.01$, and $\boldsymbol{\rho}_{(0)} = 12 \times \mathbf{1}_{N\times 1}$, where $\mathbf{1}_{N\times 1}$ is $N \times 1$ all-ones vector.

Step 1 - Read the first frame from the video.

Step 2 - Manually select the center of the first frame.

Step 3 - Update $\boldsymbol{\rho}$ using (2.19).

Step 4 - Repeat Step 3 until the algorithm reaches to the equilibrium condition. The equilibrium condition is defined as the condition where the maximum absolute value of change in $\boldsymbol{\rho}$ at the previous step is less than 10^{-3} pixels.

Step 5 - Return to step 3 for the next frame.

2.4 Results

The experimental data was collected from two healthy subjects after ethics approval was granted. The IVC was imaged in the transverse plane using a porTable ultrasound (M-Turbe, Sonosite-FujiFilm) with a phased-array probe (1-5 Mhz). Each video has a frame rate of 30 fps, scan depth of 19cm, and a duration of 15 seconds (450 frames/clip). The proposed algorithm was also compared with expert manual segmentation, two classic AC algorithms - Chan-Vese [25] and Geodesic [26], and two state-of-the-art polar ACs- PSnake [27] and variational polar AC [20]. All algorithms were implemented by MATLAB and the parameters of other four algorithms were optimized by exhaustive search over the test data. Fig. 2.4 depicts the tracking performance of the investigated algorithms and compares them with manual segmentation. As one can see from Fig. 2.4, except the proposed algorithm, the other four algorithms are not able to track the IVC contour.

Fig. 2.5 presents the IVC area estimated using the proposed algorithm, manual segmentation and four other algorithms for the video depicted in Fig. 2.1. This confirms that only the proposed algorithm accurately tracks and segments the IVC and follows the variations in manual segmentation and the other four algorithms quickly lose tracking.

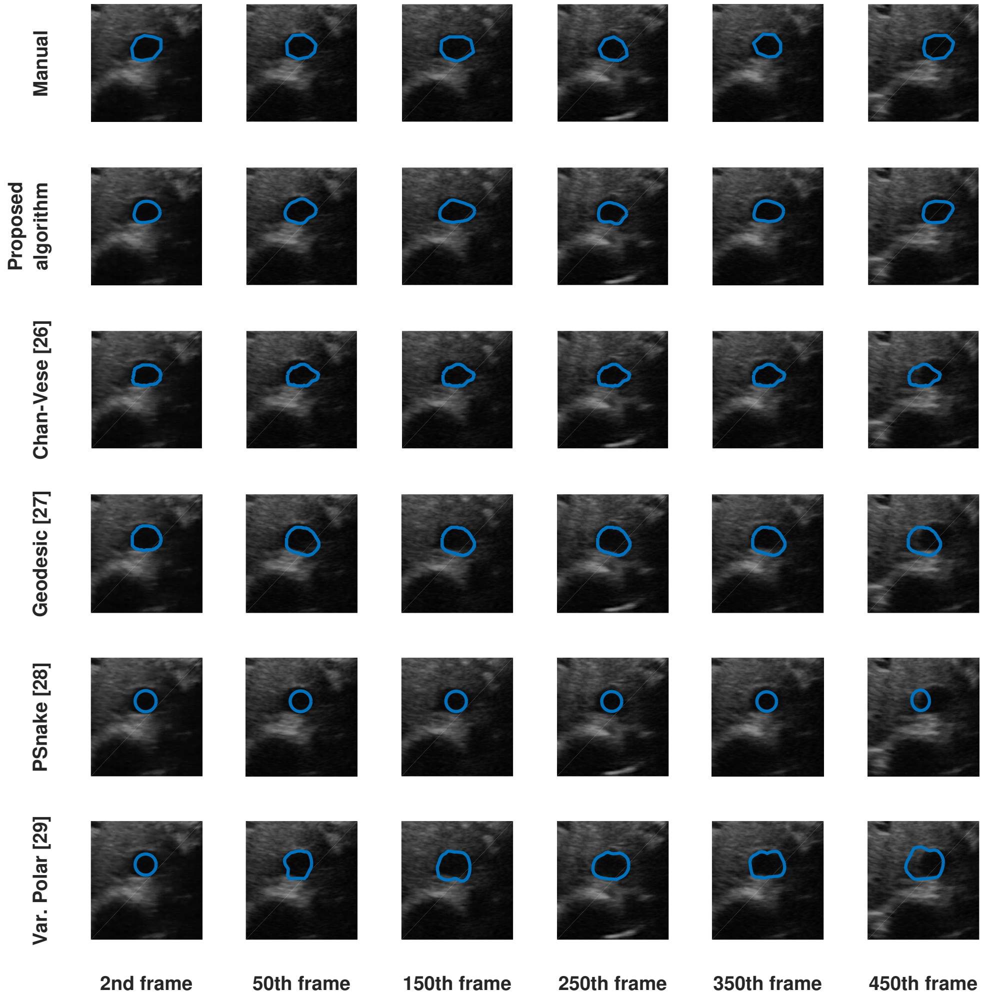

Figure 2.4: Tracking of the IVC for manual segmentation, proposed algorithm and four other algorithms.

Fig. 2.6 details the results for a lower quality IVC video. Here, it is evident that the proposed algorithm again tracks the temporal variations of the manual segmentation while the other four algorithm are unable to track the IVC.

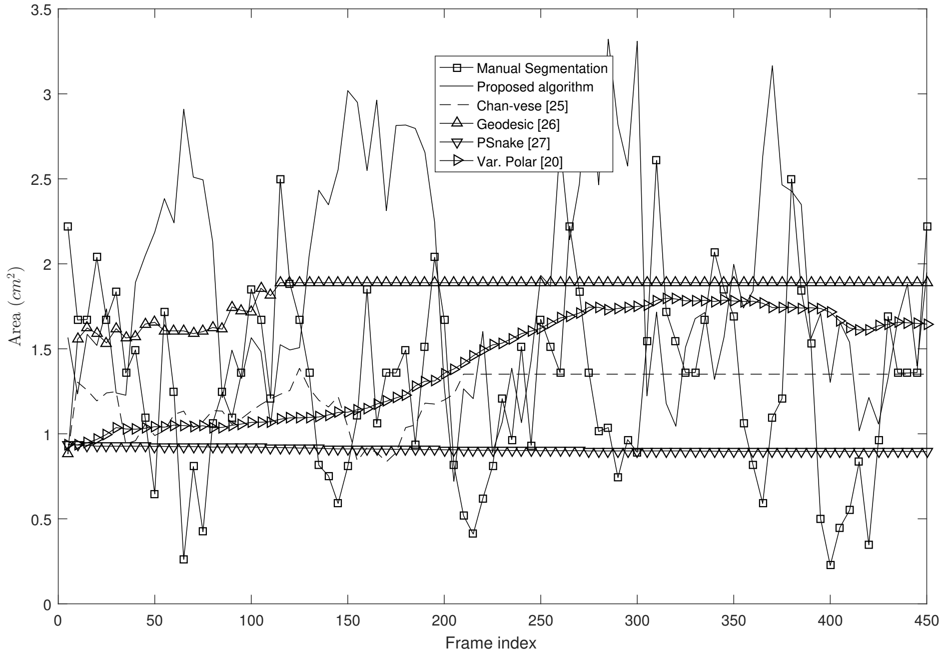

Figure 2.5: IVC area (Fig 1.) as measured by the proposed algorithm, manual segmentation, and four other algorithms.

2.5 Conclusion

In this Chapter, a novel polar active contour algorithm is developed for segmentation and tracking of the IVC in ultrasound imagery. A novel energy functional based on the third centralized moment of the object (in this research the area inside IVC) was proposed and used for updating polar active contour algorithm. Experimental results suggest that the proposed algorithm outperforms existing segmentation algorithms and suggests improvement over manual segmentation. As the future work, the algorithm should be applied to a larger dataset to explore its clinical applicability.

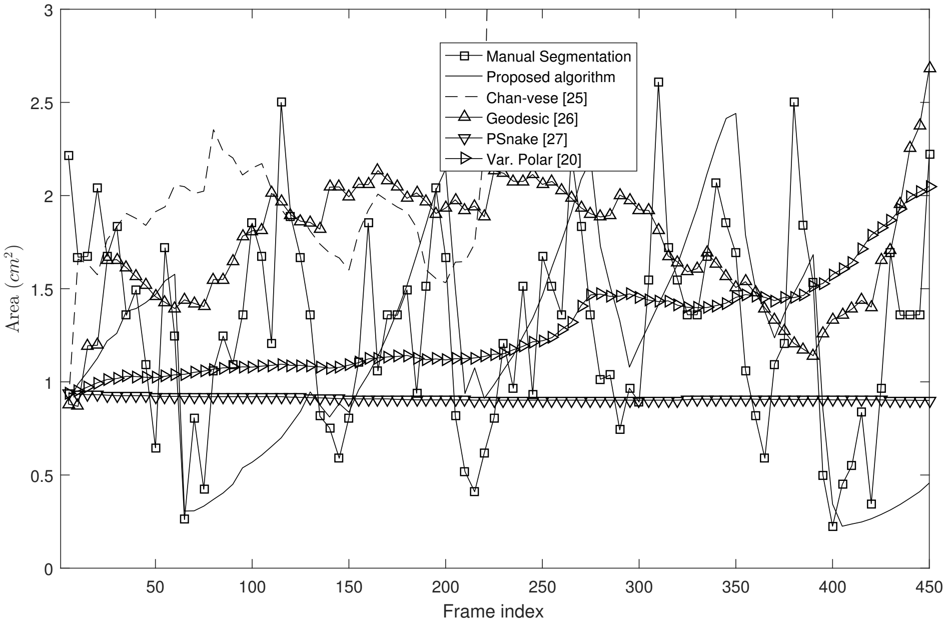

Figure 2.6: IVC area as estimated by the proposed algorithm, manual segmentation, and four other algorithms.

References

[1] Vassilios Smyrniotis, Georgia Kostopanagiotou, Kassiani Theodoraki, Dimitrios Tsantoulas, and John C Contis. The role of central venous pressure and type of vascular control in blood loss during major liver resections. *The American journal of surgery*, 187(3):398–402, 2004.

[2] Emanuel Rivers, Bryant Nguyen, Suzanne Havstad, Julie Ressler, Alexandria Muzzin, Bernhard Knoblich, Edward Peterson, and Michael Tomlanovich. Early goal-directed therapy in the treatment of severe sepsis and septic shock. *New England Journal of Medicine*, 345(19):1368–1377, 2001.

[3] Cyril Charron, Vincent Caille, Francois Jardin, and Antoine Vieillard-Baron. Echocardiographic measurement of fluid responsiveness. *Current opinion in critical care*, 12(3):249–254, 2006.

[4] Lakshmi Durairaj and Gregory A Schmidt. Fluid therapy in resuscitated sepsis: less is more. *Chest Journal*, 133(1):252–263, 2008.

[5] Weiming Wang, Lei Zhu, Jing Qin, Yim-Pan Chui, Bing Nan Li, and Pheng-Ann Heng. Multiscale geodesic active contours for ultrasound image segmentation using speckle reducing anisotropic diffusion. *Optics and Lasers in Engineering*, 54:105–116, 2014.

[6] Suresh Sudha, GR Suresh, and R Sukanesh. Speckle noise reduction in ultrasound images by wavelet thresholding based on weighted variance. *International journal of computer theory and engineering*, 1(1):7, 2009.

[7] Robert F Wagner, Stephen W Smith, John M Sandrik, and Hector Lopez. Statistics of speckle in ultrasound b-scans. *IEEE transactions on sonics and ultrasonics*, 30(3):156–163, 1983.

[8] José C Seabra, Francesco Ciompi, Oriol Pujol, Josepa Mauri, Petia Radeva, and Joao Sanches. Rayleigh mixture model for plaque characterization in intravascular ultrasound. *IEEE Transactions on Biomedical Engineering*, 58(5):1314–1324, 2011.

[9] Marcelo Pereyra, Nicolas Dobigeon, Hadj Batatia, and Jean-Yves Tourneret. Segmentation of skin lesions in 2-d and 3-d ultrasound images using a spatially coherent generalized rayleigh mixture model. *IEEE transactions on medical imaging*, 31(8):1509–1520, 2012.

[10] TA Tuthill, RH Sperry, and KJ Parker. Deviations from rayleigh statistics in ultrasonic speckle. *Ultrasonic imaging*, 10(2):81–89, 1988.

[11] Ebrahim Karami, Mohamed S Shehata, and Andrew Smith. Tracking of the internal jugular vein in ultrasound images using optical flow. In *The 30th Annual IEEE Canadian Conference on Electrical and Computer Engineering (CCECE), Windsor, Canada*, pages 1–4. IEEE, 2017.

[12] Michael Kass, Andrew Witkin, and Demetri Terzopoulos. Snakes: Active contour models. *International journal of computer vision*, 1(4):321–331, 1988.

[13] Mohammad Talebi, Ahamd Ayatollahi, and Ali Kermani. Medical ultrasound image segmentation using genetic active contour. *Journal of Biomedical Science and Engineering*, 4(02):105, 2011.

[14] J Alison Noble. Ultrasound image segmentation and tissue characterization. *Proceedings of the Institution of Mechanical Engineers, Part H: Journal of Engineering in Medicine*, 224(2):307–316, 2010.

[15] Sahirzeeshan Ali and Anant Madabhushi. An integrated region-, boundary-,

shape-based active contour for multiple object overlap resolution in histological imagery. *IEEE transactions on medical imaging*, 31(7):1448–1460, 2012.

[16] E Karami, M Shehata, P McGuire, and A Smith. A semi-automated technique for internal jugular vein segmentation in ultrasound images using active contours. In *2016 IEEE-EMBS International Conference on Biomedical and Health Informatics (BHI)*, pages 184–187. IEEE, 2016.

[17] Ebrahim Karami, Mohamed Shehata, and Andrew Smith. Ultrasound image segmentation techniques for tracking and measurement of the internal jugular vein. In *The 24th Annual Newfoundland Electrical and Computer Engineering Conference (NECEC), St. John's, Canada*, 2015.

[18] Kensuke Nakamura, Makoto Tomida, Takehiro Ando, Kon Sen, Ryota Inokuchi, Etsuko Kobayashi, Susumu Nakajima, Ichiro Sakuma, and Naoki Yahagi. Cardiac variation of inferior vena cava: new concept in the evaluation of intravascular blood volume. *Journal of Medical Ultrasonics*, 40(3):205–209, 2013.

[19] Tao Li, Alexandre Krupa, and Christophe Collewet. A robust parametric active contour based on fourier descriptors. In *2011 18th IEEE International Conference on Image Processing*, pages 1037–1040. IEEE, 2011.

[20] Maximilian Baust, Anthony J Yezzi, Gozde Unal, and Nassir Navab. A sobolev-type metric for polar active contours. In *Computer Vision and Pattern Recognition (CVPR), 2011 IEEE Conference on*, pages 1017–1024. IEEE, 2011.

[21] Chunming Li, Chenyang Xu, Changfeng Gui, and Martin D Fox. Level set evolution without re-initialization: a new variational formulation. In *Computer Vision and Pattern Recognition, 2005. CVPR 2005. IEEE Computer Society Conference on*, volume 1, pages 430–436. IEEE, 2005.

[22] Daniel Cremers, Stanley J Osher, and Stefano Soatto. Kernel density estimation and intrinsic alignment for shape priors in level set segmentation. *International journal of computer vision*, 69(3):335–351, 2006.

[23] Anthony Yezzi, Andy Tsai, and Alan Willsky. A statistical approach to curve evolution for image segmentation. In *IEEE International Conference on Computer Vision, Corfu, Greece*, 1999.

[24] Anthony Yezzi, Lilla Zöllei, and Tina Kapur. A variational framework for integrating segmentation and registration through active contours. *Medical image analysis*, 7(2):171–185, 2003.

[25] Tony F Chan and Luminita A Vese. Active contours without edges. *IEEE Transactions on image processing*, 10(2):266–277, 2001.

[26] Vicent Caselles, Ron Kimmel, and Guillermo Sapiro. Geodesic active contours. *International journal of computer vision*, 22(1):61–79, 1997.

[27] Auzuir Ripardo De Alexandria, Paulo Cesar Cortez, Jessyca Almeida Bessa, John Hebert da Silva Felix, Jose Sebastiao De Abreu, and Victor Hugo C De Albuquerque. psnakes: A new radial active contour model and its application in the segmentation of the left ventricle from echocardiographic images. *Computer methods and programs in biomedicine*, 116(3):260–273, 2014.

Chapter 3

Estimation and Tracking of the IVC AP-diameter Using a Novel Active Circle Algorithm

Medical research suggests that the anterior-posterior (AP)-diameter of the inferior vena cava (IVC) and its associated temporal variation as imaged by bedside ultrasound is useful in guiding fluid resuscitation in the critically-ill patient. Unfortunately, indistinct edges and gaps in vessel walls are frequently present which impede accurate estimation of the IVC AP-diameter for both human operators and segmentation algorithms.

The majority of clinical research involving use of the IVC to guide fluid resuscitation involves manual measurement of the maximum and minimum AP-diameter as it varies over time. We have developed and evaluated a time-varying circle fitted inside the typically ellipsoid IVC as an efficient, consistent and novel approach to tracking and approximating the AP-diameter even in the context of poor image quality. In this active-circle algorithm, a novel evolution functional is proposed and shown to be a useful tool for ultrasound image processing. The proposed algorithm is compared with an expert manual measurement, and relevant state-of-the-art algorithms. It is shown that the algorithm outperforms other techniques and performs very close to manual measurement.

3.1 Introduction

Trauma patients suffering from hemorrhagic shock as a result of blood loss or patients with shortness of breath from volume overload in the setting of congestive heart failure frequently require immediate resuscitation. Fast and accurate assessment of circulating blood volume in critically-ill patients is a challenging task as excessive or insufficient fluid administration increases patient morbidity and mortality[1, 2]. Clinical research has shown that the variations in the anterior-posterior (AP) diameter of inferior vena cava (IVC) can be helpful in approximating a patient's volume status and whether or not they will benefit from additional intravenous fluids [3, 4, 5]. Traditionally, the AP-diameter is manually estimated from porTable ultrasound imagery - often a challenging and time-consuming task in the setting of poor image quality. Artifacts such as shadowing and speckle noise frequently result in indistinct edges and gaps in the vessel walls reducing accurate estimation[6, 7].

Speckle noise present in ultrasound imagery is traditionally considered to be a Rayleigh distributed multiplicative noise [8]. Hence, Rayleigh mixture models have been proposed as a potential solution for ultrasound image segmentation [9, 10]. However, it has been shown that due to the scattering population and signal processing, the speckle distribution deviates from Rayleigh[11]. Furthermore, lossy compression algorithms present on many porTable ultrasound machines further deviate the recorded clip from an idealized Rayleigh distribution.

Active contours (ACs), as planar deformable models, are widely used for segmentation of ultrasound images [12, 13, 14, 15, 16]. ACs address image segmentation through minimization of energy functional(s) with their performance frequently dependent on a manually-defined initialization contour. In order to avoid local minima, the initiating contour needs to be as close as possible to the actual contour. ACs can be combined with other segmentation algorithms as a coarse-to-fine strategy to reduce the impact of the initial contour on segmentation error [17, 18]. Researchers have addressed the challenge of IVC segmentation using this strategy by using template matching method as the coarse segmentation and AC as the fine-tuning (TMAC) [19]. Unfortunately, this approach fails when the IVC undergoes large frame-to-frame variations commonly present on porTable machines with lower frame rates (e.g. 30 frames-per-second). Additionally, ACs continue to perform poorly in the context of fuzzy or unclear boundaries as is commonly the case for the IVC.

Given that the cross-section of the IVC is largely convex, the IVC contour can be represented in polar coordinates and consequently, polar active contours appear as a promising solution for IVC segmentation [20]. In [21], a polar AC model based on the third centralized moment (M3) was proposed for segmentation of IVC images. Unfortunately, M3 algorithm roughly estimates the cross-sectional area (CSA) of the IVC and fails with poor quality images.

Clinically the CSA of the IVC is an optimal approach to accurately assess a patient's volume status, but all existing approaches fail to accurately estimate the CSA. Hence, clinicians instead of the whole CSA of the IVC, measure its AP-diameter. In this Chapter, we propose using an active circle algorithm incorporating a novel evolution functional to estimate the AP-diameter of the IVC across a spectrum of image qualities. In addition, the proposed evolution functional appears promising for other ultrasound image segmentation problems as well.

The remainder of this Chapter is organized as follows - Section II discusses the background and related work. The proposed active circle algorithm is presented in Section III while experimental results are in Section IV and concluding remarks in Section V.

3.2 Background and Related work

3.2.1 IVC Image

Fig. 3.1 displays a typical ultrasound image of the IVC, with a circle fitted on the IVC AP-diameter shown in yellow color. For demonstrating the circle model which is later used in this work, we have also displayed two scaled circles, concentric with the yellow circle with scaling factors $S = 0.75$ and $S = 1.5$ shown in red and green colors, respectively. As in Fig. 3.1, one can see that the IVC boundaries are generally fuzzy and are unclear. On the other hand, one can see that the inside of IVC is generally hypoechoic and the outside is hyperechoic indicating that the inside and outside of the IVC have distributions with different means. Fig. 3.2 illustrates the probability density functions (PDFs) of the intensity levels inside the three circles shown in Fig. 3.1, where the x-axis is the normalized pixel intensity which is between 0 and 1. From Fig. 3.2-(a) and (b), one can see that the intensity distribution inside the IVC contour is more sparse than continuous. Assume that the intensity levels inside and outside the IVC have PDFs F_{in} with mean m_{in} and F_{out} with m_{out}, respectively. It is obvious that $m_{in} < m_{out}$. This indicates that regardless of the PDFs F_{in} and F_{out}, their distinct means can be used for image segmentation.

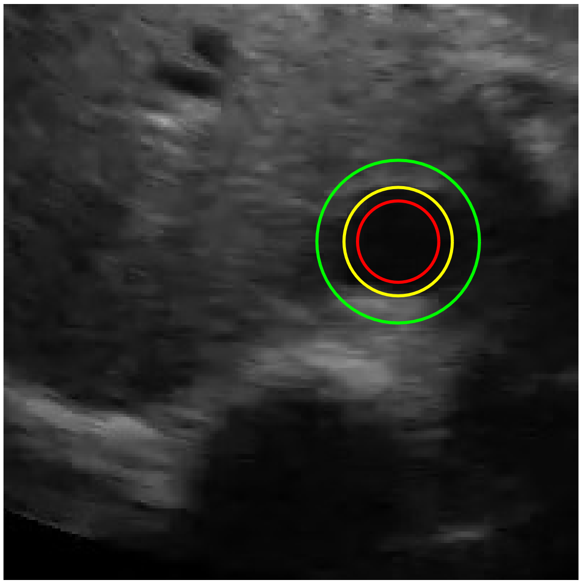

Figure 3.1: A typical ultrasound image of IVC with circle evolution model.

3.2.2 Energy and Evolution Functionals

In traditional level set methods for a given energy functional C, the evolution functional is obtained at [22, 23]:

$$\frac{\partial C}{\partial t} = -F(|\nabla C|), \tag{3.1}$$

where the function F depends on the image and is usually defined as a linear function. In this Chapter, we use the following linear function [22, 23]

$$E = -|\nabla C|\vec{n}, \tag{3.2}$$

where $\vec{n}$ is the vector normal to the contour.

Two conventional functionals, widely employed in variational ACs, are based on the mean and the variance of the intensities [24].

Functional Based on Mean: Assuming u and v represent the mean intensity levels

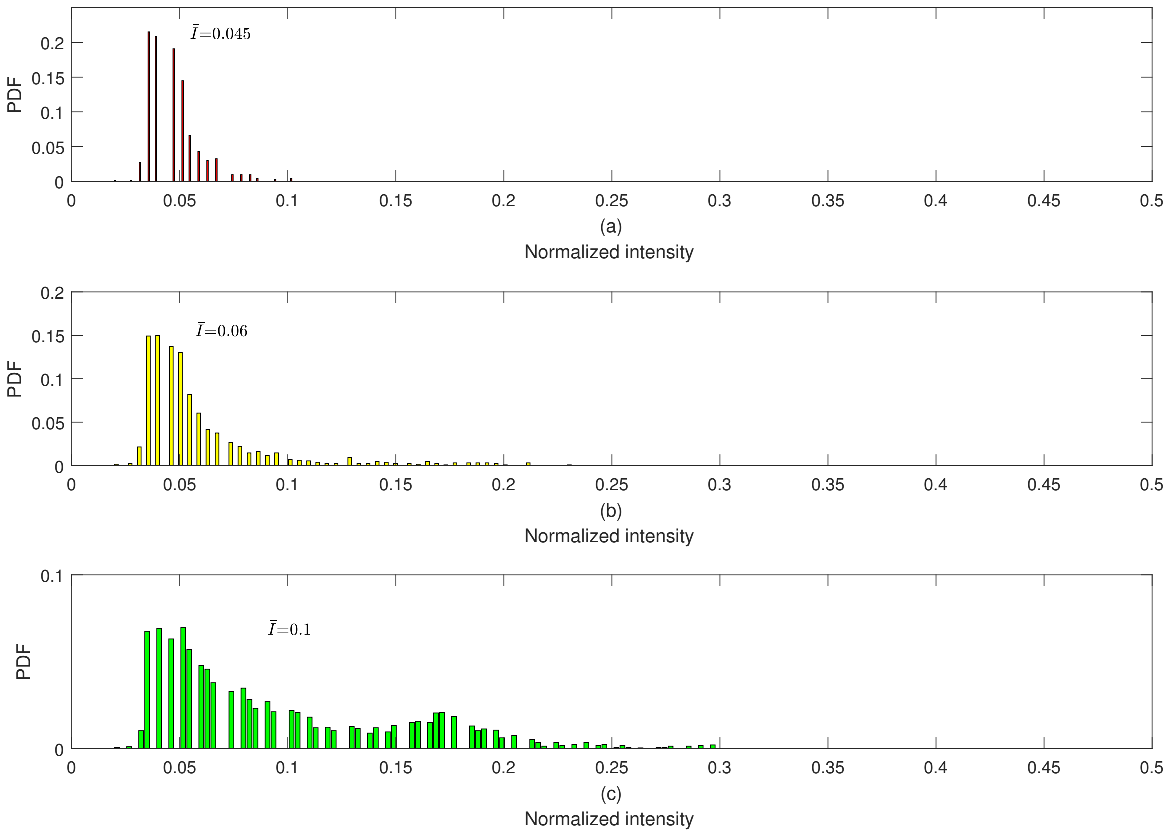

Figure 3.2: PDF of the intensity levels inside the disks concentric with the IVC (see Fig. 3.1) with radius equal to (a): 75%, (b): 100%, and (c): 150% of the IVC AP-diameter.

inside and outside the IVC, respectively, the energy functional is defined as [24]

$$C_{mean} = -\frac{\alpha}{2}(u-v)^2, \tag{3.3}$$

where α is a positive weighting factor. Using (3.1), the evolution functional corresponding to (3.3) is obtained as [24]

$$E_{mean} = -\alpha(u-v)\left(\frac{I-u}{A_u} + \frac{I-v}{A_v}\right)\vec{n}, \tag{3.4}$$

where I is the intensity at the contour point and A_u and A_v are the areas inside and outside the contour, respectively.

Functional Based on Variance: Assuming σ_u^2 and σ_v^2 as the variances of intensity levels inside and outside the IVC respectively, the energy functional is defined as [24]

$$C_{var} = \sigma_u^2 + \sigma_v^2, \tag{3.5}$$

Using (3.1), the evolution functional corresponding to (3.5) is obtained as

$$E_{var} = \alpha \left(\frac{I^2 - u^2 - \sigma_u^2}{A_u} - \frac{I^2 - v^2 - \sigma_v^2}{A_v} \right) \vec{n}, \tag{3.6}$$

where u and σ_u^2 are the mean and variance of the intensities for the pixels inside the contour while v and σ_v^2 represent for the ones outside the contour.

3.3 Proposed Algorithm

3.3.1 Why a Circular Model?

IVC images can be segmented with polar ACs as in [21]. When a polar AC with N contour points is used, the number of parameters that has to be estimated is N, i.e., one radial distance for each contour point, while with traditional Cartesian ACs, $2N$ parameters have to be estimated, i.e., two for x and y coordinates of each contour points. This makes polar contour models less complex and more accurate for vessel segmentation. On the other hand, to estimate the AP-diameter of the IVC, it is not necessary to fully segment the IVC contour; and hence, we can exploit a reduced model such as a circle which only has three parameters and, consequently, can be estimated more precisely. Fig. 3.3 shows four sample ultrasound images from IVCs with different shapes. For each case, the IVC contour is highlighted with yellow colors and its corresponding AP-diameter is shown with green colors. From Fig. 3.3, one can see that regardless of the shape of the IVC, a circle fitted inside it can accurately model and estimate the IVC AP-diameter.

3.3.2 Proposed Evolution Functional

After exploring a variety of energy and evolution functionals, we heuristically found the following evolution functional to be useful for segmentation of ultrasound images.

$$E = \alpha(u - v)(2I - u - v). \tag{3.7}$$

With the model defined in Section II.A, it is easy to see that if the contour is entirely inside the IVC, then $\bar{I} = u = m_{in}$, with $\bar{I}$ being the average intensity for the points on the contour. Consequently, the evolution functional for contour points is a random variable with the mean value

$$\bar{E} = (u - v)(2\bar{I} - u - v) = (u - v)^2, \tag{3.8}$$

resulting in the contour consistently expanding toward the actual IVC boundary. On the contrary, if the contour is entirely outside the IVC, then $\bar{I} = v = m_{out}$ and the evolution functional for contour points is a random variable with the mean value

$$\bar{E} = (u - v)(2\bar{I} - u - v) = -(u - v)^2, \tag{3.9}$$

resulting in the contour consistently shrinking toward the actual IVC boundary.

To support this finding, we computed the sensitivity of the proposed evolution functional to translation and scaling of the fitted circle.

Fig. 3.4 shows this results with the y-axis being the average contour evolution for the points on fitted circle with $\alpha = 10^{-3}$. Fig. 3.4-(a) shows this averaged functional

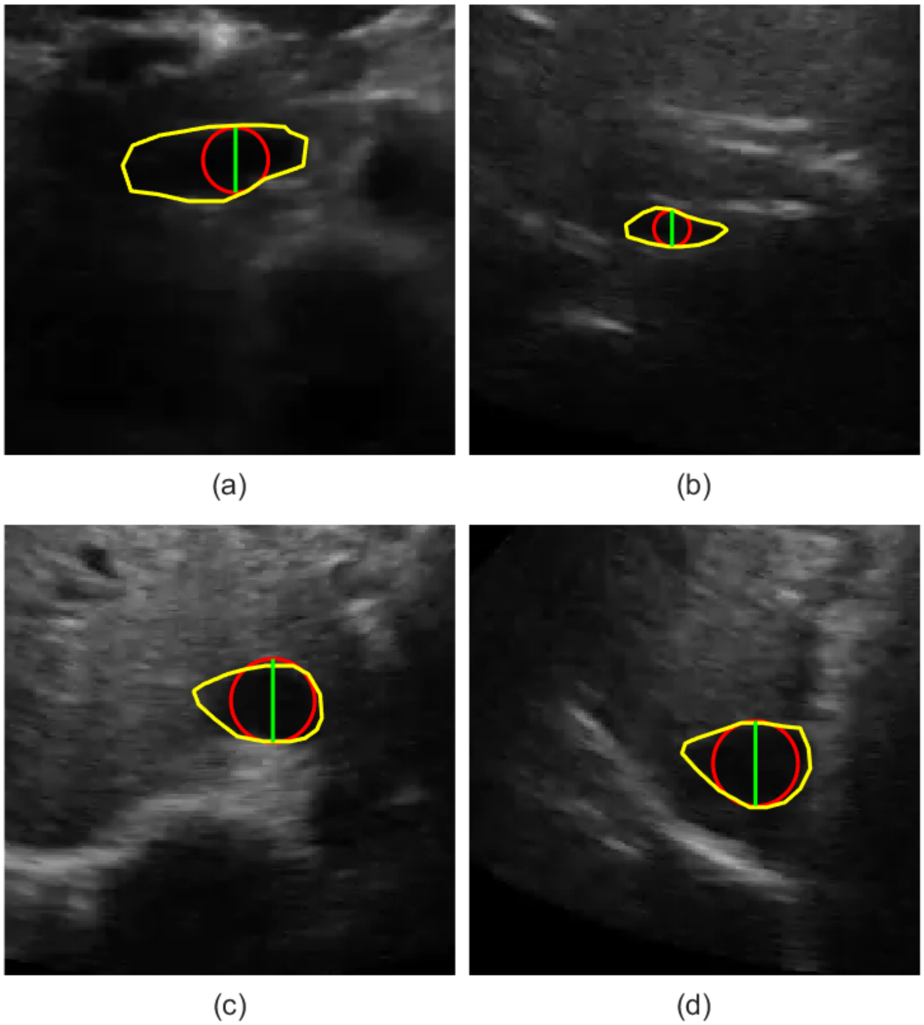

Figure 3.3: Estimation of AP-diameter using circle fitting in IVC images with different shapes and qualities.

when the circle diameter equals to AP-diameter but its center is shifted by δ_x along the x-axis. From 3.4-(a), one can see that when the fitted circle is shifted toward the left, i.e, with $\delta x < 0$, the average evolutional functional is positive, moving the fitted circle to the right, and vice versa. The circle evolution only stops when the average evolutional functional is zero which occurs at $\delta x = 0$. One can see a similar result for the transverse axis in Fig. 3.4-(b). This proves that with the proposed evolutional functional, the algorithm reaches equilibrium when the circle centers on the IVC. Fig. 3.4-(c) shows this result versus the circle diameter, i.e., functional averaged over the points on the circle with diameter D and concentric with the IVC center. From Fig. 3.4-(c), one can see that when the circle diameter is less than D_{AP} of the IVC, the evolutional functional is positive demonstrating that the contour is expanding toward the actual IVC boundaries. This proves that with the proposed functional, the algorithm reaches its equilibrium if $D = D_{AP}$, i.e., when the diameter of the circle equals to the actual AP-diameter of the vessel.

3.3.3 Circle Evolution

The evolution functional is utilized to update the parameters of the circle with R and (x_c, y_c) as its radius and center, respectively. Initially, the circle is sampled at K points with polar angles $\theta_k = \frac{2k\pi}{N}$, $k = 0, 1, ..., K-1$, where the normal vector and Cartesian coordinates corresponding to the kth sampled point notated as

$$\vec{n}_k = [\cos(\theta_k), \sin(\theta_k)]^T, \tag{3.10}$$

and

$$[x_k, y_k]^T = [x_c, y_c]^T + R\vec{n}_k, \tag{3.11}$$

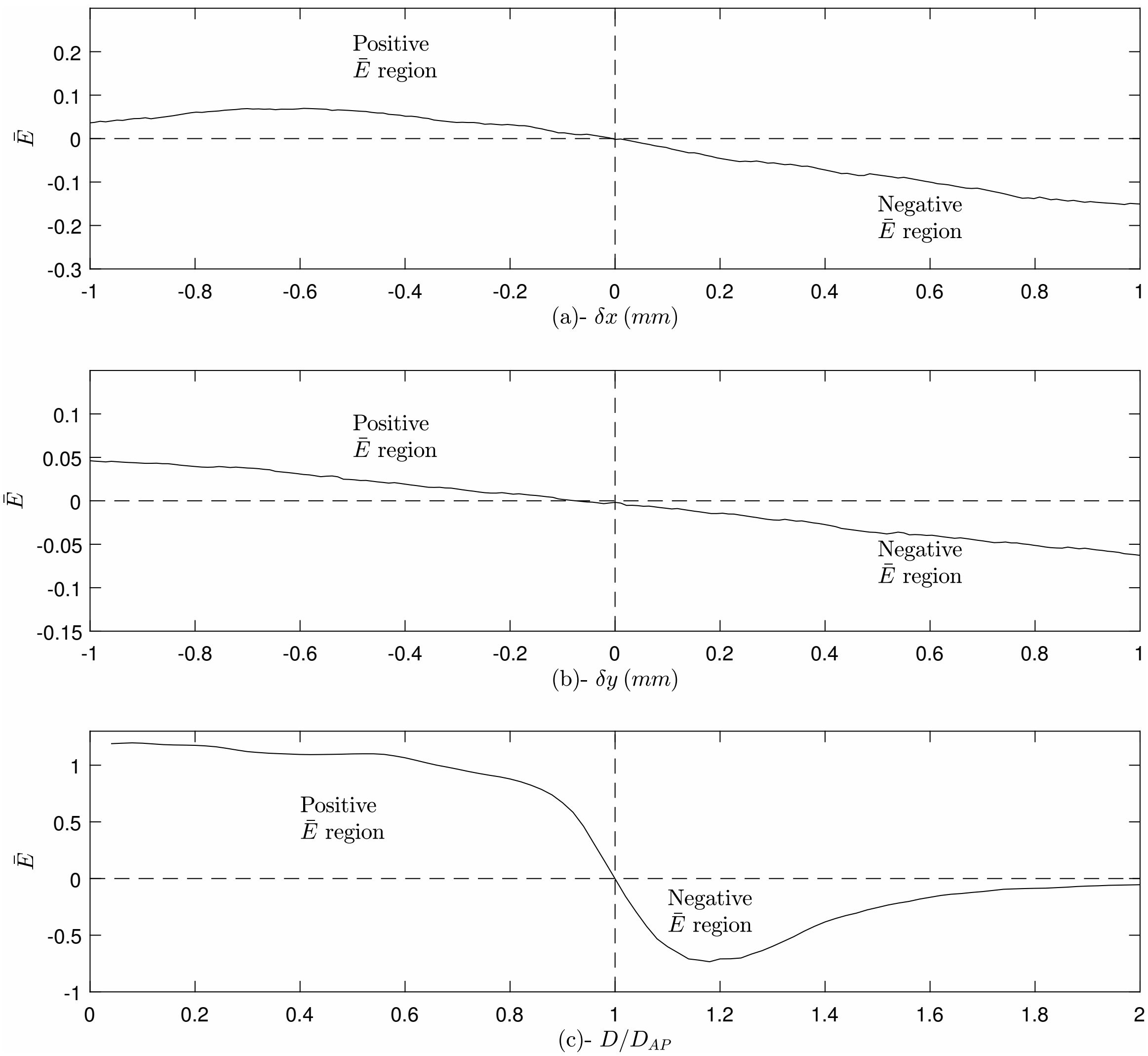

Figure 3.4: Proposed evolution functional versus (a)- δx, (b)- δy, and (c)- normalized circle diameter D/D_{AP} with $\alpha = 10^{-3}$.

respectively. The evolution functional generates forces $f_k = \alpha(u - v)(2I_k - u - v)$ along the normal vectors $n_k, k = 0, 1, ..., K - 1$, as shown in Fig. 3.5. The forces shift the sampled contour points to new positions governed by

$$[\tilde{x}_k, \tilde{x}_k] = [x_c, y_c]^T + (R + f_k)\vec{n}_k. \tag{3.12}$$

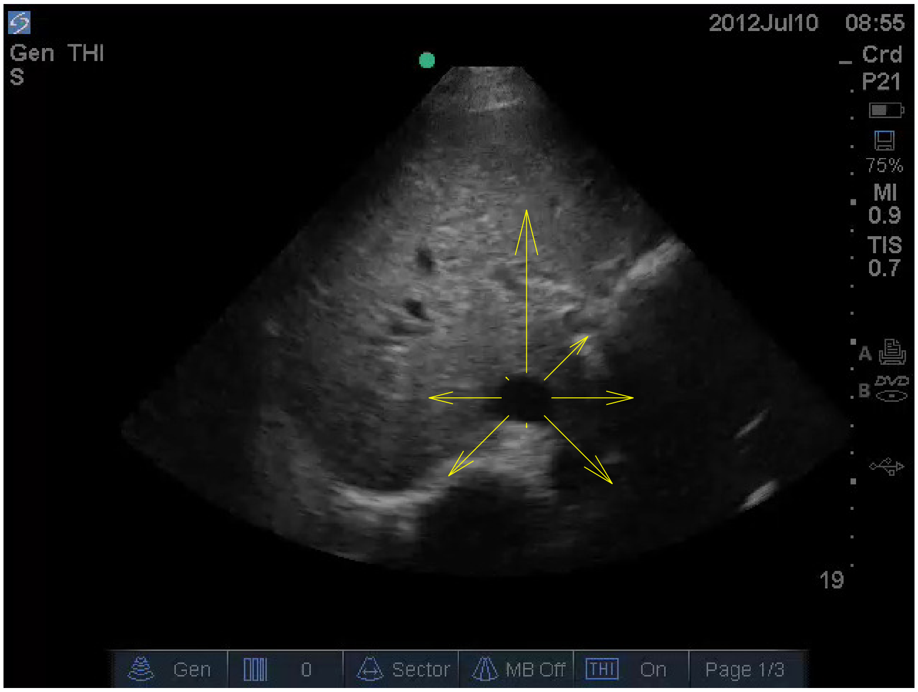

Figure 3.5: The forces generated by the evolution functional in (3.7) with $\alpha = 0.05$ and $K = 8$ (values are adjusted for illustration purposes).

where f_k is the value of the evolution functional at kth contour point. Obviously, the shifted contour points are not on a circle anymore; hence, a new circle needs to be fitted to the updated contour points. This is accomplished through minimization of the following energy functional:

$$C_{circle} = \sum_{k=0}^{K-1} [(\tilde{x}_k - \tilde{x}_c - \tilde{R}\cos(\theta_k))^2 + (\tilde{y}_k - \tilde{y}_c - \tilde{R}\sin(\theta_k))^2], \qquad (3.13)$$

where $[\tilde{x}_c, \tilde{y}_c]$ and $\tilde{R}_c$ are the center and radius of the updated circle. By minimizing C_{circle}, the new values for the center and radius of the circle are obtained using the following theorems.

Theorem 3.3.1. *For a given set of forces, the circle center is shifted by the average* *of the force vectors* $f_k\vec{n}_k$*.*

Proof. To find $\tilde{x}_c$ and $\tilde{y}_c$, the energy functional (C_{circle}) in (3.13) is minimized by setting its gradient to zero as:

$$\frac{\partial C_{circle}}{\partial \tilde{x}_c} = -2\sum_{k=0}^{K-1}(\tilde{x}_k - \tilde{x}_c - \tilde{R}\cos(\theta_k)) = 0, \tag{3.14}$$

$$\frac{\partial C_{circle}}{\partial \tilde{y}_c} = -2\sum_{k=0}^{K-1}(\tilde{y}_k - \tilde{y}_c - \tilde{R}\sin(\theta_k)) = 0. \tag{3.15}$$

Since $\sum\limits_{k=0}^{K-1}\cos(\theta_k) = \sum\limits_{k=0}^{K-1}\sin(\theta_k) = 0$, by subsisting (3.13) in (3.14) and (3.15), one can easily find

$$[\tilde{x}_c, \tilde{y}_c] = [x_c, y_c] + \frac{1}{K}\sum_{k=0}^{K-1} f_k\vec{n}_k, \tag{3.16}$$

highlighting that the circle center is shifted by the average of the force vectors $f_k\vec{n}_k$.

Theorem 3.3.2. *For a given set of forces, the circle radius is modified with the average of the force values* f_k*.*

Proof. To find the new circle radius $\tilde{R}$, the energy functional (C_{circle}) in (3.13) is minimized by setting its gradient to zero as:

$$\begin{aligned}\frac{\partial C_{circle}}{\partial \tilde{R}} &= -2\sum_{k=0}^{K-1}[(\tilde{x}_k - \tilde{x}_c - \tilde{R}\cos(\theta_k))\cos(\theta_k) \\ &+ (\tilde{y}_k - \tilde{y}_c - \tilde{R}\sin(\theta_k))\sin(\theta_k)] = 0.\end{aligned} \tag{3.17}$$

By substituting (3.16) in (3.17), one determines that

$$\tilde{R} = R + \frac{1}{K}\sum_{k=0}^{K-1} f_k. \tag{3.18}$$

3.3.4 Proposed Active Circle Algorithm

In this Chapter we set $K = 32$ and $\alpha = 10^{-4}$. Note that with a larger value of K, the estimation accuracy is improved at the cost of increased computational complexity. Similarly, with an smaller value of α the accuracy is improved at the cost of increased number of iterations required to reach the convergence. The flowchart of the algorithm is shown in Fig. 3.6. As the first step, the proposed algorithm requests to manually locate the IVC. This is simply performed by a mouse click on a point inside the IVC. The initial circle centers at this selected point and to avoid convergence to a wrong boundary, its radius is assumed to be as small as 6 pixels. In the second step, we compute the forces f_k using (3.7). In the third step, these forces to evolve the circle parameters using (3.16) and (3.18). Steps two and three are repeated until either a convergence or maximum number of iterations, i.e., 5000 iterations is achieved. In this Chapter, we assume the algorithm has converged, if the largest force computed in the second step is less than 10^{-3} pixels. This process is repeated for the next frames of the videos.

3.3.5 Complexity Analysis

The complexity of the proposed active circle algorithm is obviously much less than the state-of-the-art algorithms. The algorithm obtains its low complexity from: 1) the simplicity of the proposed evolutional 2) the simplicity of the circle model which only has three parameters to estimate. In this Section, we estimate the computational complexity of the active-circle algorithm using the number of floating point operations (flops) [25]. Assume N_{iter} is the average number of iterations and $A_{max} = 5000$ pixels is the maximum area of the circle. From equations (3.7), (3.16), and (3.18), one can see that the maximum number of flops for each frame is $N_{flops} = (2A_{max} + 3K +$

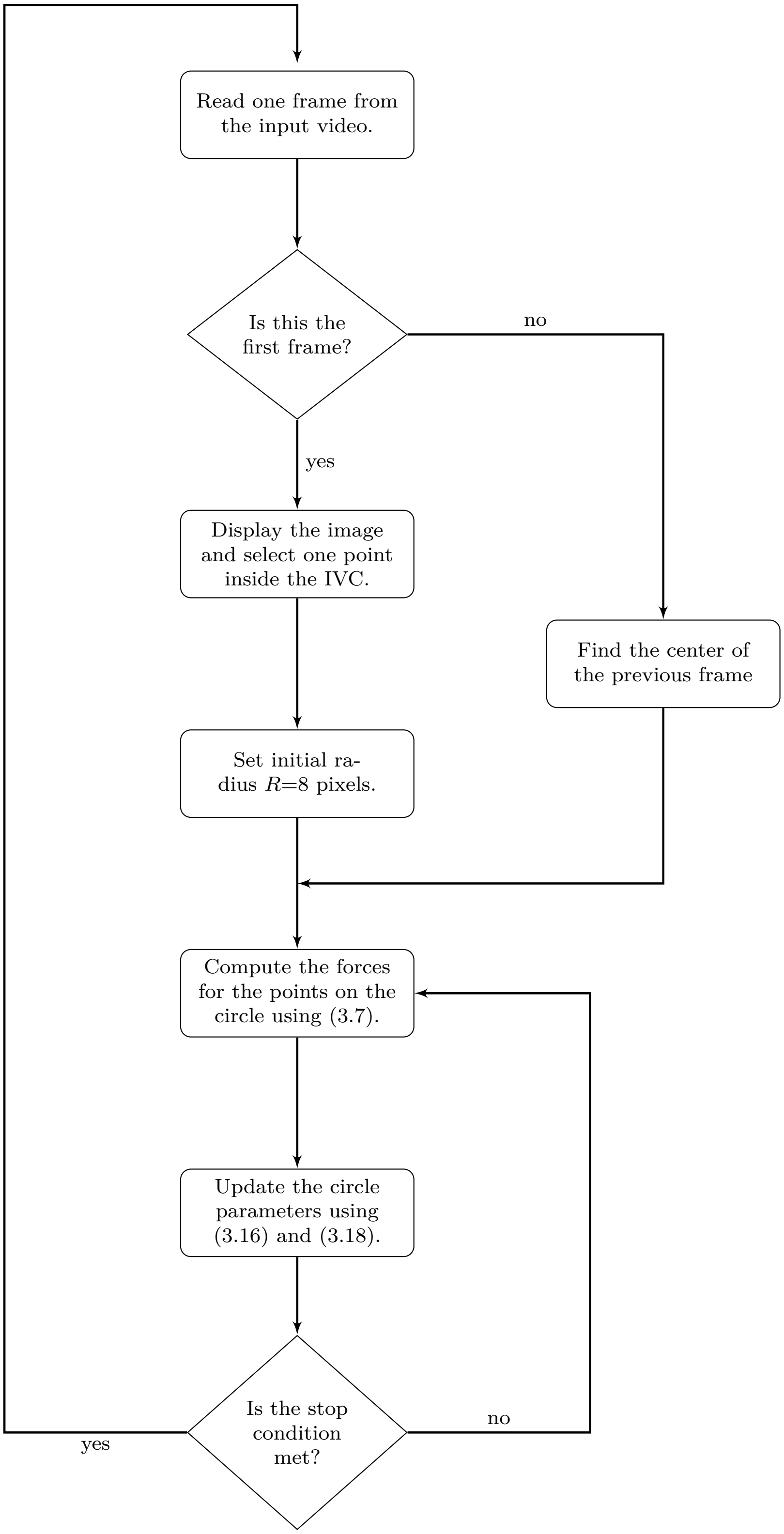

Figure 3.6: Flowchart of the proposed active-circle algorithm.

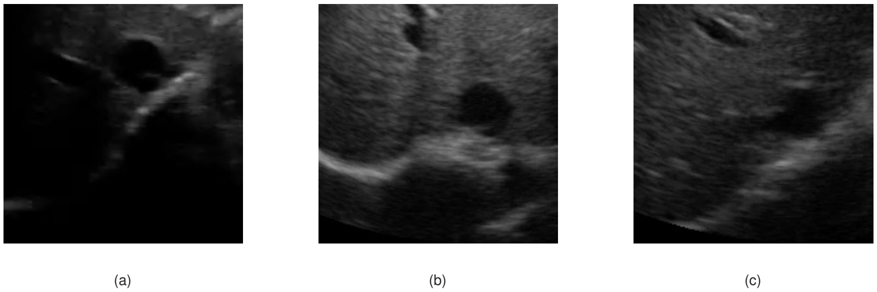

Figure 3.7: First frame of three sample IVC videos rated as (a)- good, (b)- average, and (c)- poor quality videos.

5)$N_{iter} \approx 50$ million flops, i.e., with an average i7-3770 Intel processor, estimation of AP-diameter from each frame requires less than 1 millisecond.

3.4 Results

The experimental data was collected from eight healthy male subjects with ages from 21 to 35. The study protocol was reviewed and approved by the Health Research Ethics Authority. The IVC was imaged in the transverse plane using a porTable ultrasound (M-Turbo, Sonosite-FujiFilm) with a phased-array probe (1-5 Mhz). Each video has a frame rate of 30 fps, scan depth of 19cm, and a duration of 15 seconds (450 frames/clip). Fig. 3.7 depicts the first frame of three subjects with different qualities which are graded, based on their quality and clinical impression, by three experts, including Dr. Andrew Smith as a point-of-care ultrasound expert and two additional clinicians. Note that although the sample image in Fig. 3.7-(b) seems to have a better quality than the one in Fig. 3.7-(a), it is rated as average quality due to its more fuzzy boundaries which degraded the accuracy of the algorithm.

3.4.1 Comparison of the proposed functional with state-of-the-art functionals

In this Section, we first compare the proposed evolution functional with manual measurements made by Dr. Andrew Smith, and two state-of-the-art evolution functionals in eqs. (3.4) and (3.6). The proposed and the two state-of-the-art functionals were implemented with MATLAB2018a. From Fig. 3.8, one can see that in all three investigated videos, the active circle algorithm using the two state-of-the-art functionals fail to track the relatively fast AP-diameter variations in the first video. This is because, in IVC images $A_u \ll A_v$, and hence in eqs. (4) and (6), the second term is dominated by the first term. Consequently, the balance between the intensities inside and outside the contour is not established. Note that in Fig. 3.8-(c) which presents the results for the third subject, due to the extremely poor quality of this video, the manual measurement is partially missing for the frames in range 297 to 332, as the expert was unable to measure the AP-diameter. The proposed algorithm still estimates the AP-diameter although there is no ground truth for these frames.

3.4.2 Influence of the parameter α on the accuracy of the proposed algorithm

In this section, we investigate the sensitivity of the proposed algorithm to the value of α for the three videos depicted in Fig. 3.7. For this study, we use root mean square (RMS) of error as the performance criterion, with the error e defined as the the difference between the AP-diameter estimated from the proposed algorithm and the manual measurement. For the first two subjects, the RMS of error is calculated over all 450 frames, but for the third video, it is calculated over the first 150 frames, where the manual measurement seems to be reliable. From Fig. 3.9, one can easily

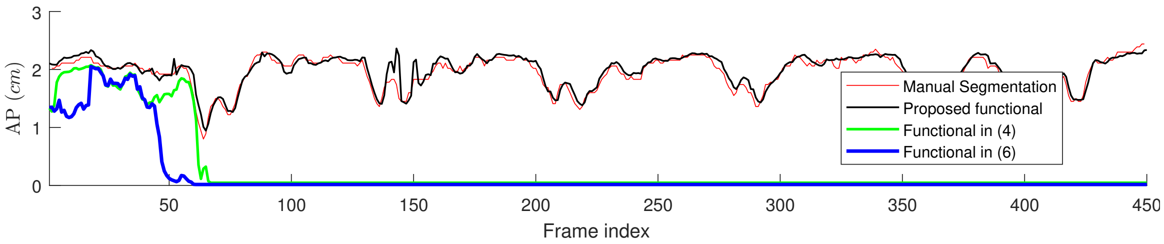

(a)- 1st video

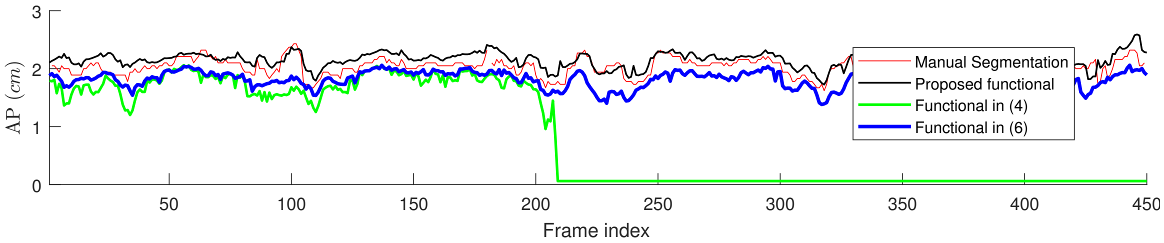

(a)- 2nd video

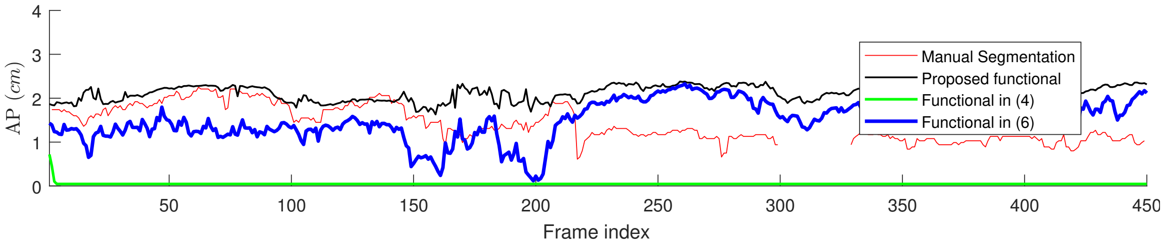

(a)- 3rd video

Figure 3.8: IVC diameter of a typical IVC video as measured by the proposed functional and two functionals in equations (3.4) and (3.6).

see that in all three cases, the proposed algorithm performs well with $\alpha < 5 \times 10^{-4}$. Hence, for the rest of our experiments, we set $\alpha = 10^{-4}$. Note that with a smaller α, more accurate results can be obtained in the cost of more number of iterations required for convergence.

3.4.3 comparison of the proposed algorithm with state-of-the-art segmentation algorithms

The proposed active circle algorithm was also compared with expert manual measurement, the two classic AC algorithms - Chan-Vese [26] and Geodesic [27], and four state-of-the-art polar ACs- PSnake [28] and variational polar AC [29, 30], M3 algo-

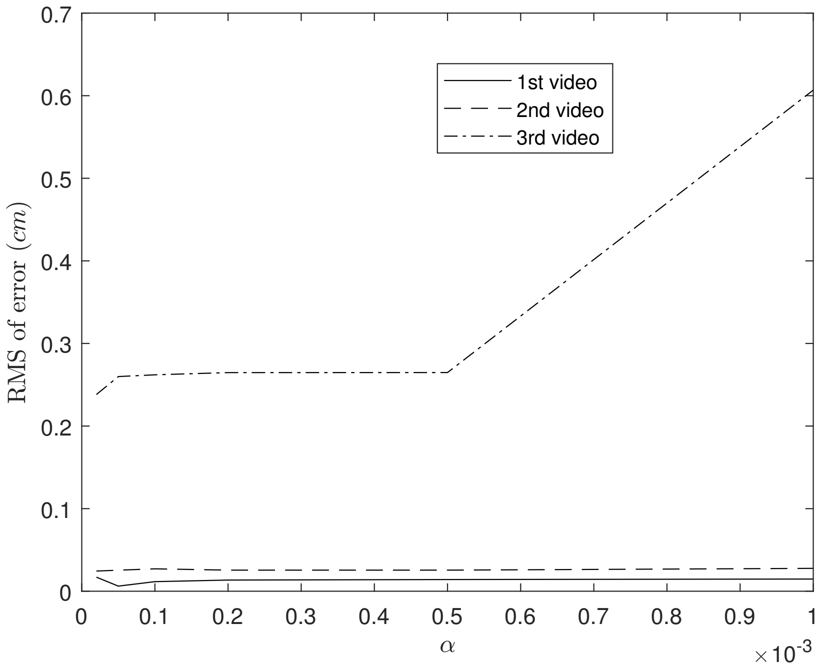

Figure 3.9: The RMS of error for the proposed algorithm w.r.t. the parameter α for the three sample videos depicted in Fig. 3.7.

rithm [21], and Ad-PAC [31], and star-Kalman algorithm [32]. All algorithms were implemented with MATLAB2018a and their parameters were optimized to achieve their maximum accuracy over the test data.

Fig. 3.10-(a) presents the results for the video depicted in Fig. 3.7-(a). This figure illustrates that only the active circle accurately tracks and segments the IVC and follows the variations in manual extraction. M3 algorithm fails to track, whereas the others struggle to capture the temporal variation.

Fig. 3.10-(b) details the results for the video depicted in Fig. 3.7-(b) which suffers from artifact partially occluding the vessel wall. Here, it is evident that the proposed algorithm again tracks the temporal variations of the manual extraction.

Fig. 3.10-(c) details the results for the video depicted in Fig. 3.7-(c) which has a poor quality (the worst among all eight investigated videos). In this case, both the proposed algorithm and manual extraction roughly estimated the AP-diameter for the first 150 frames and then they failed.

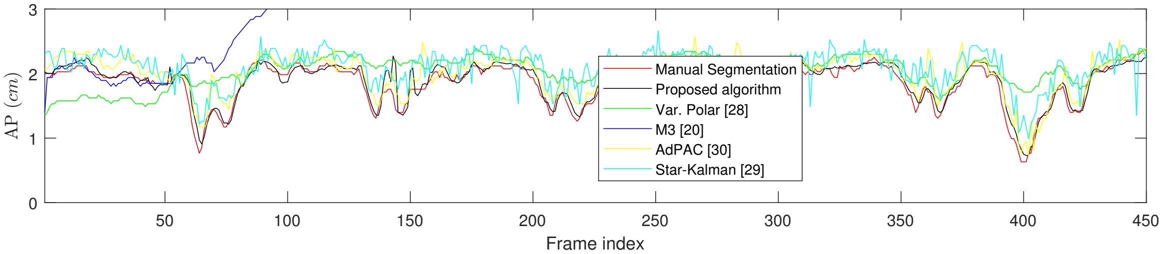

(a)- 1st video

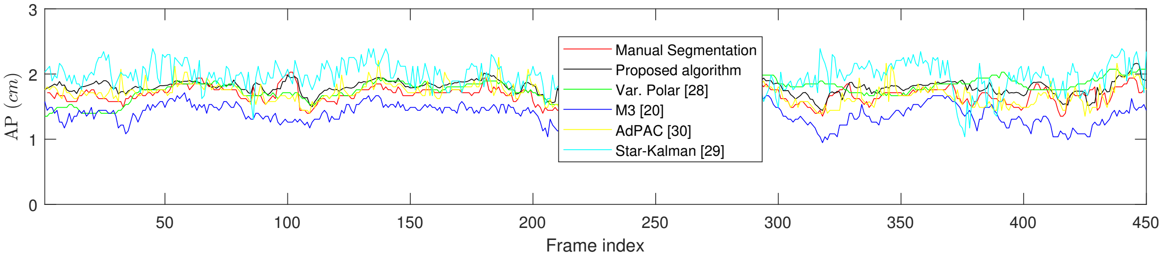

(b)- 2nd video

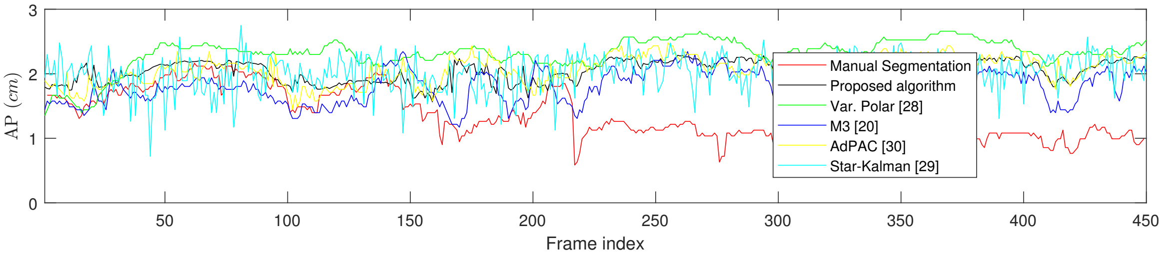

(c)- 3rd video

Figure 3.10: AP-diameter for the three samples videos depicted in Fig. 3.7, as measured by the proposed algorithm, manual extraction, and four other algorithms.

Table 1 presents the RMS of the AP-diameter estimation error for the proposed algorithm and other seven algorithms and for all eight studied subjects, with the last column showing the results averaged over all subjects. Note that videos no. 1 to 3 are the ones depicted in Fig. 3.7. Except the third subject where the manual measurement is reliable only for the first 150 frames (see Fig. 3.10-(c)), for the other seven subject, the RMS of error is calculated over all 450 frames. From this Table, one can see that for all eight studies subjects, the proposed algorithm outperforms other seven methods. The second best performance is obtained from M3 algorithm. One can also see that the Star-Kalman algorithm which fits an ellipse to the IVC contour performs much poorer than the proposed active-circle algorithm. The worst average performance is obtained from the two classic AC algorithms, i.e., Chan-Vese and Geodesic AC, showing that polar ACs perform in average more accurate than the Cartesian ACs because their larger degree of freedom, i.e, the number of parameters that has to be estimated.

Table 3.1: RMS of the AP-diameter estimation error obtained using the proposed algorithm and seven other methods.

Subject no. Method	1	2	3	4	5	6	7	8	Ave
Proposed algorithm	0.10	0.16	0.26	0.16	0.25	0.25	0.1	0.11	0.17
Var. Polar [29]	0.38	0.25	0.49	0.27	0.42	0.28	0.24	0.52	0.36
Psnake [28]	0.66	0.50	0.52	0.5	0.4	0.33	0.49	0.71	0.51
M3 [21]	0.53	0.30	0.24	0.30	0.31	0.32	0.41	0.42	0.35
AdPAC [31]	0.21	0.17	0.2	0.17	0.16	1.1	1.8	0.13	0.39
Star-Kalman [32]	0.34	0.45	0.44	0.45	0.58	0.54	0.37	0.25	0.43
Chan-Vese [26]	1.77	0.39	0.54	0.39	0.38	0.33	0.55	0.73	0.66
Geodesic [27]	1.89	0.17	0.54	0.17	0.38	0.33	0.55	0.73	0.60

3.4.4 More Comparison Metrics

In Table 2, we compare the proposed algorithm and manual estimation using more metrics, where some of these metrics are also clinically useful to assess patient's status. In this Table, e_{ave} is the average estimation error, averaged over the frames in each video; σ_e is the standard deviation of the estimation error e for the frames in each video, and $|e|_{max}$ is the maximum error. Note that e_{ave}, except for the third subject where only the manual measurements for the first 150 frames are reliable, is calculated over all 450 frames. Since the values of D_{max} and D_{min} are useful for the medical purposes, we have also compared them obtained from both the algorithm and manual measurement. Note that subjects no. 1 to 3 are the ones depicted in Fig. 3.7. Furthermore, note that for subject no. 3, i.e., the lowest quality video, these metrics are only calculated for the first 150 frames, where the manual extraction is relatively reliable, while for other seven subjects, they are computed over all 450 frames. From Table 2, one can see that except for the fourth subject, in other cases, D_{max} estimated from the proposed algorithm is very close to the one obtained from the manual measurement and for 5 out of the eight studied subjects, the error for estimation of D_{max} is less than 2mm. Furthermore, in all cases the average error is positive indicating that the proposed algorithm usually overestimates the AP-diameter although this bias is very small and is mostly less than 2mm. Note that this overestimation is mainly due to the fact that the expert extracts the AP-diameter from the inside boundary of IVC. The amount of bias can simply be controlled by adding a constant value to the functional. In all cases, the value σ_e is small indicating that the proposed algorithm performs consistent over different frames of each video.

Table 3.2: Summary of the results of eight studied IVC videos.

Metric \ Subject no.	1	2	3	4	5	6	7	8
e_{ave} (cm)	0.03	0.07	0.07	0.18	0.29	0.37	0.04	0.08
σ_e (cm)	0.06	0.07	0.14	0.08	0.08	0.13	0.09	0.11
$\|e\|_{max}$ (cm)	0.06	0.29	0.43	0.48	0.57	0.75	0.41	0.44
D_{max} alg. (cm)	2.39	2.59	2.3	1.93	2.35	2.29	2.14	2.33
D_{min} alg. (cm)	0.67	0.75	1.7	1.37	1.69	1.38	1.54	1.16
D_{max} man. (cm)	2.43	2.43	2.25	2.41	2.36	2.08	2.21	2.39
D_{min} man. (cm)	0.7	0.66	1.36	0.94	1.34	1.22	1.42	1.21

3.4.5 Influence of speckle removal filtering on the performance of the proposed algorithm

In this subsection, we investigate the influence of different speckle-removal filters on the performance of the proposed algorithm. For this study, we used the proposed algorithm for the images smoothed by either of the the following filters: Bilateral filter [33], 3D block matching filter (BM3D) [34], speckle reducing anisotropic diffusion (SRAD) [35], Wiener filter [36], and median filter.

Fig. 3.11 shows the AP-diameter estimated using the proposed algorithm with each of the above speckle removal filters and have shown their results for the subjects depicted in Fig. 3.7. From Fig. 3.11, one can see that none of these filtering techniques significantly improve the performance of the proposed algorithm. This is mainly due to the fact that the speckle noise in ultrasound images includes useful information that can even improve the performance of computerized algorithms. On the other hand,

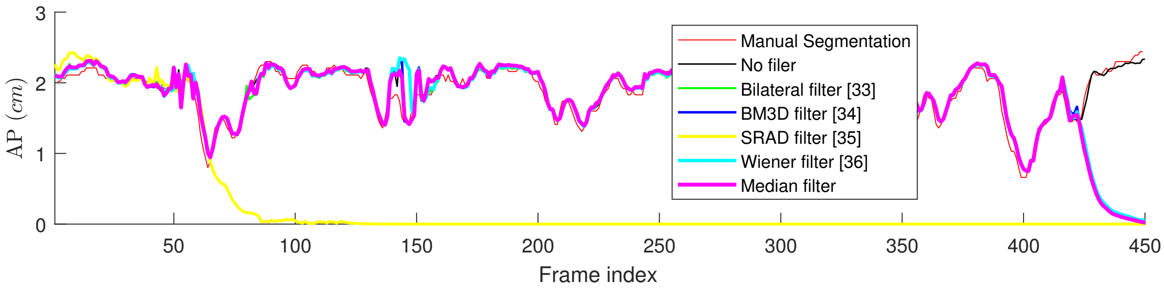

(a)- 1st video

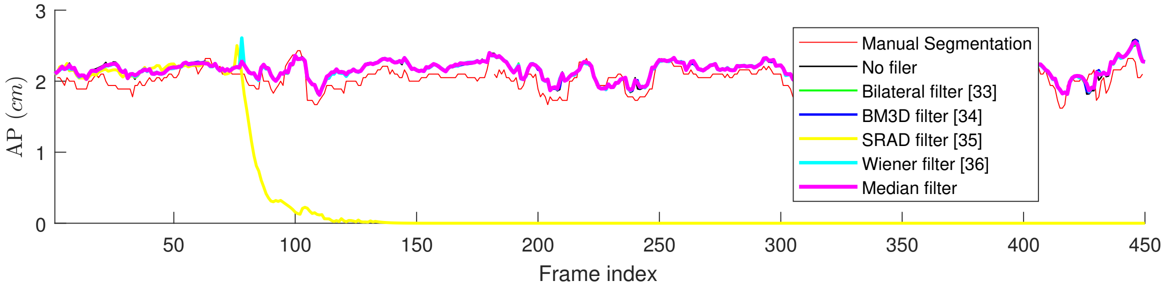

(b)- 2nd video

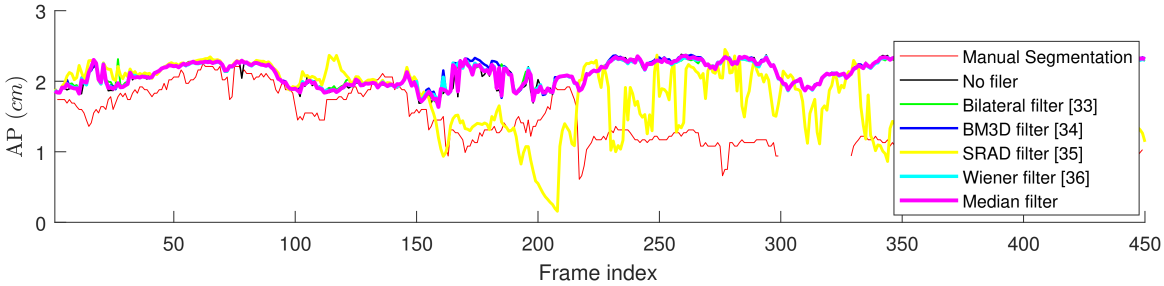

(c)- 3rd video

Figure 3.11: Estimated AP-diameter versus the type of speckle removal filter.

as was discussed in Section III, the proposed algorithm relies on the mean value of the local distributions which usually is not significantly changed by speckle removal filters.

Table 3 presents numerical results to validate this argument. One can see that except the bilateral filter, other speckle-removal filters even degrade the performance and the improvement obtained from the bilateral filter is negligible.

Table 3.3: RMS of error obtained from the proposed algorithm with different speckle removal filters.

Subject no. Metric	1	2	3	4	5	6	7	8
No. filter	0.10	0.16	0.26	0.33	0.25	0.25	0.10	0.12
Bilteral filter [33]	0.11	0.16	0.28	0.32	0.24	0.24	0.10	0.11
BM3D [34]	0.48	0.16	0.27	0.41	0.68	0.26	0.10	0.11
SRAD [35]	1.78	1.81	0.34	0.50	0.78	0.73	0.10	0.11
Wiener filter [36]	0.48	0.17	0.26	0.34	0.43	0.25	0.10	0.12
Median filter	0.48	0.17	0.26	0.36	0.53	0.25	0.10	0.12

3.5 Conclusion

In this Chapter, a novel active circle algorithm is developed for estimating the AP-diameter of the IVC in ultrasound imagery. It has been shown that the diameter of a circle fitted inside the IVC can accurately model the AP-diameter and therefore, is a useful tool capable of supporting further clinical research of using the IVC to guide fluid resuscitation. Furthermore, a novel evolution functional has been proposed and used for updating the circle parameters. Experimental results suggest that the proposed algorithm performs very close to the expert manual measurements. The proposed algorithm only failed under extremely low image-quality scenarios when the AP-diameter was even unable to be measured by the expert.

References

[1] Vassilios Smyrniotis, Georgia Kostopanagiotou, Kassiani Theodoraki, Dimitrios Tsantoulas, and John C Contis. The role of central venous pressure and type of vascular control in blood loss during major liver resections. *The American journal of surgery*, 187(3):398–402, 2004.

[2] Emanuel Rivers, Bryant Nguyen, Suzanne Havstad, Julie Ressler, Alexandria Muzzin, Bernhard Knoblich, Edward Peterson, and Michael Tomlanovich. Early goal-directed therapy in the treatment of severe sepsis and septic shock. *New England Journal of Medicine*, 345(19):1368–1377, 2001.

[3] Cyril Charron, Vincent Caille, Francois Jardin, and Antoine Vieillard-Baron. Echocardiographic measurement of fluid responsiveness. *Current opinion in critical care*, 12(3):249–254, 2006.

[4] Lakshmi Durairaj and Gregory A Schmidt. Fluid therapy in resuscitated sepsis: less is more. *Chest Journal*, 133(1):252–263, 2008.

[5] Christophe Barbier, Yann Loubières, Christophe Schmit, Jan Hayon, Jean-Louis Ricôme, François Jardin, and Antoine Vieillard-Baron. Respiratory changes in inferior vena cava diameter are helpful in predicting fluid responsiveness in ventilated septic patients. *Intensive care medicine*, 30(9):1740–1746, 2004.

[6] Weiming Wang, Lei Zhu, Jing Qin, Yim-Pan Chui, Bing Nan Li, and Pheng-Ann Heng. Multiscale geodesic active contours for ultrasound image segmentation using speckle reducing anisotropic diffusion. *Optics and Lasers in Engineering*, 54:105–116, 2014.

[7] Suresh Sudha, GR Suresh, and R Sukanesh. Speckle noise reduction in ultrasound

images by wavelet thresholding based on weighted variance. *International journal of computer theory and engineering*, 1(1):7, 2009.

[8] Robert F Wagner, Stephen W Smith, John M Sandrik, and Hector Lopez. Statistics of speckle in ultrasound b-scans. *IEEE transactions on sonics and ultrasonics*, 30(3):156–163, 1983.

[9] José C Seabra, Francesco Ciompi, Oriol Pujol, Josepa Mauri, Petia Radeva, and Joao Sanches. Rayleigh mixture model for plaque characterization in intravascular ultrasound. *IEEE Transactions on Biomedical Engineering*, 58(5):1314–1324, 2011.

[10] Marcelo Pereyra, Nicolas Dobigeon, Hadj Batatia, and Jean-Yves Tourneret. Segmentation of skin lesions in 2-d and 3-d ultrasound images using a spatially coherent generalized rayleigh mixture model. *IEEE transactions on medical imaging*, 31(8):1509–1520, 2012.

[11] TA Tuthill, RH Sperry, and KJ Parker. Deviations from rayleigh statistics in ultrasonic speckle. *Ultrasonic imaging*, 10(2):81–89, 1988.

[12] Michael Kass, Andrew Witkin, and Demetri Terzopoulos. Snakes: Active contour models. *International journal of computer vision*, 1(4):321–331, 1988.

[13] E Karami, M Shehata, P McGuire, and A Smith. A semi-automated technique for internal jugular vein segmentation in ultrasound images using active contours. In *2016 IEEE-EMBS International Conference on Biomedical and Health Informatics (BHI)*, pages 184–187. IEEE, 2016.

[14] Bo Liu, HD Cheng, Jianhua Huang, Jiawei Tian, Xianglong Tang, and Jiafeng Liu. Probability density difference-based active contour for ultrasound image segmentation. *Pattern Recognition*, 43(6):2028–2042, 2010.

[15] Mohammad Talebi, Ahamd Ayatollahi, and Ali Kermani. Medical ultrasound image segmentation using genetic active contour. *Journal of Biomedical Science and Engineering*, 4(02):105, 2011.

[16] J Alison Noble. Ultrasound image segmentation and tissue characterization. *Proceedings of the Institution of Mechanical Engineers, Part H: Journal of Engineering in Medicine*, 224(2):307–316, 2010.

[17] Peter J Yim and David J Foran. Volumetry of hepatic metastases in computed tomography using the watershed and active contour algorithms. In *Computer-Based Medical Systems, 2003. Proceedings. 16th IEEE Symposium*, pages 329–335. IEEE, 2003.

[18] Sahirzeeshan Ali and Anant Madabhushi. An integrated region-, boundary-, shape-based active contour for multiple object overlap resolution in histological imagery. *IEEE transactions on medical imaging*, 31(7):1448–1460, 2012.

[19] Kensuke Nakamura, Makoto Tomida, Takehiro Ando, Kon Sen, Ryota Inokuchi, Etsuko Kobayashi, Susumu Nakajima, Ichiro Sakuma, and Naoki Yahagi. Cardiac variation of inferior vena cava: new concept in the evaluation of intravascular blood volume. *Journal of Medical Ultrasonics*, 40(3):205–209, 2013.

[20] Maximilian Baust et al. *Polar Active Contours for Medical Applications.* PhD thesis, Technische Universität München, 2012.

[21] E Karami, M Shehata, and A Smith. Segmentation and tracking of inferior vena cava in ultrasound images using a novel polar active contour algorithm. In *5th IEEE Global Conference on Signal and Information Processing, GlobalSIP2017*, pages 1–5. IEEE, 2017.

[22] Chunming Li, Chenyang Xu, Changfeng Gui, and Martin D Fox. Level set evolution without re-initialization: a new variational formulation. In *Computer Vision and Pattern Recognition, 2005. CVPR 2005. IEEE Computer Society Conference on*, volume 1, pages 430–436. IEEE, 2005.

[23] Daniel Cremers, Stanley J Osher, and Stefano Soatto. Kernel density estimation and intrinsic alignment for shape priors in level set segmentation. *International journal of computer vision*, 69(3):335–351, 2006.

[24] Anthony Yezzi, Lilla Zöllei, and Tina Kapur. A variational framework for integrating segmentation and registration through active contours. *Medical image analysis*, 7(2):171–185, 2003.

[25] David S Watkins. *Fundamentals of matrix computations*, volume 64. John Wiley & Sons, 2004.

[26] Tony F Chan and Luminita A Vese. Active contours without edges. *IEEE Transactions on image processing*, 10(2):266–277, 2001.

[27] Vicent Caselles, Ron Kimmel, and Guillermo Sapiro. Geodesic active contours. *International journal of computer vision*, 22(1):61–79, 1997.

[28] Auzuir Ripardo De Alexandria, Paulo Cesar Cortez, Jessyca Almeida Bessa, John Hebert da Silva Felix, Jose Sebastiao De Abreu, and Victor Hugo C De Albuquerque. psnakes: A new radial active contour model and its application in the segmentation of the left ventricle from echocardiographic images. *Computer methods and programs in biomedicine*, 116(3):260–273, 2014.

[29] Maximilian Baust, Anthony J Yezzi, Gozde Unal, and Nassir Navab. A sobolev-type metric for polar active contours. In *Computer Vision and Pattern Recognition (CVPR), 2011 IEEE Conference on*, pages 1017–1024. IEEE, 2011.

[30] Maximilian Baust and Nassir Navab. A spherical harmonics shape model for level set segmentation. In *European Conference on Computer Vision*, pages 580–593. Springer, 2010.

[31] Ebrahim Karami, Mohamed S Shehata, and Andrew Smith. Adaptive polar active contour for segmentation and tracking in ultrasound videos. *IEEE Transactions on Circuits and Systems for Video Technology*, 2018. doi: 10.1109/TCSVT.2018.2818072.

[32] Julian Guerrero, Septimiu E Salcudean, James A McEwen, Bassam A Masri, and Savvakis Nicolaou. Real-time vessel segmentation and tracking for ultrasound imaging applications. *IEEE transactions on medical imaging*, 26(8):1079–1090, 2007.

[33] Carlo Tomasi and Roberto Manduchi. Bilateral filtering for gray and color images. In *Computer Vision, 1998. Sixth International Conference on*, pages 839–846. IEEE, 1998.

[34] Kostadin Dabov, Alessandro Foi, Vladimir Katkovnik, and Karen Egiazarian. Image denoising by sparse 3-d transform-domain collaborative filtering. *IEEE Transactions on image processing*, 16(8):2080–2095, 2007.

[35] Yongjian Yu and Scott T Acton. Speckle reducing anisotropic diffusion. *IEEE Transactions on image processing*, 11(11):1260–1270, 2002.

[36] Christos P Loizou and Constantinos S Pattichis. Despeckle filtering algorithms and software for ultrasound imaging. *Synthesis lectures on algorithms and software in engineering*, 1(1):1–166, 2008.

Chapter 4

Estimation and Tracking of the IVC AP-diameter Using Active Shape Models

Acutely-ill patients with conditions such as sepsis, trauma, and congestive heart failure require judicious resuscitation in order to achieve and maintain optimal circulating blood volume. Increasingly, emergency and critical care physicians are using porTable ultrasound to approximate the temporal changes of the anterior-posterior (AP)-diameter of the inferior vena cava (IVC) in order to guide fluid administration or removal. This Chapter proposes semi-automatic active ellipse and rectangle algorithms capable of improved and quantified measurement of the AP-diameter. The proposed algorithms are compared to manual measurement and a previously published active circle model. Results demonstrate that the rectangle model outperforms both active circle and ellipse irrespective of IVC shape and closely approximates tedious frame-by-frame expert assessment.

4.1 Introduction

Acutely-ill patients with conditions such as sepsis, trauma, and congestive heart failure require judicious resuscitation in order to achieve and maintain optimal circulating blood volume while avoiding increased morbidity and mortality[1, 2, 3, 4]. Increasingly, emergency and critical care physicians visually approximate the AP-diameter of the IVC using porTable ultrasound in order to guide fluid management on these patients [5, 6, 7]. Unfortunately, ultrasound image quality is highly operator-dependent, images contain considerable noise, and image artifacts frequently impede accurate manual or computerized segmentation [8, 9].

Speckle noise present in ultrasound imagery is theoretically considered to be a Rayleigh distributed multiplicative noise [10] as the envelope of the ultrasound wave reflected from each tissue has a Rayleigh distribution. Hence, Rayleigh mixture models have been proposed as a solution for ultrasound image segmentation [11, 12]. However, it has been shown that due to the scattering population and signal processing, the speckle distribution deviates from Rayleigh[13]. In [14], authors proposed a fast algorithm based on optical flow for tracking of the speckles in ultrasound images. This approach fails when the speckle structure is rapidly deformed.

Active contours (ACs) are widely used for segmentation of ultrasound images [15, 16, 17, 18, 19, 20]. ACs convert the problem of image segmentation into a minimization of an energy functional with their performance frequently dependent on a manually-defined initialization contour. In order to avoid local minima, the initiating contour needs to be as close as possible to the actual contour. ACs can be combined with other segmentation algorithms as a coarse-to-fine strategy to reduce the impact of the initial contour on segmentation error [21, 22]. Researchers have addressed the challenge of IVC segmentation using this strategy by using a template matching method as the coarse segmentation and AC for fine-tuning (TMAC) [23]. Unfortunately, this approach fails when the IVC undergoes large frame-to-frame variations commonly present on porTable machines with lower frame rates (e.g. 30 frames-per-second). Additionally, ACs continue to perform poorly in the context of fuzzy or unclear boundaries as is commonly the case for the IVC.

Given that the cross-section of the IVC is largely convex, the IVC contour can be represented in polar coordinates and consequently, polar active contours appear to be a promising solution for IVC segmentation [24]. In [25], a polar AC model based on the third centralized moment (M3) was proposed for segmentation of IVC images. Unfortunately, M3 algorithm roughly estimates the cross-sectional area (CSA) of the IVC and fails with poor quality images. In [26], adaptive polar AC algorithm was proposed for segmentation of ultrasound images, where the parameters of the AC models are locally and temporally adapted as frame by frame basis. This approach fails with poor quality IVC images [27].

Accurate segmentation algorithms such as the one proposed in this manuscript have the potential to expand understanding into non-invasive volume status monitoring. Clinical research has demonstrated that the true angle of collapse is actually 25 degrees off vertical rather than the simple AP-diameter [28].

In [27], the off-axis collapse was appropriately modeled using the diameter of a circle fitted inside the IVC with good results. However, tools capable of measuring the CSA, AP-diameter, and off-axis collapse are needed. In this Chapter, we propose two algorithms based on elliptical and rectangular models. The height of a thin rectangle fitted inside the IVC can efficiently model its clinically measured AP-diameter. We also develop another algorithm based on ellipse fitting just for the purpose of comparison.

The remainder of this Chapter is organized as follows - Section 2 discusses the background and related work. The proposed active rectangle and active ellipse algorithms are presented in Section 3 while experimental results are given in Section 4, the results are discussed in Section 5 and the Chapter is concluded in Section 6.

4.2 Background and Related Work

In [27], the authors showed that the AP-diameter of the IVC can be accurately modeled with the diameter of a circle fitted inside the IVC. The active circle algorithm proposed in [27] is based on the following evolution functional:

$$E = \alpha(u - v)(2I - u - v), \tag{4.1}$$

where u and v are the mean of the intensities for the pixels inside and outside the contour, respectively, and I is the intensity of the pixels on the contour. This functional is used to evolve the parameters of the circle, i.e., R as the circle radius and (x_c, y_c) as its center coordinates. For this, the circle is sampled at K points with polar angles $\theta_k = \frac{2k\pi}{N}$, $k = 0, 1, ..., K - 1$, where the normal vector and the Cartesian coordinates corresponding to the kth sampled point are denoted by

$$\vec{n}_k = [\cos(\theta_k), \sin(\theta_k)]^T, \tag{4.2}$$

and

$$[x_k, y_k]^T = [x_c, y_c]^T + R\vec{n}_k, \tag{4.3}$$

respectively. The evolutional functional generates forces f_k along the normal vectors as

$$f_k = \alpha(u - v)(2I_k - u - v). \tag{4.4}$$

These forces move the contour points to their new positions as

$$[\tilde{x}_k, \tilde{x}_k] = [x_c, y_c]^T + (R + f_k)\vec{n}_k, \tag{4.5}$$

where f_k is the value of the evolution functional at kth contour point. It is shown that the average evolution functional approaches zero when the contour points are on the IVC boundary. In active circle algorithm, the center of the circle is evolved as

$$[\tilde{x}_c, \tilde{y}_c] = [x_c, y_c] + \frac{1}{K}\sum_{k=0}^{K-1} f_k\vec{n}_k, \tag{4.6}$$

where $[x_c, y_c]$ and $[\tilde{x}_c, \tilde{y}_c]$ are the center coordinates of the circle before and after evolution, respectively, and f_k is the evolution force for the kth contour point obtained from (3.7), and $\vec{n}_k$ is its corresponding normal vector that can be obtained as

$$\vec{n}_k = [\cos(\theta_k), \sin(\theta_k)]^T, \tag{4.7}$$

Eq. (3.16) indicates that the circle center point is simply translated by the average of the force vectors $f_k\vec{n}_k$. The radius of the circle is evolved as

$$\tilde{R} = R + \frac{1}{K}\sum_{k=0}^{K-1} f_k. \tag{4.8}$$

where R and $\tilde{R}$ is the radius of the circle before and after evolution, respectively. This indicates that the circle radius is evolved with the average of the force magnitudes f_k.

4.3 Proposed Algorithms

In this section, we develop active ellipse and rectangle models based on the evolution functional proposed in [27].

4.3.1 Active Ellipse Model

In [27], authors showed that the active circle algorithm estimates the IVC AP-diameter much more accurately than the star-Kalman algorithm in [29] which is based on ellipse fitting. But does this indicate that a circular model can estimate the AP-diameter more accurately than an elliptical model? To answer this question, we develop an active ellipse algorithm based on the same evolutional functional as the one employed in the active circle algorithm.

In the general case, during evolution, the kth contour point is evolved as

$$[\tilde{x}_k, \tilde{x}_k] = [x_k, y_k]^T + f_k \vec{n}_k. \tag{4.9}$$

The next step is to evolve the ellipse parameters using the evolved contour points. Unlike the circular model, the evolved ellipse parameters are not linearly related to evolved contour points. This non-linearity may result in convergence to local minima. To avoid this, at each iteration, we fit a new ellipse using the following conic equation. Note that since the algorithm still operates iteratively, the ellipse parameters are gradually evolving and hence, we call this algorithm an active ellipse algorithm.

$$ax^2 + bxy + cy^2 + dx + ey = 1, \tag{4.10}$$

where x and y are the coordinates of the points on the conic, a, b, c, d, and e are the conic parameters. Note that with an elliptical model, the values of a and b must be positive. With K points with coordinates $[\tilde{x}_k, \tilde{x}_k]$, the best ellipse is fitted by minimizing the following cost function.

$$C = \sum_{k=1}^{K} (a\tilde{x}_k^2 + b\tilde{x}_k\tilde{y}_k + c\tilde{y}_k^2 + d\tilde{x}_k + e\tilde{y}_k - 1)^2 \tag{4.11}$$

Eq. (4.11) can be rewritten in matrix form

$$C(A) = A^T X^T X A + 2\mathbf{1}_K^T X A + K, \tag{4.12}$$

where the vector of conic parameters defined as $A = [a, b, c, d, e]^T$, X is a matrix with $[\tilde{x}_k^2, \tilde{x}_k\tilde{y}_k, \tilde{y}_k^2, \tilde{x}_k, \tilde{y}_k]$ as its kth row, $\mathbf{1}_K$ is $K \times 1$ all-one vector, and superscript T is the transpose operator. After setting the gradient of $C(A)$ to zero, the vector A is obtained as

$$\hat{A} = -\mathbf{1}_K^T X (X^T X)^{-1}. \tag{4.13}$$

Fig. 4.1 presents the flowchart for the proposed active ellipse algorithm. As shown in the flowchart, only for the first frame, an operator needs to manually select a point inside the IVC and the rest of the algorithm works automatically. For each frame, the ellipse parameters are iteratively updated using (4.4), (4.9) and (4.13) until a convergence is reached. We assume that the algorithm has reached convergence when the maximum of the change in the elements of the A is less than 10^{-4}, i.e., when $max(|\hat{A}_n - \hat{A_{n-1}}|)$, where max is the element-wise maximum, and $\hat{A}_n$ is the vector A estimated at nth iteration. After convergence, the algorithm proceeds with the next frame. Fig. 4.2 shows the ellipse evolution versus the number of iterations for a sample IVC frame.

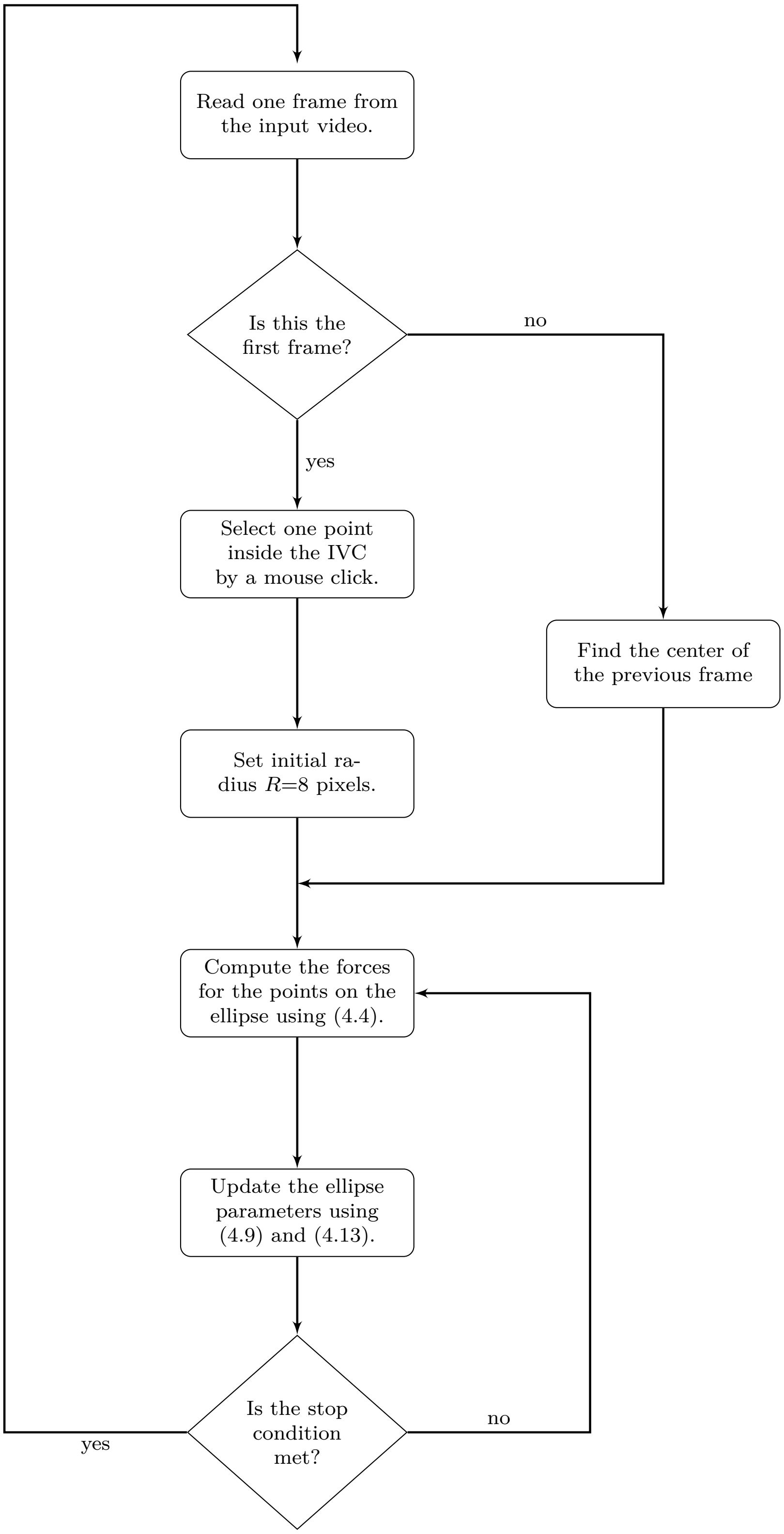

Figure 4.1: Flowchart for the proposed active ellipse algorithm for estimation and tracking of the IVC AP-diameter from ultrasound videos.

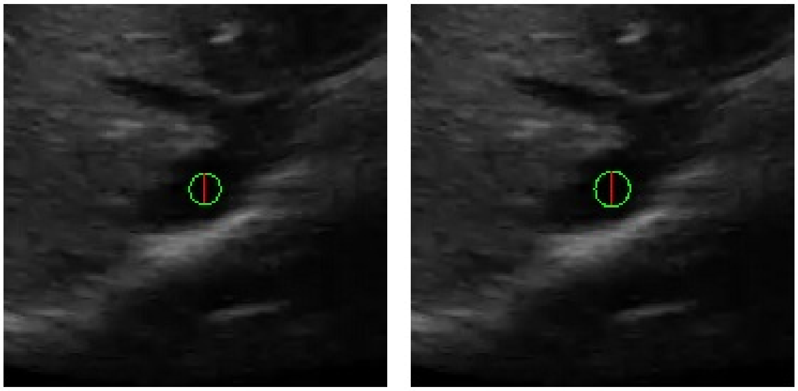

1st iteration 10th iteration

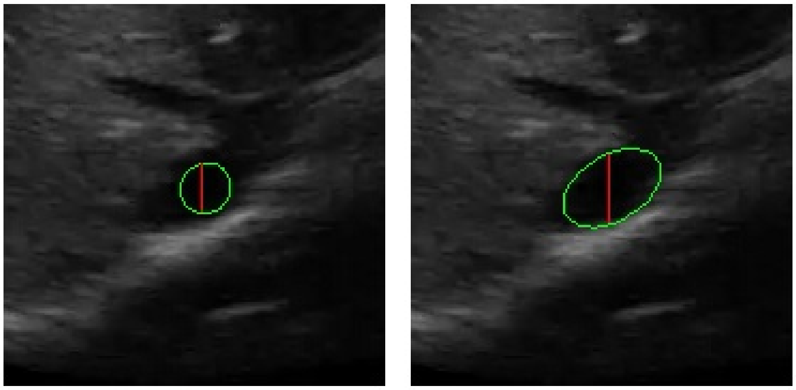

50th iteration 200th iteration

Figure 4.2: The ellipse evolution versus number of iterations.

4.3.2 Active Rectangle Model

The intuition to use a rectangular model is that the AP-diameter is clinically defined as the largest vertical diameter of the IVC contour which may practically deviate from the actual diameter of an circle or even an ellipse. The AP-diameter can be modeled as the height of a vertical thin rectangle. As a starting point, we assume that the fitted rectangle has a fixed width w=3 pixels and the only parameters that have to be modified are the center and the height of the rectangle. With the forces defined as (4.1), either of the upper and lower sides of the rectangle move with the average of the forces applied on that side. Hence, the center of the rectangle is shifted as

$$\tilde{x}_c = x_c + \frac{1}{K_l} \sum_{p \in P_l} f_p - \frac{1}{K_r} \sum_{p \in P_r} f_p, \tag{4.14}$$

$$\tilde{y}_c = y_c + \frac{1}{K_u} \sum_{p \in P_u} f_p - \frac{1}{K_b} \sum_{p \in P_b} f_p, \tag{4.15}$$

where P_l, P_r, P_u, and P_b are the subsets of the contour points on the left, right, upper, and lower sides of the rectangle, respectively, and K_l, K_r, K_u, and K_b are the number of points in each of these sets. Similarly, the height of the rectangle is evolved as

$$\tilde{h} = h + \frac{1}{K_u} \sum_{p \in P_u} f_p + \frac{1}{K_b} \sum_{p \in P_b} f_p. \tag{4.16}$$

Although a thin rectangle model accurately models the clinically measured AP-diameter, it might be lost if parts of the IVC boundaries are missing as the IVC edges are not detected and hence, the algorithm may diverge. To combat this problem, we modify the active rectangle algorithm by starting with a rectangle with a much larger width of w=15 pixels. This rectangle is gradually narrowed to its final width, i.e., w=3 pixels which is narrow enough to model the AP-diameter. The active rectangle algorithm is summarized as the flowchart in Fig. 4.3. As shown in 4.3, similar to the active circle and ellipse algorithms, an operator has to manually select a point inside the IVC and the rest of the algorithm is automatic and does not need further manual intervention. The active rectangle algorithm converges much more quickly than the active circle and ellipse algorithms as the results show that in all cases, no more than N_i=200 iterations are required to reach convergence, while with the other two algorithms, typically up to N_i=5000 iterations are required to reach convergence. Therefore, there is no need to set a stop condition for the active rectangle algorithm.

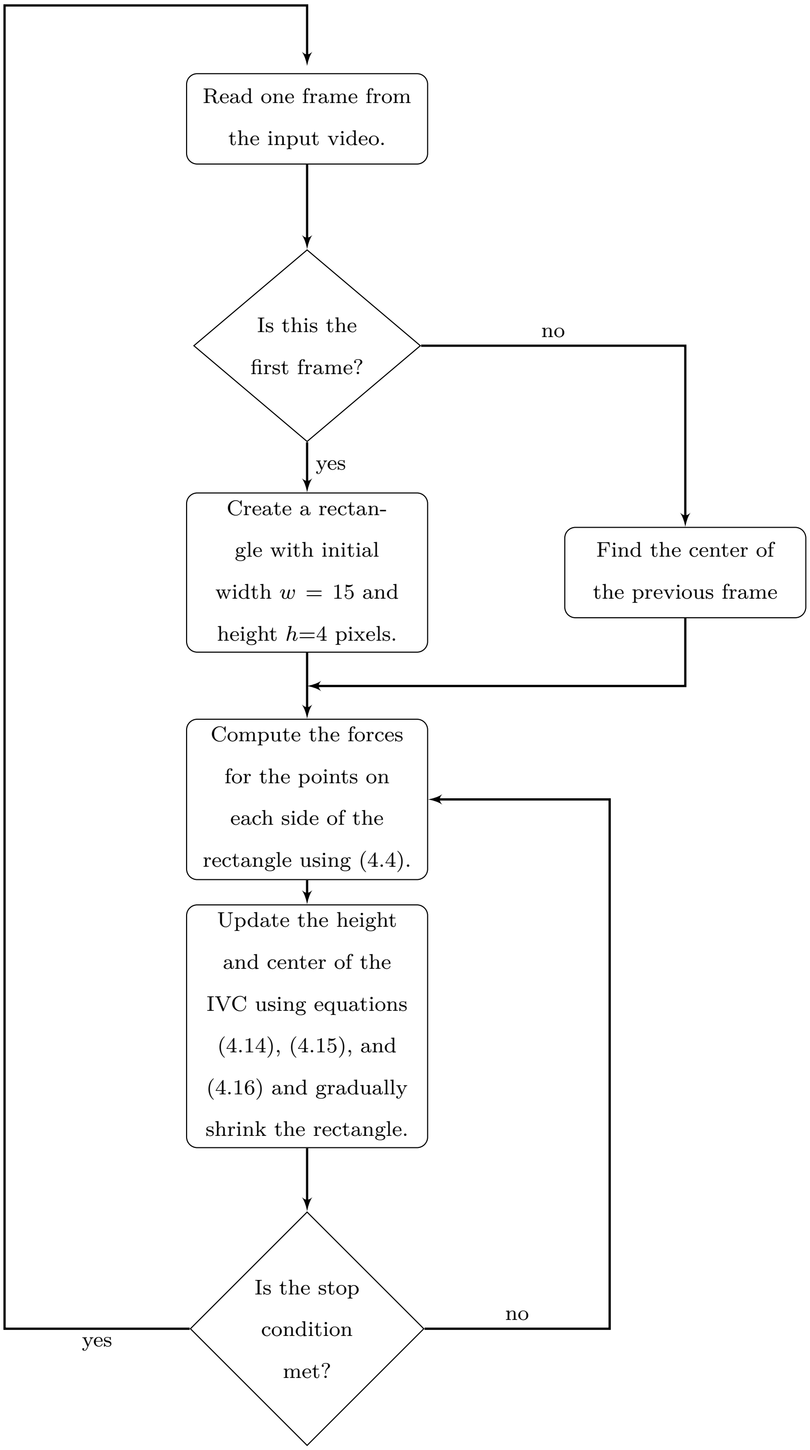

Figure 4.3: Flowchart for the proposed active rectangle algorithm for estimation and tracking of the IVC AP-diameter from ultrasound videos.

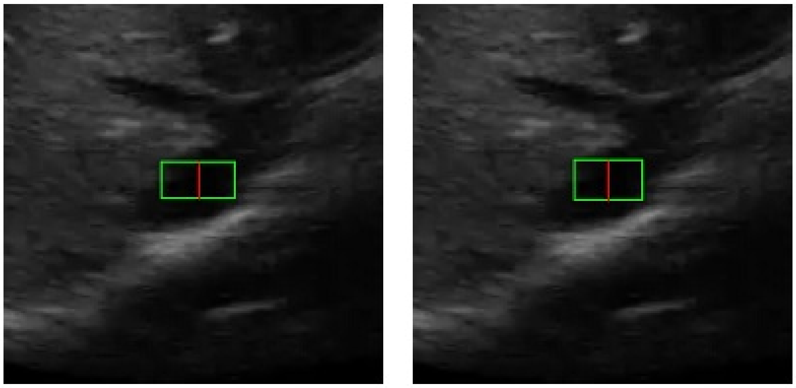

1st iteration 10th iteration

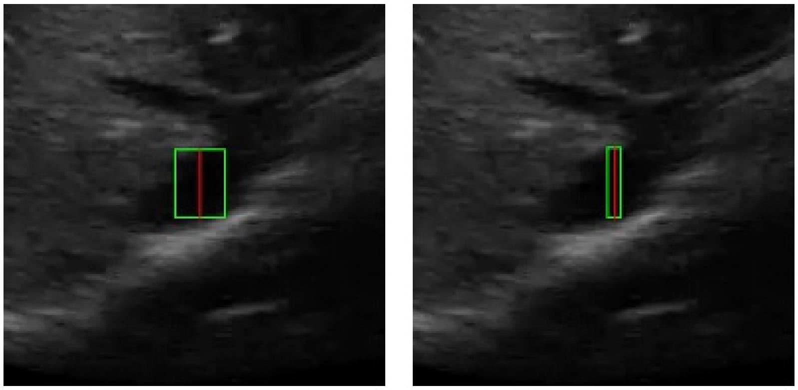

50th iteration 200th iteration

Figure 4.4: The rectangle evolution versus number of iterations.

Fig. 4.4 shows the rectangle evolution versus number of iterations for the IVC image as in Fig. 4.2. By comparison of Figs. 4.2 and 4.4, one can see the active rectangle algorithm not only converges more quickly but also more accurately estimates the AP-diameter than the active ellipse algorithm.

4.4 Results

Ultrasound videos from eight healthy subjects were collected with the IVC imaged in the transverse plane using a portable ultrasound (M-Turbo, Sonosite-FujiFilm) and a phased-array probe (1-5 MHz). The data were collected from twenty subjects. But only for eight cases, the manual measurement seemed reliable to be used as the ground truth. Each video has a frame rate of 30 fps, scan depth of 19 cm, and a duration of 15 seconds (450 frames/clip). All algorithms were implemented with MATLAB2018b. Fig. 4.5 depicts the first frame of all eight subjects. In Fig. 4.5, one can see that an IVC image can have different shapes and qualities. For instance, in clip no. (1), although part of the image is shadowed, the IVC edges are almost visible. The IVC videos for the clips no. (3) and (8) show the lowest quality as the IVC is almost collapsed in the former one and it vanishes after the initial frames in the latter one (this is not seen in this image as it is only the first frame of the video).

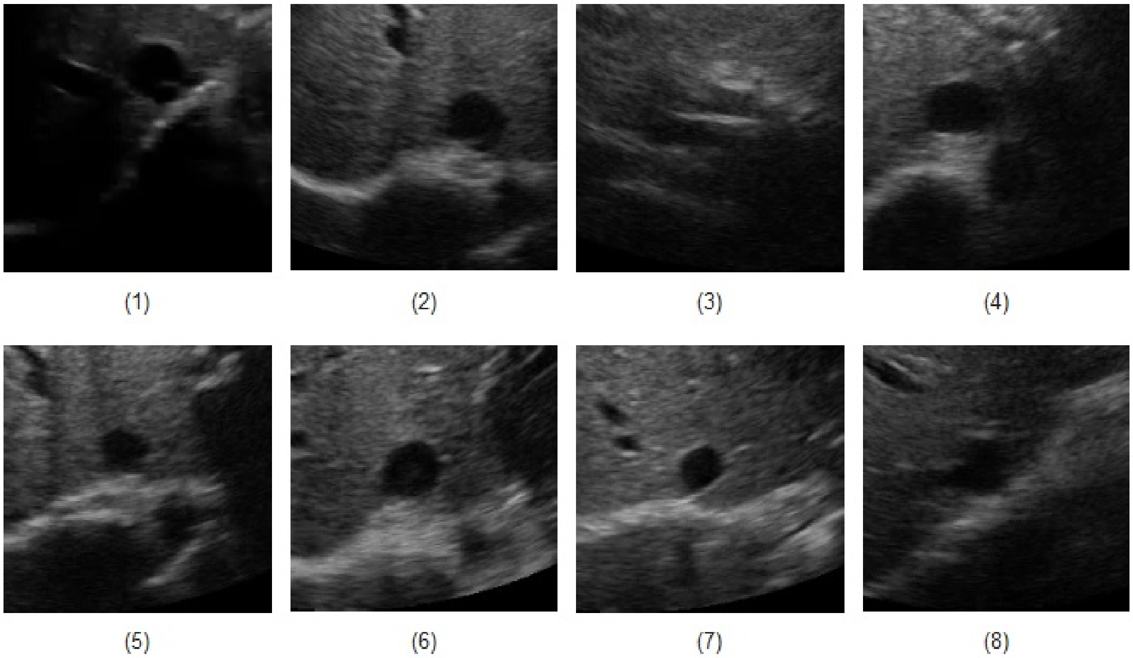

Figure 4.5: The first frame of all eight IVC videos.

4.4.1 Tracking Performance

Figs. 4.6-4.8 present the AP-diameter manually measured by Dr. Andrew Smith as a point-of-care ultrasound expert and the ones that are semi-automatically estimated by the three shape-based algorithms for the first three sample videos depicted as subjects (1)-(3) in Fig. 4.5. From Fig. 4.6, one can see that with the first IVC clip which has a good quality, both active circle and active rectangle algorithms efficiently track the manual measurement, although the active ellipse algorithm roughly tracks the manual measurement and performs more poorly than the other two methods.

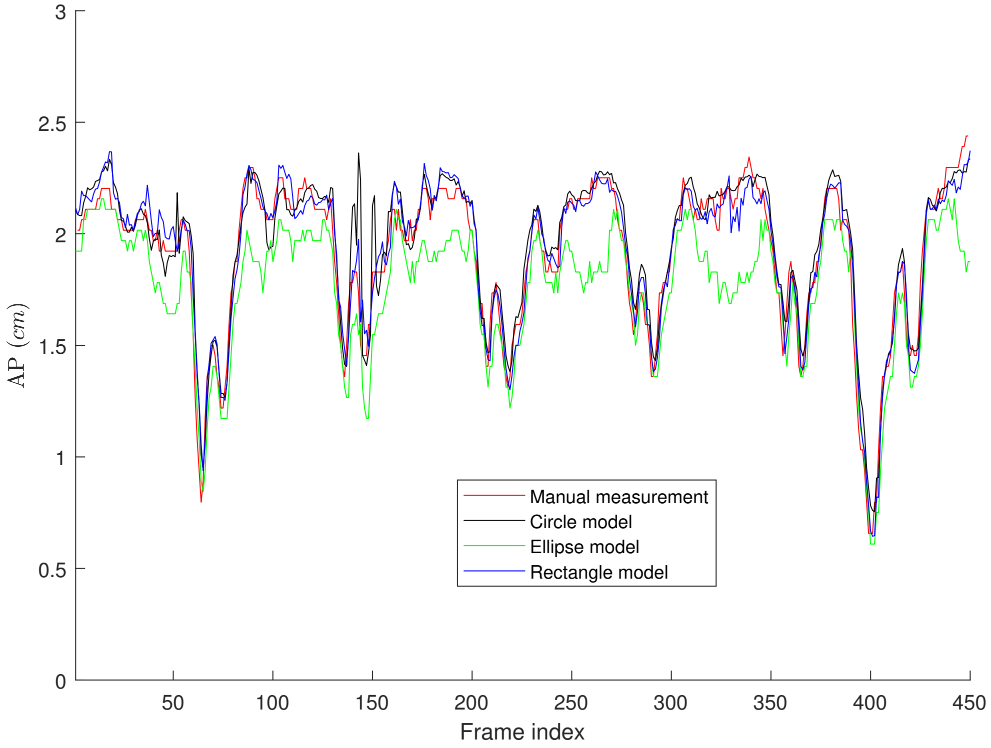

Figure 4.6: AP-diameter for the first video depicted in Fig. 4.5, as measured by the manual measurement (red line), active circle algorithm (black line), active ellipse algorithm (green line) and active rectangle algorithm (blue line).

Fig. 4.7 presents the tracking results for the second clip where one can easily see that all three algorithms perform less accurately than the case in Fig. 4.6. This is mainly due to the fact that although the second clip seems to have a better quality than the first one, it has a more fuzzy contour, making the algorithms less accurate than the first clip. Similar to the first clip, we can see that the active rectangle algorithm performs better than the other two methods.

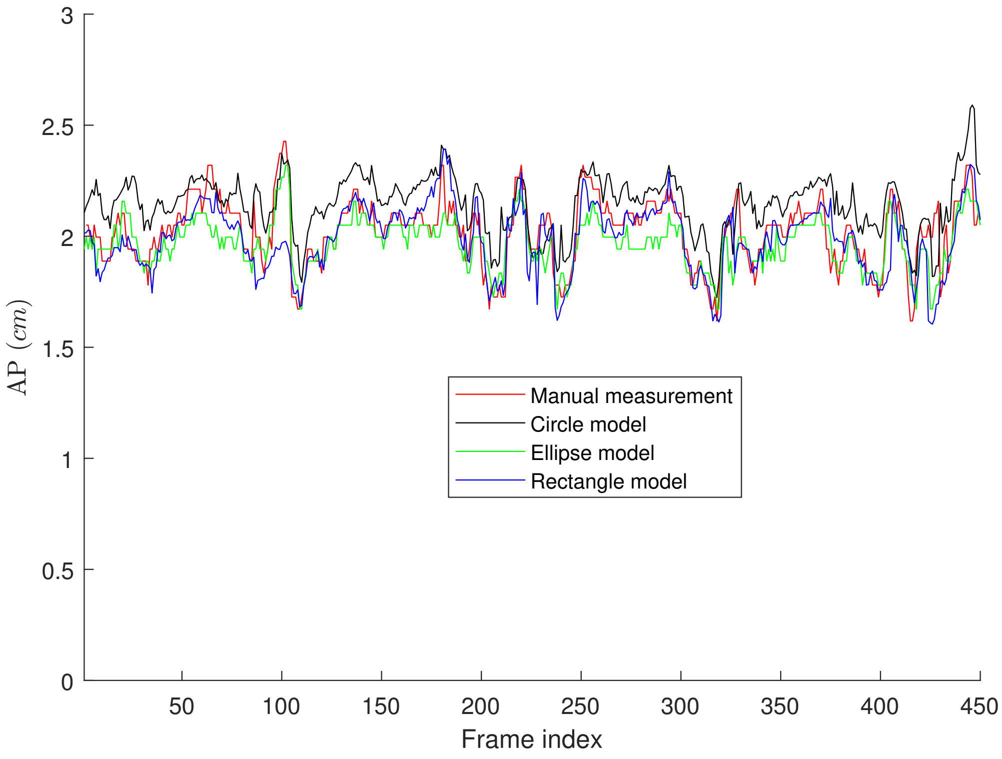

Figure 4.7: AP-diameter for the second video depicted in Fig. 4.5, as measured by the manual measurement (red line), active circle algorithm (black line), active ellipse algorithm (green line) and active rectangle algorithm (blue line).

Fig. 4.8 presents the tracking results for the third video depicted in Fig. 4.5 where the IVC is almost collapsed and therefore, a smaller AP-diameter is expected. In this case, the active circle algorithm loses the tracking after 337 frames, while both active ellipse and active rectangle algorithms efficiently track the result obtained from the manual measurement.

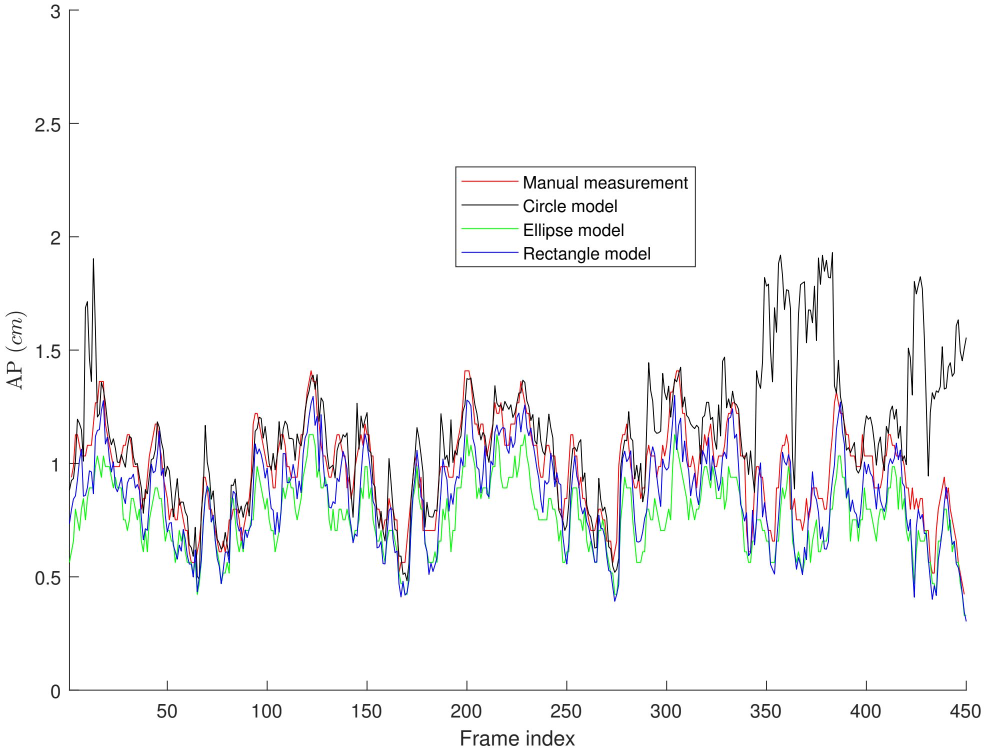

Figure 4.8: AP-diameter for the third sample video depicted in Fig. 4.5, as measured by the manual measurement (red line), active circle algorithm (black line), active ellipse algorithm (green line) and active rectangle algorithm (blue line).

Figs. 4.9-4.11 present the probability distribution function (PDF) of the AP-diameter estimation error for the three videos depicted as subjects (1)-(3) in Fig. 4.5. Here, the error is defined as the difference between the AP-diameter estimated by each of the three shape-based algorithms and the one measured by the expert. From Figs. 4.9-4.11, one can see that for all three investigated scenarios, the active circle algorithm provides a biased measurement. This confirms the similar result reported in [27]. Furthermore, for all three cases the PDF of the error obtained from the active rectangle algorithm is more concentrated around zero than the other two algorithms, indicating the best performance among the three shape-based algorithms.

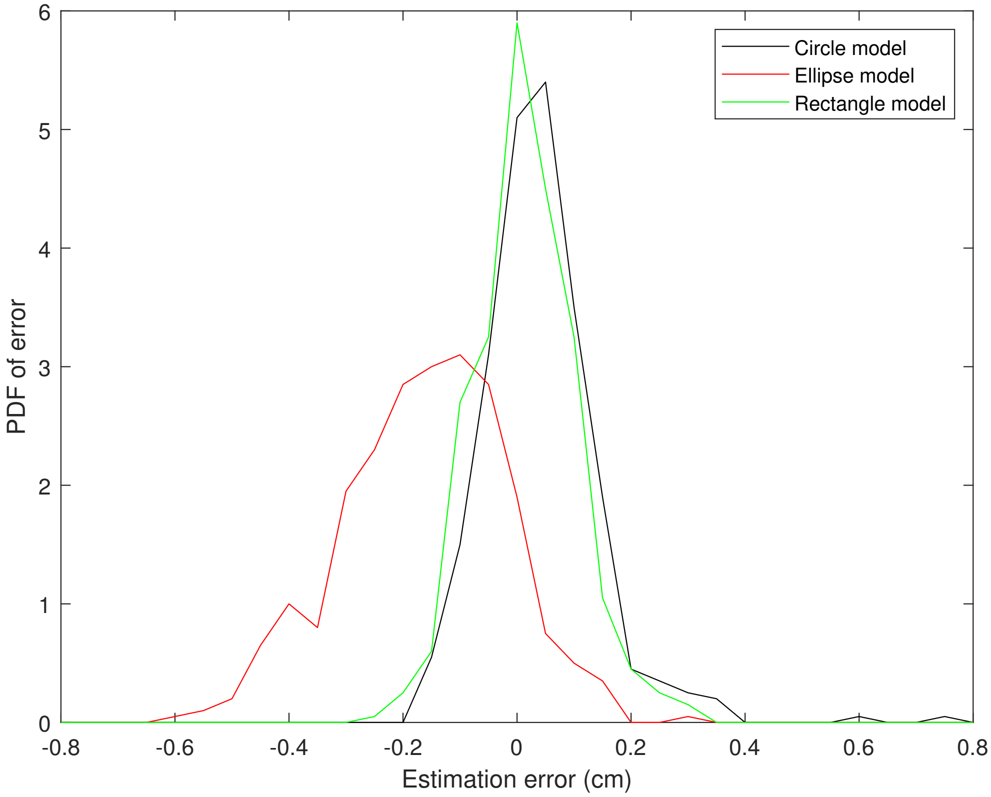

Figure 4.9: PDF of the AP-diameter estimation error w.r.t. manual measurement for the first sample video depicted in Fig. 4.5, as measured by active circle algorithm (black line), active ellipse algorithm (red line) and active rectangle algorithm (green line).

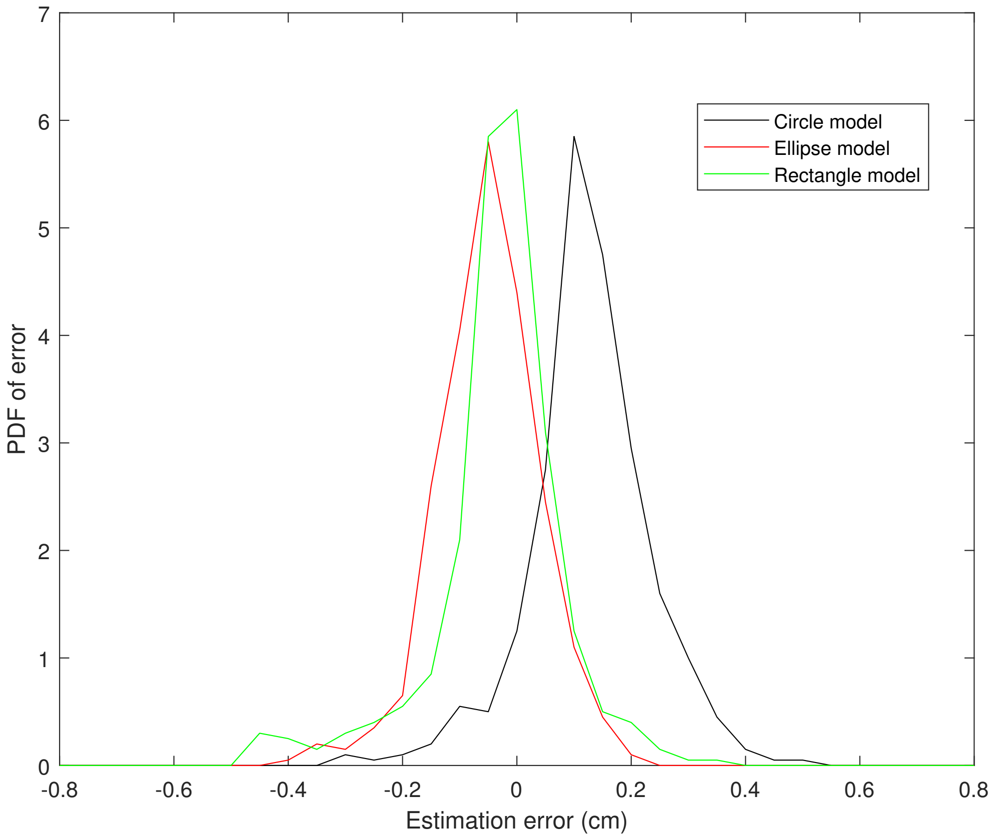

Figure 4.10: PDF of the AP-diameter estimation error w.r.t. manual measurement for the second sample video depicted in Fig. 4.5, as measured by active circle algorithm (black line), active ellipse algorithm (red line) and active rectangle algorithm (green line).

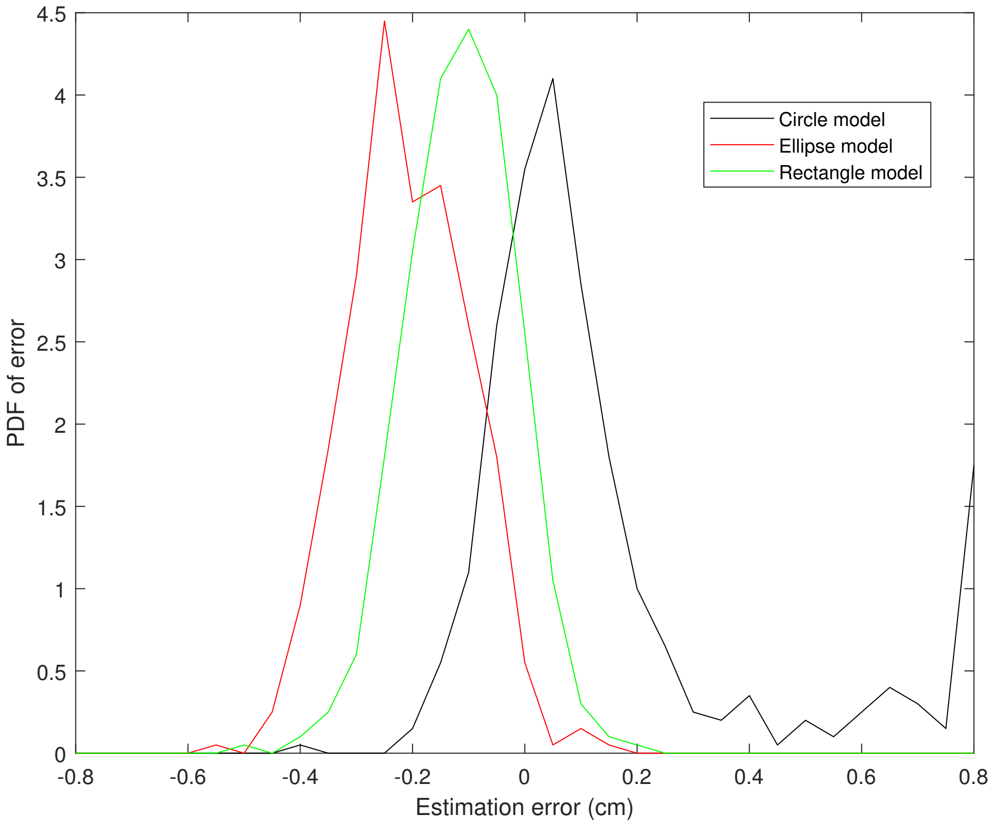

Figure 4.11: PDF of the AP-diameter estimation error w.r.t. manual measurement for the third sample video depicted in Fig. 4.5, as measured by active circle algorithm (black line), active ellipse algorithm (red line) and active rectangle algorithm (green line).

Figs. 4.6-4.11 show that in all three investigated clips, the active rectangle algorithm outperforms the other two methods. To have a better insight about the results, we present numerical results in Tables 1 and 2. Table 1 presents the room mean square (RMS) of the AP-diameter estimation error for the three shape-based algorithms for the all eight clips depicted in Fig. 4.5. Note that the error is defined as the difference between the AP-diameter estimated by each of the algorithms and the one manually measured by the expert. Except with subject no. (8), where manual segmentation is reliable for only the first 150 frames (see [27]), for the other seven subjects, the

RMS of error is calculated over all 450 frames. From this Table, one can see that in all eight investigated cases, the active rectangle algorithm outperforms the other two methods, while in five out of the eight cases, the active circle algorithm performs more accurately than the active ellipse algorithm.

Table 2 presents the maximum absolute value of error obtained for the three algorithms for all eight clips depicted in Fig. 4.5. This Table confirms the results obtained in Table 1, i.e., the active rectangle algorithm always outperforms the other two methods.

Table 4.1: RMS of the AP-diameter estimation error.

Subject **Method**	**(1)**	**(2)**	**(3)**	**(4)**	**(5)**	**(6)**	**(7)**	**(8)**	**Ave.**
Circle model	0.10	0.16	0.16	0.25	0.25	0.10	0.11	0.26	0.17
Ellipse model	0.21	0.19	0.14	0.26	0.18	0.11	0.11	0.20	0.35
Rectangle model	0.08	0.11	0.12	0.23	0.14	0.10	0.10	0.18	0.12

Table 4.2: Maximum absolute value of AP-diameter estimation error.

Subject **Method**	**(1)**	**(2)**	**(3)**	**(4)**	**(5)**	**(6)**	**(7)**	**(8)**
Circle model	0.06	0.29	0.48	0.57	0.75	0.41	0.44	0.43
Ellipse model	0.11	0.32	0.35	0.59	0.48	0.54	0.47	0.38
Rectangle model	0.05	0.18	0.19	0.42	0.28	0.37	0.39	0.29

Table 3 present the correlation between the AP-diameter estimated by each of the three shape-based algorithms and the one measured by the expert. This Table confirms the results obtained in Tables 1 and 2 as in all eight cases, the proposed active rectangle algorithm outperforms the other two algorithms and provides the highest correlation with the manual measurement.

Table 4 present the average position error for each of the three shape-based algorithm versus the one measured by the expert. In this Table, the distance position error is defined as the Euclidean distance (in cm) between the center of the fitted shape (circle, ellipse, or rectangle) and the center of the AP-line manually located by the expert. This also confirms the previous results as in all eight investigated cases the center of the fitted rectangle is closer to the manual measurement than the centers of the fitted circle and ellipse.

Table 4.3: Correlation between the AP-diameters estimated by the three shape-based algorithms and manual measurement.

Subject / **Method**	**(1)**	**(2)**	**(3)**	**(4)**	**(5)**	**(6)**	**(7)**	**(8)**
Circle model	0.9987	0.9987	0.9652	0.7971	0.9985	0.9986	0.9988	0.9958
Ellipse model	0.9974	0.9985	0.9945	0.9981	0.9986	0.9985	0.9991	0.9850
Rectangle model	0.9993	0.9994	0.9949	0.9991	0.9992	0.9991	0.9994	0.9985

Table 4.4: The average position error for the three shape-based algorithms w.r.t. the manual measurement.

Subject **Method**	**(1)**	**(2)**	**(3)**	**(4)**	**(5)**	**(6)**	**(7)**	**(8)**	**Ave.**
Circle model	0.41	0.39	0.63	0.65	0.36	0.49	0.55	0.64	0.51
Ellipse model	0.42	0.43	0.31	0.47	0.44	0.49	0.54	0.56	0.45
Rectangle model	0.37	0.33	0.27	0.28	0.29	0.47	0.54	0.55	0.39

4.5 Discussion

4.5.1 The Performance of the Proposed Algorithms

As was described earlier in the Results section, for all eight investigated clips, the active rectangle algorithm performs more closely to the manual measurement than the other two methods. This is due to the fact the AP-diameter is clinically defined as the largest vertical diameter inside the IVC. The active circle algorithm finds the largest circle inside the IVC and assumes that the diameter of this circle can efficiently model the AP-diameter. This is technically correct if the IVC is horizontally aligned. But based on the angle of the ultrasound prob, the IVC in the ultrasound clip can be rotated along the horizontal axis and this makes the results somewhat different from the clinically measured AP-diameter.

In five out of the eight cases, the active circle algorithm performed better than the active ellipse algorithm. This is mainly due to the fact that a circle has less degree of freedom than an ellipse and therefore, circle evolution can be performed more accurate than ellipse evolution. Furthermore, from Fig. 4.5, one can see that in most cases, the IVC does not appear to have an elliptical shape making the ellipse fitting process inaccurate.

4.5.2 Complexity Comparison

In this section, we analyze the computational complexity of the proposed algorithms in terms of the number of floating points operations (flops) required to estimate the AP-diameter for each frame. Assume N_i as the maximum number of iterations required to reach convergence, K is the number of contour points, and A_{max} is the maximum number of pixels inside the fitted shape. The maximum required flops per frame for the active circle algorithm is $N_{flops}^{cir} \approx (2A_{max} + 3K)N_i$. From equations (4.4), (4.13), (4.14), (4.15), and (4.16), one can see that the maximum required flops per frame for active ellipse and rectangle algorithms are $N_{flops}^{ell} \approx (2A_{max} + 5K)N_i$ and $N_{flops}^{rec} \approx (2A_{max} + 2K)N_i$, respectively. Note that the rectangular model converges much more quickly than the circular and elliptical models as the active circle and ellipse algorithms need up to $N_i = 5000$ iterations to reach convergence, while the active rectangle algorithm converges in no more than $N_i = 200$ iterations. with an average i7-3770 Intel processor, estimation of AP-diameter from each frame using active circle, ellipse, and rectangle algorithms requires about 1, 8.5, and and 0.1 millisecond, respectively

4.6 Conclusions

In this Chapter, two novel algorithms based on elliptical and rectangular models were proposed for semi-automatic estimation of AP-diameter of the IVC in ultrasound videos. The proposed algorithms were compared with the active circle algorithm and it was shown that although IVC usually has an elliptical CSA, both circular and rectangular models provide a more accurate AP-diameter measurement, while the rectangular model outperforms the other two models. This is due that fact that the AP-diameter is clinically measured as the maximum vertical diameter of the IVC which can be modeled better as the vertical side of a rectangle rather than the diameter of a circle or even the largest vertical axis of an ellipse.

References

[1] Vassilios Smyrniotis, Georgia Kostopanagiotou, Kassiani Theodoraki, Dimitrios Tsantoulas, and John C Contis. The role of central venous pressure and type of vascular control in blood loss during major liver resections. *The American journal of surgery*, 187(3):398–402, 2004.

[2] Emanuel Rivers, Bryant Nguyen, Suzanne Havstad, Julie Ressler, Alexandria Muzzin, Bernhard Knoblich, Edward Peterson, and Michael Tomlanovich. Early goal-directed therapy in the treatment of severe sepsis and septic shock. *New England Journal of Medicine*, 345(19):1368–1377, 2001.

[3] Mohammad Ikhsan, Kok Kiong Tan, Andi Sudjana Putra, Tsong Huey Sophia Chew, and Chee Fai Kong. Automatic identification of blood vessel cross-section for central venous catheter placement using a cascading classifier. In *Engineering in Medicine and Biology Society (EMBC), 2017 39th Annual International Conference of the IEEE*, pages 1489–1492. IEEE, 2017.

[4] Cyprian Ogum, Seetharaman Hariharan, and Deryk Chen. Non-invasive central venous pressure estimation by ultrasound-guided internal jugular vein cross-sectional area measurement. *Biomedical Physics & Engineering Express*, 2(2): 025004, 2016.

[5] Cyril Charron, Vincent Caille, Francois Jardin, and Antoine Vieillard-Baron. Echocardiographic measurement of fluid responsiveness. *Current opinion in critical care*, 12(3):249–254, 2006.

[6] Lakshmi Durairaj and Gregory A Schmidt. Fluid therapy in resuscitated sepsis: less is more. *Chest Journal*, 133(1):252–263, 2008.

[7] Christophe Barbier, Yann Loubières, Christophe Schmit, Jan Hayon, Jean-Louis Ricôme, François Jardin, and Antoine Vieillard-Baron. Respiratory changes in inferior vena cava diameter are helpful in predicting fluid responsiveness in ventilated septic patients. *Intensive care medicine*, 30(9):1740–1746, 2004.

[8] Weiming Wang, Lei Zhu, Jing Qin, Yim-Pan Chui, Bing Nan Li, and Pheng-Ann Heng. Multiscale geodesic active contours for ultrasound image segmentation using speckle reducing anisotropic diffusion. *Optics and Lasers in Engineering*, 54:105–116, 2014.

[9] Suresh Sudha, GR Suresh, and R Sukanesh. Speckle noise reduction in ultrasound images by wavelet thresholding based on weighted variance. *International journal of computer theory and engineering*, 1(1):7, 2009.

[10] Robert F Wagner, Stephen W Smith, John M Sandrik, and Hector Lopez. Statistics of speckle in ultrasound b-scans. *IEEE transactions on sonics and ultrasonics*, 30(3):156–163, 1983.

[11] José C Seabra, Francesco Ciompi, Oriol Pujol, Josepa Mauri, Petia Radeva, and Joao Sanches. Rayleigh mixture model for plaque characterization in intravascular ultrasound. *IEEE Transactions on Biomedical Engineering*, 58(5):1314–1324, 2011.

[12] Marcelo Pereyra, Nicolas Dobigeon, Hadj Batatia, and Jean-Yves Tourneret. Segmentation of skin lesions in 2-d and 3-d ultrasound images using a spatially coherent generalized rayleigh mixture model. *IEEE transactions on medical imaging*, 31(8):1509–1520, 2012.

[13] TA Tuthill, RH Sperry, and KJ Parker. Deviations from rayleigh statistics in ultrasonic speckle. *Ultrasonic imaging*, 10(2):81–89, 1988.

[14] Ebrahim Karami, Mohamed S Shehata, and Andrew Smith. Tracking of the internal jugular vein in ultrasound images using optical flow. In *The 30th Annual IEEE Canadian Conference on Electrical and Computer Engineering (CCECE), Windsor, Canada*, pages 1–4. IEEE, 2017.

[15] Ebrahim Karami, Mohamed Shehata, and Andrew Smith. Ultrasound image segmentation techniques for tracking and measurement of the internal jugular vein. In *The 24th Annual Newfoundland Electrical and Computer Engineering Conference (NECEC), St. John's, Canada*, 2015.

[16] E Karami, M Shehata, P McGuire, and A Smith. A semi-automated technique for internal jugular vein segmentation in ultrasound images using active contours. In *2016 IEEE-EMBS International Conference on Biomedical and Health Informatics (BHI)*, pages 184–187. IEEE, 2016.

[17] Bo Liu, HD Cheng, Jianhua Huang, Jiawei Tian, Xianglong Tang, and Jiafeng Liu. Probability density difference-based active contour for ultrasound image segmentation. *Pattern Recognition*, 43(6):2028–2042, 2010.

[18] Mohammad Talebi, Ahamd Ayatollahi, and Ali Kermani. Medical ultrasound image segmentation using genetic active contour. *Journal of Biomedical Science and Engineering*, 4(02):105, 2011.

[19] J Alison Noble. Ultrasound image segmentation and tissue characterization. *Proceedings of the Institution of Mechanical Engineers, Part H: Journal of Engineering in Medicine*, 224(2):307–316, 2010.

[20] Lei Ma, Hidemichi Kiyomatsu, Keiichi Nakagawa, Junchen Wang, Etsuko Kobayashi, and Ichiro Sakuma. Accurate vessel segmentation in ultrasound im-

ages using a local-phase-based snake. *Biomedical Signal Processing and Control*, 43:236–243, 2018.

[21] Peter J Yim and David J Foran. Volumetry of hepatic metastases in computed tomography using the watershed and active contour algorithms. In *Computer-Based Medical Systems, 2003. Proceedings. 16th IEEE Symposium*, pages 329–335. IEEE, 2003.

[22] Sahirzeeshan Ali and Anant Madabhushi. An integrated region-, boundary-, shape-based active contour for multiple object overlap resolution in histological imagery. *IEEE transactions on medical imaging*, 31(7):1448–1460, 2012.

[23] Kensuke Nakamura, Makoto Tomida, Takehiro Ando, Kon Sen, Ryota Inokuchi, Etsuko Kobayashi, Susumu Nakajima, Ichiro Sakuma, and Naoki Yahagi. Cardiac variation of inferior vena cava: new concept in the evaluation of intravascular blood volume. *Journal of Medical Ultrasonics*, 40(3):205–209, 2013.

[24] Maximilian Baust et al. *Polar Active Contours for Medical Applications*. PhD thesis, Technische Universität München, 2012.

[25] E Karami, M Shehata, and A Smith. Segmentation and tracking of inferior vena cava in ultrasound images using a novel polar active contour algorithm. In *5th IEEE Global Conference on Signal and Information Processing, GlobalSIP2017*, pages 1–5. IEEE, 2017.

[26] Ebrahim Karami, Mohamed S Shehata, and Andrew Smith. Adaptive polar active contour for segmentation and tracking in ultrasound videos. *IEEE Transactions on Circuits and Systems for Video Technology*, 2018. doi: 10.1109/TCSVT.2018.2818072.

[27] Ebrahim Karami, Mohamed Shehata, and Andrew Smith. Estimation and tracking of ap-diameter of the inferior vena cava in ultrasound images using a novel active circle algorithm. *Computers in Biology and Medicine*, 98:16–25, 2018.

[28] David J Blehar, Dana Resop, Benjamin Chin, Matthew Dayno, and Romolo Gaspari. Inferior vena cava displacement during respirophasic ultrasound imaging. *Critical ultrasound journal*, 4(1):18, 2012.

[29] Julian Guerrero, Septimiu E Salcudean, James A McEwen, Bassam A Masri, and Savvakis Nicolaou. Real-time vessel segmentation and tracking for ultrasound imaging applications. *IEEE transactions on medical imaging*, 26(8):1079–1090, 2007.

Chapter 5

Segmentation and Tracking of the IJV

Detection of relative changes in circulating blood volume is important to guide resuscitation and manage a variety of medical conditions including sepsis, trauma, dialysis and congestive heart failure. Recent studies have shown that estimates of circulating blood volume can be obtained from the cross-sectional area (CSA) of the internal jugular vein (IJV) from ultrasound images. However, accurate segmentation and tracking of the IJV in ultrasound imaging is a challenging task and is significantly influenced by a number of parameters such as the image quality, shape, and temporal variation. In this paper, we propose a novel adaptive polar active contour (Ad-PAC) algorithm for the segmentation and tracking of the IJV in ultrasound videos. In the proposed algorithm, the parameters of the Ad-PAC algorithm are adapted based on the results of segmentation in previous frames. The Ad-PAC algorithm is applied to 65 ultrasound videos captured from 13 healthy subjects, with each video containing 450 frames. The results show that spatial and temporal adaptation of the energy functional significantly improves segmentation performance when compared to current state-of-the-art active contour algorithms.

5.1 Introduction

Determination of relative changes in circulating blood volume is important for a variety of acute and chronic medical conditions including hemorrhage from trauma, septic shock, dialysis and volume overload pertaining to congestive heart failure [1, 2, 3, 4, 5]. The estimation of absolute blood volume, while ideal, remains a significant challenge [6]. Recent studies suggest that non-invasive measures such as transverse ultrasound (cross-section area, CSA) of the internal jugular vein (IJV) can be used to detect and monitor relative changes in blood volume [7, 8]. As shown in Fig 5.1, the CSA of the IJV is dynamic with spatial and temporal variations that can correlate with relative changes in volume status. Short-term variability reflects a variety of factors including blood volume, proximity to the carotid artery, cardiac contractility, respiratory effort and local anatomy. Changes in parameters over the long-term can reflect relative changes in blood volume. Demonstration of short- and long-term CSA variability of a healthy patient sitting at different angles of inclination to simulate relative changes in circulating blood volume is shown in Fig. 5.2. Accurate segmentation and tracking of the rapidly changing IJV is fundamental to the use of ultrasound to estimate relative changes in blood volume.

Portable ultrasound, the technology typically used to image the IJV in the acute care setting, does have its limitations. Ultrasound videos are generated at the point of care by clinicians with a broad range of skills which can result in significant variation in image quality. Furthermore, manual segmentation of IJV is a time-consuming task and inappropriate for real-time blood-volume monitoring applications.

Fully automatic segmentation algorithms are an ideal objective; however, they tend to

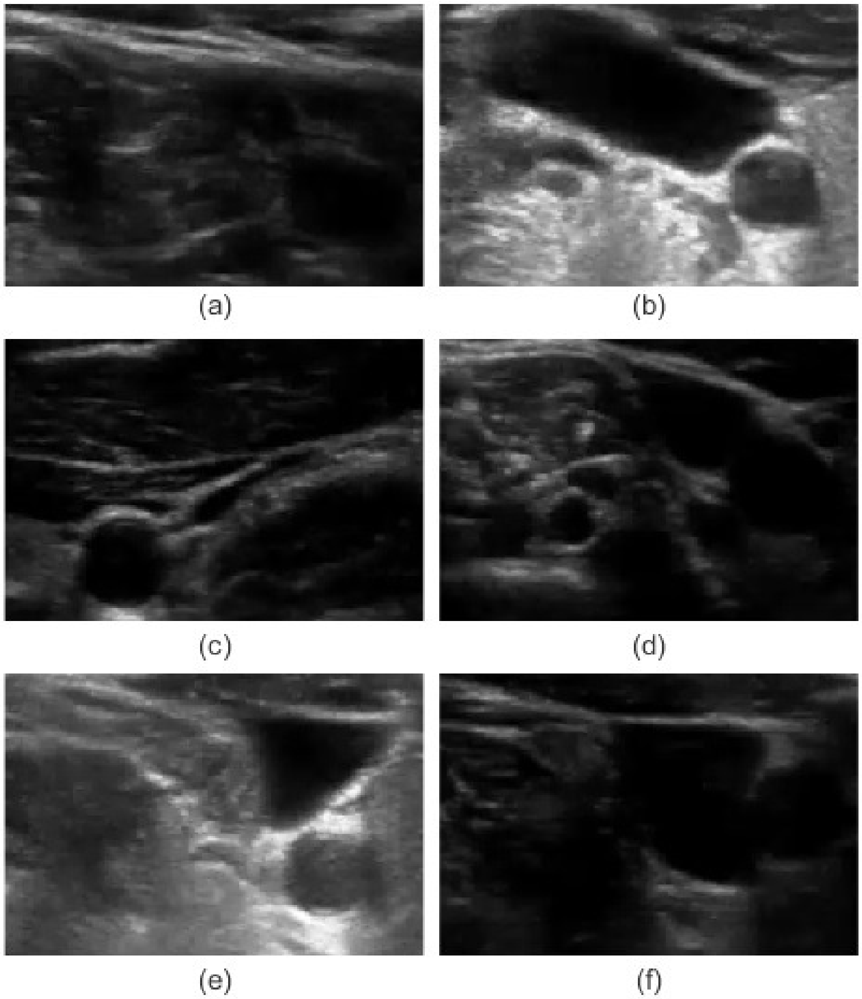

Figure 5.1: Sample images for IJV images with (a) low brightness, (b) high brightness, (c) fully collapsed, (d) partially missing contour (broken edge), (e) sharp contour (triangular) shape, and (f) non-convex contour shape.

require prior information about the images [9, 10, 11]. More recently, semi-automated segmentation algorithms requiring operator input have become popular in medical image processing [12, 13, 14, 15]. For example, combinatorial graph-cut based algorithms perform the segmentation task by minimizing an energy functional to find the minimal energy paths through the vertices that are manually selected by an operator [16, 17, 18]. Unfortunately, graph-cut algorithms suffer from high computational complexity, making them inefficient for real-time frame-by-frame segmentation, and

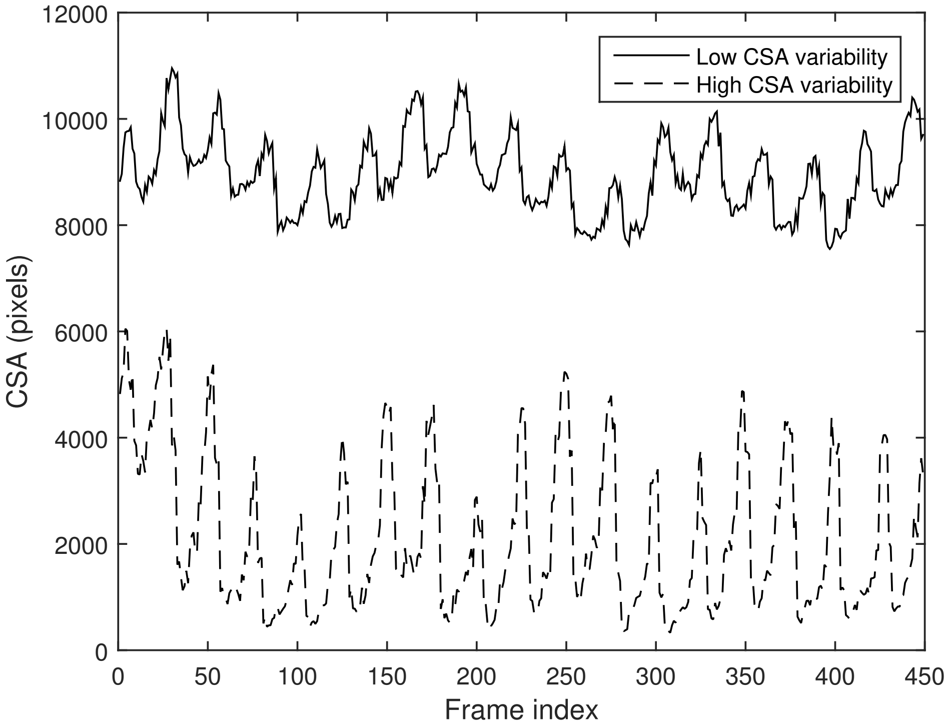

Figure 5.2: Temporal variations of IJV csa obtained from manual segmentation of two IJV videos with different CSA variability.

their results are sensitive to variations in image quality - a significant problem in ultrasound imaging.

Similar to graph-cut algorithms, active contours (ACs) segment images via minimization of an energy functional; however, their energy functional is more flexible than graph-cut based algorithms. This is demonstrated in their ability to adapt to complex shapes and track temporal deformations, making them suitable for real-time monitoring applications in medicine. An additional advantage is that the minimization is performed over a continuous surface, improving the computational complexity over graph-cut based techniques [19, 20, 21, 22, 23]. Unfortunately, these algorithms suffer from the fact that their performance is highly sensitive to the parameters of the energy functional and the initial contour, resulting in a limited ability to track topological changes. This limitation was addressed in the geometric deformable AC models based on curve or surface evolution [24, 25, 26]. In these models, the evolution is independent of the parameter selection and topological variations, which makes them more suitable for object tracking; however, they are still unable to detect shape split or merge due to the low quality of ultrasound images.

In general, the performance of AC algorithms also depends on the initial segmentation, and therefore, can be combined with other segmentation algorithms in a coarse-to-fine strategy. The coarse initial segmentation, obtained from another algorithm, provides a rough segmentation which is subsequently refined with an AC algorithm [27, 28]. In [29], the combination of speckle tracking [30] and AC was proposed for the segmentation and tracking of the IJV in which the coarse segmentation obtained from speckle tracking was smoothed with an AC. Unfortunately, speckle tracking fails when the IJV undergoes fast variations, unless the ultrasound machine has a sufficiently high frame rate. This problem was addressed by cascading region growing [31] and AC (RGAC) [32]. Unfortunately, all of these methods continue to fail when the image quality is poor or when a part of the vessel wall is obscured by artifact.

In the case of broken edges, active contours fail to resolve the contours of intersecting objects resulting in leakage. An active shape model (ASM) using a statistical shape model can be used to address the above mentioned problem [33, 34]. Unfortunately, as per Fig. 5.1, the IJV assumes many different shapes and therefore, ASM is not applicable for the IJV segmentation. Other common approaches, such as Kalman filers, have been proposed for real-time vessel tracking in ultrasound imagery; however, similar to ASM, they require the geometry of the vessel [35].

Segmentation can be viewed and solved as a spatio-temporal three dimensional (3D) segmentation problem with the time (frame index) defined as the 3rd dimension. 3D segmentation algorithms work on frame-by-frame basis using the similarity between regions [36, 37, 38, 39] or by attempting to minimize a 3D AC model [40, 41, 42, 43, 44]. The former methods again require imaging machines with high frame rates so that deformation from one frame to the next one is insignificant. The latter algorithms suffer from (1) significant computational complexity, (2) lower accuracy associated with minimization of a 3D energy functional which involves more parameters, and (3) the entire video prior to initiation of segmentation eliminating the possibility of real-time monitoring.

Polar representation of the contour is a useful technique in a variety of medical image processing applications, particularly vessel segmentation, in which the shape of the object is generally convex [45, 46, 47, 48]. Polar contours sample the object boundary at certain angles, reducing the degrees of freedom for each contour point to one. In other words, the contour is evolved only radially, enabling the energy functional to be minimized faster and efficiently than conventional ACs. Several examples include [45] in which polar edge detection is combined with AC for segmentation of tongue images; [49] incorporated a polar active contour algorithm based on a classic energy functional definition for segmentation of intra-vascular ultrasound images; [46] used a polar active contour defined with the external force derived from an energy term based on the area inside the contour; and [50], a variational polar active contour was proposed to inherit the robustness to local minima from Sobolev active contours. Unfortunately, all above mentioned polar AC algorithms are sensitive to image quality and object shape, with each working for a specific subset of image qualities and shapes. These algorithms fail to accurately segment clips across this spectrum, hence the need for an adaptive AC algorithm that accounts for these large variations.

In this paper, a novel adaptive polar AC algorithm (Ad-PAC) is proposed for semi-automatic segmentation and tracking of the IJV videos. This algorithm involves the initial frame being manually segmented by an operator and subsequently serving as the reference for the initial energy functional parameters selection. The parameters are then adapted from one frame to the next based on the segmentation results of previous frames. Section II introduces two related state-of-the-art polar AC algorithms; Section III describes the proposed algorithm; Section IV presents the results with comparisons to manual segmentation, traditional AC algorithms, and the two polar AC algorithms of Section II; and the conclusions are presented in Section V.

5.2 Related Work

Polar AC Algorithms

Polar representation of the contours reduce the degrees of freedom for each contour point such that the contour can only evolve radially. Each polar contour is sampled at certain angles, as shown in Fig. 5.3 as a contour with $N = 8$ points. In general,

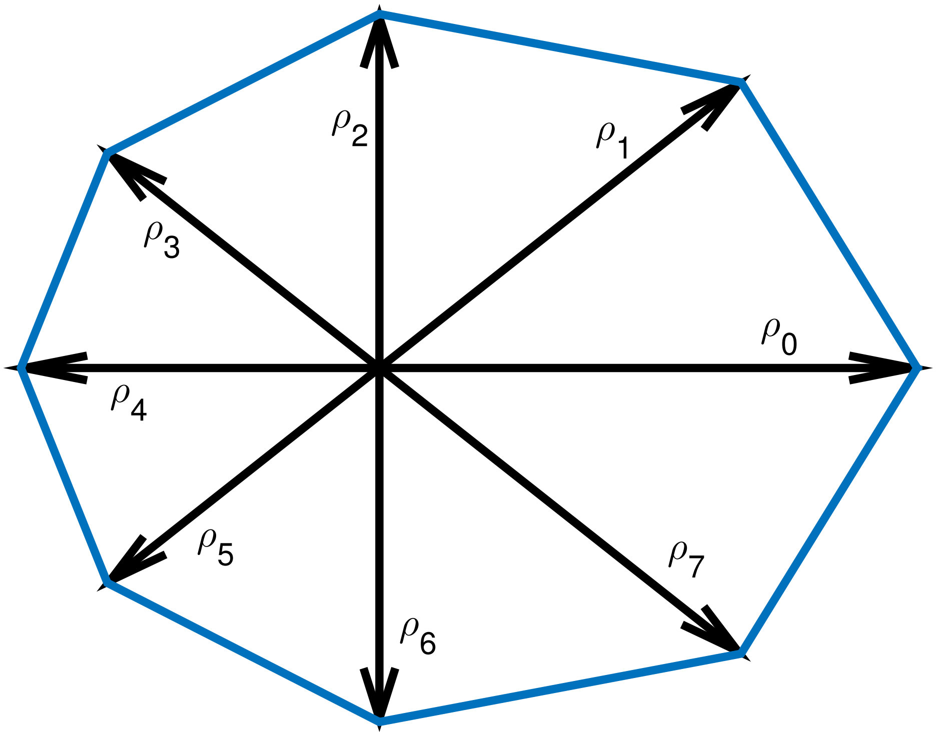

Figure 5.3: An example of polar contour with eight contour points.

polar AC algorithms minimize the following energy functional:

$$E_t = E_{int} + E_{ext}, \tag{5.1}$$

where E_{int} is the internal energy of the contour including forces from the contour shape parameters such as curvature (E_{curv}) and continuity (E_{cont}) defined as

$$E_{int} = \alpha E_{curv} + \beta E_{cont}, \tag{5.2}$$

where α, β are positive real constants. In [51], the curvature and continuity energies at angle θ are defined as

$$E_{curv,\theta} = (r_\theta - 2r_{\theta+1} + r_{\theta+2})^2, \tag{5.3}$$

$$E_{cont,\theta} = (r_\theta - r_{\theta+1})^2, \tag{5.4}$$

where r_θ is the radial distance at angle θ. Furthermore, according to [51], $E_{ext,\theta}$ is the external Hibernian energy at angle θ and defined as

$$E_{ext,\theta} = \gamma \left(1 - \frac{|\hat{f}(r_\theta)|}{max(|\hat{f}(r_\theta)|)} \right), \tag{5.5}$$

where γ is a positive real constant and $\hat{f}(r(\theta))$ is the Hilbert transform of $f(r(\theta))$. To overcome the problem of having shape-dependent constants, variational polar AC models have been proposed in the past[47, 50]. In these models, the energy functional has been defined as [50]:

$$E(c) = \int_{int(c)} f dx + \alpha \int_0^L g ds, \tag{5.6}$$

where $int(c)$ in the first integral that denotes the area which is bounded by the contour c, L is the length of c, f and g indicate the intensity and gradient functions, respectively, and α is the weight given to boundary information. The $\mathbb{L}^2$-gradient flow of $E(c)$ is calculated as [50]:

$$\nabla_{\mathbb{L}^2} E(c) = Lf\mathbf{n} + \alpha L(\nabla g \cdot \mathbf{n} - g\kappa)\mathbf{n}, \tag{5.7}$$

where $\mathbf{n}$ denotes the normal of the contour c and κ represents its curvature.

5.3 The Proposed Algorithm: Adaptive Polar AC (Ad-PAC)

The proposed algorithm (Ad-PAC) can be categorized as a polar 2D AC where the parameters of the energy functional are dynamically and automatically changed according to image quality as well as spatial and temporal variations of the object. Ad-PAC performs the segmentation task on a frame by frame basis creating the possibility for real-time applications. The novelties include:

- Modified energy functional: Ad-PAC enables researchers to incorporate many features followed by subsequent removal of weaker features depending on the application. An example of this is the continuity energy functional described in Section III-A - a weak feature for IJV segmentation which was subsequently removed. In this Chapter, we use six energy terms and derive their gradients in polar coordinates. Furthermore, we modified the energy terms proposed in existing polar ACs. For instance, from (5.9), one can see that the curvature energy proposed in [51] is not applicable, as in the case of a circular contour because it will result an energy term equal to zero which obviously cannot be correct and does not provide accurate results.

- Automatic adaptation of the energy functional: Ad-PAC automatically adapts the parameters based on the spatial and temporal features of the object as follows:

  1. Spatial parameter adaptation: The parameters of the energy functional are selected such that each energy term is optimized and adapted based on local features of objects such as shape and intensity. This makes the proposed algorithm more robust to image artifacts such as shadowing.

  2. Temporal parameter adaptation: In the proposed algorithm, the parame-

ters of the energy functional are adapted to temporal variations of the object, such as variations in shape, intensity, and the object area, on a per-frame basis. In conventional ACs, to achieve the best performance, parameters must be optimized for individual frames, a task requiring significant operator intervention. Outside of initialization, Ad-PAC automatically calculates optimized parameters drastically reducing the need for human intervention.

In the following subsections, we discuss these novelties in detail.

5.3.1 The Energy Functional

In the proposed algorithm, we define the energy functional as

$$\begin{aligned} E = \alpha E_{curv} + \beta E_{cont} + \gamma E_{edge} \\ + \kappa E_{var} + \zeta E_{intensity} + \nu E_{contr}, \end{aligned} \tag{5.8}$$

where α, β, γ, κ, ζ, and ν are real positive numbers, and E_{curv}, E_{cont}, E_{edge}, E_{var}, $E_{intensity}$, and E_{contr} are, respectively, the energy functional corresponding to the information in the object curvature, continuity, boundary, variability of the intensity in and out of the contour, the intensity on the object contour, and contraction energy. E_{curv} is the energy term used to control the contour curvature. The curvature energy proposed in [51] does not provide the correct result as it takes its minimum value for a circle, where $r_\theta =$ constant, i.e., it cannot segment the boundaries with less curvature than a circle (e.g., a straight line). In this Chapter, we extend the curvature energy defined in Cartesian coordinates, which is applicable to contours with any amount of curvature, to polar coordinates as:

$$E_{curv} = \sum_{n=0}^{N-1} |p_{n+1} - 2p_n + p_{n-1}|^2. \tag{5.9}$$

where N is the number of contour points, and p_n is the nth point vector defined as

$$[x_c + \rho_n \cos(n\phi_0), y_c + \rho_n \sin(n\phi_0)]\,, \tag{5.10}$$

with x_c and y_c being the coordinates of the center of the object in previous frame, respectively, $\phi_0 = \frac{2\pi}{N}$.

E_{cont} is the energy term used to control the distance between contour points and is defined as

$$E_{cont} = \sum_{n=0}^{N-1} |p_{n+1} - p_n|^2. \tag{5.11}$$

This definition is also similar to the continuity energy term used in Cartesian ACs and is different from the simple continuity energy term used in [51].

E_{edge} represents the edge energy in the object boundary though this term has limited value in scenarios with indistinct edges as is often the case in ultrasound imaging. This energy term is defined as

$$E_{edge} = -\sum_{n=0}^{N-1} |\nabla I\left(p_n\right)|^2, \tag{5.12}$$

where $|\nabla I|$ is the gradient magnitude of the image and $I\left(p_n\right)$ is the image intensity at the current frame.

E_{var} is similar to the variational energy term defined in either variational Cartesian or polar ACs and is defined as

$$E_{var} = -(u - v)^2, \tag{5.13}$$

where u and v are the mean intensities inside and outside of the contour, respectively.

$E_{intensity}$ is a proposed energy term which is defined to exploit the information in spatial illumination levels at the object boundary.

$$E_{intensity} = \sum_{n=0}^{N-1} \left| I\left(p_n\right) - I_0\left(p_n\right) \right|^2, \tag{5.14}$$

where $I_0\left(p_n\right)$ is the reference intensity of the contour obtained from the previous segmented frame.

E_{contr} is the energy term that controls the area of the object and is defined as

$$E_{contr} = -\sum_{n=0}^{N-1} \rho_n, \tag{5.15}$$

5.3.2 Local Parameterization of the Energy Functional

5.3.2.1 Overview

A major shortcoming in existing AC algorithms is that they define similar energy terms for all contour points, despite the fact that intensity and shape vary across the region of interest. To overcome this problem, the proposed algorithm weights the energy terms locally. For example, if part of the IJV contour is obscured by shadow then the algorithm assigns smaller weights to the external energy of the points in the shadowed region such that increased emphasis is on the internal energy terms. Similarly, if a part of the contour has a sharp curvature, the algorithm gives a smaller weight to the curvature energy term for points in areas with sharp edges. These small, non-zero weights enable the contour points to have larger curvatures while still contributing to the total energy. Furthermore, regional variations in intensity are incorporated by subdividing the region of interest (ROI) into multiple sectors with each sector containing one contour point and values of u and v calculated locally as shown in Fig. (5.4). After splitting the contour into N sectors, the energy functional

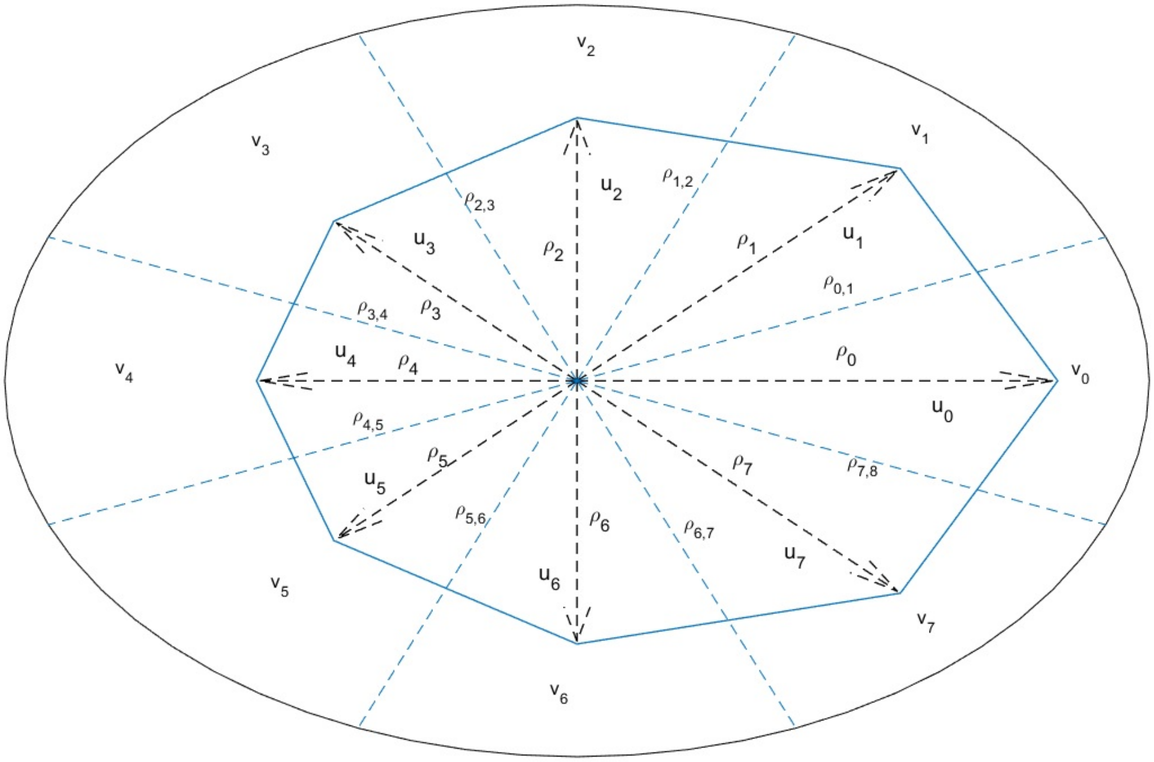

Figure 5.4: Adaptive polar structure.

is modified by giving spatial weights to equations (5.9-5.14) as:

$$E_{curv} = \sum_{n=0}^{N-1} \alpha_n |p_{n+1} - 2p_n + p_{n+1}|^2, \tag{5.16}$$

$$E_{cont} = \sum_{n=0}^{N-1} \beta_n |p_{n+1} - p_n|^2, \tag{5.17}$$

$$E_{edge} = -\sum_{n=0}^{N-1} \gamma_n |\nabla I\left(p_n\right)|^2, \tag{5.18}$$

$$E_{var} = -\sum_{n=0}^{N-1} \kappa_n (u_n - v_n)^2, \tag{5.19}$$

$$E_{intensity} = -\sum_{n=0}^{N-1} \zeta_n |I\left(p_n\right) - I_0\left(p_n\right)|^2, \tag{5.20}$$

where α_n, β_n, γ_n, κ_n, and ζ_n are the weights given to the energy terms of the nth region. Note that E_{contr} is the only remaining energy term which is not spatially adapted.

5.3.2.2 Energy Functionals in Polar Coordinates

Polar representation is used to derive the energy functional in the following sections.

The curvature energy: By substitution of (5.10) in (5.16), the curvature energy functional is rewritten as

$$E_{curv} = \sum_{n=0}^{N-1} \alpha_n [4\rho_n^2 + \rho_{n-1}^2 + \rho_{n+1}^2 - 4\rho_n(\rho_{n-1} + \rho_{n+1}) \\ \times \cos(\phi_0) + 2\rho_{n-1}\rho_{n+1}\cos(2\phi_0)], \tag{5.21}$$

and its gradient with respect to $\boldsymbol{\rho}$ is obtained as

$$\frac{\partial E_{curv}}{\partial \boldsymbol{\rho}} = \boldsymbol{A_c \rho}, \tag{5.22}$$

where $\mathbf{A}_c$ is an $N \times N$ penta-diagonal matrix with its elements defined as

$$a_c(i,j) = \\ \begin{cases} 2\alpha_{i-1}\cos(2\phi_0), & \text{if} \quad mod(i-j,N) = 2, \\ -4(\alpha_{i-1} + \alpha_i)\cos(\phi_0), & \text{if} \quad mod(i-j,N) = 1, \\ 2(\alpha_{i-1} + 4\alpha_n + \alpha_{n+1}), & \text{if} \quad i = j, \\ -4(\alpha_i + \alpha_{i+1}\cos(\phi_0), & \text{if} \quad mod(j-i,N) = 1, \\ 2\alpha_i\cos(2\phi_0), & \text{if} \quad mod(j-i,N) = 2, \\ 0, & \text{otherwise.} \end{cases} \tag{5.23}$$

where $i, j = 0, 1, ..., N-1$ are the indices of the matrix.

The continuity energy: Similarly, by substitution of (5.10) in (5.17), the continuity energy functional is rewritten as

$$E_{cont} = \sum_{n=0}^{N} \left(\rho_n^2 - 2\rho_n \rho_{n+1} \cos(\phi_0) + \rho_{n+1}^2 \right), \tag{5.24}$$

and its gradient with respect to $\boldsymbol{\rho}$ is computed as

$$\frac{\partial E_{cont}}{\partial \boldsymbol{\rho}} = \boldsymbol{B_c \rho}, \tag{5.25}$$

where $\mathbf{B}_c$ is an $N \times N$ tridiagonal matrix with its elements defined as

$$b_c(i,j) = \tag{5.26}$$

$$\begin{cases} -2\beta_{i-1}\cos(\phi_0), & \text{if} \quad mod(i-j,N) = 1, \\ 2(\beta_i + \beta_{i-1}), & \text{if} \quad i = j, \\ -2\beta_i \cos(\phi_0), & \text{if} \quad mod(j-i,N) = 1, \\ 0, & \text{otherwise.} \end{cases}$$

The edge energy: From (5.18), the gradient of the edge energy with respect to $\boldsymbol{\rho}$ is an $N \times 1$ vector $\boldsymbol{G} = [g_0, \quad g_1, \quad ..., \quad g_{N-1}]^T$ where

$$g_i = \tag{5.27}$$

$$-\gamma_i \left[\frac{\partial |\nabla I\left(p_i\right)|^2}{\partial x} \cos(i\phi_0) + \frac{\partial |\nabla I\left(p_i\right)|^2}{\partial y} \sin(i\phi_0) \right].$$

The variational energy: In (5.19), u_n and v_n can be computed as,

$$u_n = \frac{S_n}{A_n}, \tag{5.28}$$

$$v_n = \frac{S_n^{(c)}}{A_n^{(c)}}, \tag{5.29}$$

where S_n and $S_n^{(c)}$ are total intensities inside C_n and $C_n^{(c)}$, respectively, and are obtained as

$$S_n = \int_{C_n} I dA, \tag{5.30}$$

$$S_n^{(c)} = \int_{C_n^{(c)}} I dA, \tag{5.31}$$

with C_n and $C_n^{(c)}$ as the areas inside and outside the nth sector, respectively, and A_n and $A_n^{(c)}$ are their corresponding areas which can be computed as follow,

$$A_n \approx \frac{1}{4} \sin\left(\frac{\phi_0}{2}\right) \rho_n \left(\rho_{n+1} + 2\rho_n + \rho_{n-1}\right), \tag{5.32}$$

$$A_n^{(c)} = \frac{1}{2}\phi_0 R^2 - A_n, \tag{5.33}$$

where R is the maximum radius of the search area. In this Chapter, R is set to be 50 percent larger than the maximum contour radius, ρ_n, estimated in previous frame. From (5.28) and (5.29), the gradient of u_n and v_n with respect to ρ_i is computed as,

$$\frac{\partial u_n}{\partial \rho_i} = \frac{(I_n - u_n)}{A_n} \frac{\partial A_n}{\partial \rho_i}, \tag{5.34}$$

$$\frac{\partial v_n}{\partial \rho_i} = -\frac{(I_n - v_n)}{A_n} \frac{\partial A_n}{\partial \rho_i}, \tag{5.35}$$

From (5.13), (5.34), (5.35), (5.32), and (5.33), one can find the gradient of $E_{intensity}$ with respect to ρ_n as

$$\frac{\partial E_{var}}{\partial \rho} = \boldsymbol{U\rho}, \tag{5.36}$$

where $\boldsymbol{U}$ is an $N \times N$ tri-diagonal matrix defined as follows,

$$U(i,j) = \begin{cases} \iota(i) + \iota(i-1) & \text{if} \quad mod(i-j,N) = 1, \\ 4\iota(i) & \text{if} \quad i = j, \\ \iota(i) + \iota(i+1) & \text{if} \quad mod(j-1,N) = 1, \\ 0, & \text{otherwise}, \end{cases} \tag{5.37}$$

with $\iota(i)$ defined as

$$\begin{aligned} \iota(i) = & \\ & -\frac{1}{2}\kappa_i \sin(\frac{\phi_0}{2})(u_i - v_i)\left(\frac{I_i - u_i}{A_i} - \frac{I_i - v_i}{\frac{1}{2}\phi_0 R^2 - A_i}\right). \end{aligned} \tag{5.38}$$

The intensity energy: the gradient of the intensity energy with respect to $\boldsymbol{\rho}$ is an $N \times 1$ vector $\boldsymbol{\chi}$, in which its elements are defined as

$$\begin{aligned} \boldsymbol{\chi}_i = & \zeta_i \left(I\left(p_i\right) - I_0\left(p_i\right)\right) \\ & \times \left(\frac{\partial I\left(p_i\right)}{\partial x}\cos(i\phi_0) + \frac{\partial I\left(p_i\right)}{\partial y}\sin(i\phi_0)\right). \end{aligned} \tag{5.39}$$

In this Chapter, simple iterative gradient descent technique is used to minimize the defined energy functional, although due to single-dimensionality of the energy functional, more quickly techniques are also applicable [52]. From equations (5.22), (5.25), (5.27), (5.36), and (5.39) the gradient of the total energy functional is obtained as

$$\frac{\partial E_c}{\partial \boldsymbol{\rho}} = \left(\boldsymbol{\alpha A_c} + \boldsymbol{\beta B_c} + \boldsymbol{\kappa U}\right)\boldsymbol{\rho} + \boldsymbol{\gamma G} + \boldsymbol{\zeta \chi} + \nu \mathbf{1}_{\boldsymbol{N\times 1}}. \tag{5.40}$$

where $\mathbf{1}_{\boldsymbol{N\times 1}}$ is $N \times 1$ all-ones vector. Using (5.40), the energy functional can be iteratively minimized as

$$\begin{aligned}\boldsymbol{\rho}_{(i)} =& \boldsymbol{\rho}_{(i-1)} - \mu_1(\mathbf{1} + \mu_2\boldsymbol{\rho}_{(i-1)}) \\ & \odot \left[(\boldsymbol{\alpha}\boldsymbol{A_c} + \boldsymbol{\beta}\boldsymbol{B_c} + \boldsymbol{\kappa}\boldsymbol{U})\,\boldsymbol{\rho} + \boldsymbol{\gamma}\boldsymbol{G} + \boldsymbol{\zeta}\boldsymbol{\chi} + \nu\mathbf{1}_{\boldsymbol{N}\times\mathbf{1}}\right],\end{aligned} \tag{5.41}$$

where $\boldsymbol{\rho}_{(i)}$ is the estimated $\boldsymbol{\rho}$ at kth iteration, $\odot$ is the Hadamard vector product, and μ_1 and μ_2 are two step size parameters that let the algorithm to approach more quickly to the equilibrium when the contour point is farther from the center point.

5.3.3 Parameter Adaptation

The parameters are adapted to the shape and size of the object and to the local intensities around the contour points of previous frames.

Adaptation of the number of contour points N: The first parameter adapted is the number of contour points, N, whose optimal value depends on the object size. Adaptation of N is important due to large size variations in the contour. For example, when the contour shrinks, the elements of $\boldsymbol{\rho}_{(i)}$ become very small such that some terms can become negative during energy minimization using (5.41). On the contrary, when the contour expands, the distance between adjacent contour points increases resulting in an inaccurate rough contour. In this Chapter, we select the number of contour points such that the average spacing between contour points is a constant value Λ while later demonstrating the influence of Λ on the segmentation accuracy. After segmenting each frame, the perimeter of the contour (P) is computed and used to calculate the number of contour points using

$$N^k = \left\lceil \frac{\sum_{n=0}^{N^{k-1}-1} \left|p_{n+1}^{k-1} - p_n^{k-1}\right|}{\Lambda} \right\rceil, \tag{5.42}$$

where $\lceil x \rceil$ denotes the smallest integer greater than or equal to x, and superscript k denotes the frame index. After updating the number of contour points, the contour is re-sampled at angles

$$\phi_n = n\phi_0^k, \tag{5.43}$$

where $n = 0, 1, ..., N^k - 1$ and $\phi_0^k = \frac{2\pi}{N^k}$.

Parameter selection for the curvature energy: If the object boundary around a contour point is sharp, then the gradient of the curvature energy of that contour point is relaxed such that at the equilibrium (total energy minimized) it can approach a value with larger absolute value compared to the points on more smooth parts of the contour. Therefore, in the proposed algorithm, we select the parameters α_n^k of the kth frame, such that at the equilibrium condition for the reference frame (previous frame), all contour points have similar gradient of curvature as

$$\left| \frac{\partial E_{curv,k,k-1}}{\partial \rho_n^{k-1}} \right| = 1, \tag{5.44}$$

where $E_{curv,k,k-1}$ is defined as the curvature energy of the $(k-1)$th frame with the weights α_n^k and is computed by substituting $\alpha_n = \alpha_n^k$ and $\rho_n = \rho_n^{k-1}$ in (5.21). Using (5.22) and (5.23), (5.44) can be rewritten as

$$\left| \boldsymbol{A_c} \boldsymbol{\rho}^{k-1} \right| = \mathbf{1}_{\boldsymbol{N}\times\mathbf{1}}. \tag{5.45}$$

where the elements of $\boldsymbol{A_c}^k$ are calculated using equation (5.23) for the kth frame. Note that equation (5.45) is NP-hard, but we can find an approximate closed form solution as follows. The nth row of the matrix equation in (5.45) is

$$\begin{aligned}
&|2\alpha_{n-2}\rho_{n-2}^{k-1}\cos(2\phi_0) - 4(\alpha_{n-1}+\alpha_n)\rho_{n-1}^{k-1}\cos(\phi_0)\\
&+ 2(\alpha_{n-1}+4\alpha_n+\alpha_{n+1})\rho_n^{k-1} - 4(\alpha_n\\
&+ \alpha_{n+1})\rho_{n+1}^{k-1}\cos(\phi_0) + 2\alpha_{n+2}\rho_{n+2}^{k-1}\cos(2\phi_0)|\\
&= 1. \qquad (5.46)
\end{aligned}$$

By assuming that the local parameters α_n do not rapidly change, i.e., $\alpha_{n-2} \approx \alpha_{n-1} \approx \alpha_n \approx \alpha_{n+1} \approx \alpha_{n+2}$, (5.46) is simply as

$$\begin{aligned}
\alpha_n^k = \Big(\epsilon + \Big|&12\boldsymbol{\rho_n}^{k-1} - 8(\boldsymbol{\rho_{n-1}}^{k-1} + \boldsymbol{\rho_{n+1}}^{k-1})\cos(\phi_0^k)\\
&+2(\boldsymbol{\rho_{n_{-2}}}^{k-1} + \boldsymbol{\rho_{n_{+2}}}^{k-1})\cos(2\phi_0^k)\Big|\Big)^{-1}, \qquad (5.47)
\end{aligned}$$

where ϵ is a very small number to avoid zero at the denominator. Note that with this parameter selection, (5.44) is approximately satisfied.

Parameter selection for the continuity energy: Similarly, the weights of continuity energy are adapted using the segmentation result from the previous frame such that

$$\left|\frac{\partial E_{cont,k,k-1}}{\partial \rho_n^{k-1}}\right| = 1, \qquad (5.48)$$

where $E_{cont,k,k-1}$ is the continuity energy of the $(k-1)$th frame with the weights β_n^k and is computed by substituting $\beta_n = \beta_n^k$ and $\rho_n = \rho_n^{k-1}$ in (5.24). Using (5.25) and (5.26), (5.48) can be rewritten as

$$\left|\boldsymbol{B_c}^k \boldsymbol{\rho}^{k-1}\right| = \boldsymbol{1_{N\times 1}}, \qquad (5.49)$$

Similar to (5.45), (5.49) is NP-Hard but has an approximate solution as

$$\beta_n^k = \left(\epsilon + |4\boldsymbol{\rho_n}^{k-1} - 2(\boldsymbol{\rho_{n-1}}^{k-1} + \boldsymbol{\rho_{n+1}}^{k-1})\cos(\phi_0^k)|\right)^{-1}. \tag{5.50}$$

Parameter selection for the edge energy: Adaptation of the parameters γ_n in the edge energy functional (see eq. 5.12)) is crucial. Lack of adaptation would result in the edge energy forcing the AC to continue to expand in areas of broken edges or shadow resulting in leakage outside the actual object boundary. The weighting for the edge energy is selected such that

$$\left|\frac{\partial E_{edge,k,k-1}}{\partial \rho_n^{k-1}}\right| = 1, \tag{5.51}$$

where $E_{edge,k,k-1}$ is $|\nabla I_1(p_n)|^2$ of the $(k-1)$th frame. Consequently, the weights γ_n^k are obtained as

$$\begin{aligned}\gamma_n^k = \Bigg(\epsilon + \Bigg|&\frac{\partial|\nabla I_{k-1}\left(p_n^{k-1}\right)|^2}{\partial x}\cos(n\phi_0^k)\\ &+\frac{\partial|\nabla I_{k-1}\left(p_n^{k-1}\right)|^2}{\partial y}\sin(n\phi_0^k)\Bigg|\Bigg)^{-1}.\end{aligned} \tag{5.52}$$

Parameter selection for the variational energy: Similar to the previous energy terms, the weights κ_n in the variational energy functional (see equation (5.13)) are selected such that

$$\left|\frac{\partial E_{var,k,k-1}}{\partial \rho_n^{k-1}}\right| = 1, \tag{5.53}$$

where κ is a constant value and $E_{var,k,k-1}$ is the variational energy of the $(k-1)$th frame with the weights κ_n^k and is computed by substituting $\kappa_n = \kappa_n^k$ and $\rho_n = \rho_n^{k-1}$ in (5.13). Consequently, using (5.36), (5.37), and (5.53), the weights κ_n^k can be approximately obtained as

$$\begin{aligned}\kappa_n^k = \Big(\epsilon + \Big|\Big(\iota^{k-1}(n) + \iota(n-1)\Big)\,\rho_{n-1}^{k-1} + 4\iota^{k-1}(n)\rho_n^{k-1} \\ + \Big(\iota^{k-1}(n) + \iota^{k-1}(n+1)\Big)\,\rho_{n+1}^{k-1}\Big|\Big)^{-1}.\end{aligned} \tag{5.54}$$

Parameter selection for the intensity energy: The intensity energy and its gradient at the previous frame are both equal to zero (see eq. (5.14)) and hence, the weights cannot be based on the information from previous frame. In this Chapter, the weights ζ_n^k are heuristically set as

$$\zeta_n^k = \left|\left(I\left(p_n^{k-1}\right)\right)\right|^2, \tag{5.55}$$

From (5.55), one can see that in the case of broken edges, where the intensity is almost zero, the intensity energy is automatically set to zero which is a reasonable outcome. *Parameter Adaptation with Forgetting Factor*: Since the parameters of the AC are not expected to change rapidly, the parameters obtained from previous frames can always be used to improve segmentation accuracy and avoid misleading results due to the poor segmentation of any one individual frame. The forgetting factor, ξ, is defined as

$$\alpha_n^k = \xi\alpha_{n,0}^k + (1-\xi)\alpha_n^{k-1}, \tag{5.56}$$

$$\beta_n^k = \xi\beta_{n,0}^k + (1-\xi)\beta_n^{k-1}, \tag{5.57}$$

$$\gamma_n^k = \xi\gamma_{n,0}^k + (1-\xi)\gamma_n^{k-1}, \tag{5.58}$$

$$\kappa_n^k = \xi\kappa_{n,0}^k + (1-\xi)\kappa_n^{k-1}, \tag{5.59}$$

$$\zeta_n^k = \xi\zeta_{n,0}^k + (1-\xi)\zeta_n^{k-1}, \tag{5.60}$$

where $\alpha_{n,0}^k$, $\beta_{n,0}^k$, $\gamma_{n,0}^k$, and $\kappa_{n,0}^k$ are the value of the parameters obtained from (5.47), (5.50), (5.52), and (5.54), respectively. Note that since the first frame is segmented manually, its results are assumed to be accurate and therefore, the forgetting factor ξ is applied to weights obtained from the segmentation results of subsequent frames. Also note that, since it is assumed that at equilibrium, the overall gradient of energy is zero, then

$$\alpha + \beta \approx \gamma + \kappa. \tag{5.61}$$

5.4 Implementation of The Ad-PAC Algorithm

The Ad-PAC algorithm is initialized from a manually generated segmentation of the first frame. This manual segmentation is adjusted and smoothed using Ad-PAC (without parameter adaptation), reducing the error associated with initial manual segmentation. This makes the initial segmentation insensitive to small operator errors as large as 5 pixels. For larger operator errors, this smoothing process may converge the initial manual segmentation to a different local minima (such as the boundary of an adjacent object). Next, the number of contour points is updated using (5.42). Third, the centroid is calculated as

$$x_c^k = x_c^{k-1} + \frac{1}{N^k} \sum_{n=0}^{N^k-1} \rho_n^{k-1} \cos(\phi_n^k), \tag{5.62}$$

$$y_c^k = y_c^{k-1} + \frac{1}{N^k} \sum_{n=0}^{N^k-1} \rho_n^{k-1} \sin(\phi_n^k), \tag{5.63}$$

followed by the contour being re-sampled at angles obtained from (5.43) using a cubic spline interpolation algorithm[53]. Next, the weights of the energy functional are obtained using (5.47), (5.50), (5.52), (5.54), and (5.55). Then, the value of $\boldsymbol{\rho}^{(k)}$ is iteratively updated using (5.41), until the equilibrium stop condition is met. In this Chapter, the algorithm is assumed to be at equilibrium if $\max(\left|\boldsymbol{\rho}^{(k)} - \boldsymbol{\rho}^{(k-1)}\right|) < 10^{-4}$, where max(.) is element-wise maximum. Finally, the algorithm returns to the first step to repeat the procedure for the next frame. A summary of the Ad-PAC algorithm is shown in Table 1.

Table 1. Ad-PAC algorithm

Input: A video, $p_n^{(1)}$, with $n = 0, 1, ..., N-1$ as manual segmentation of the first frame, where N is the initial number of contour points, and parameters α, β, γ, κ, ζ, and Λ.
- Read one frame from the input video.
- Update the number of contour points using (5.42).
- Find the center of the contour and re-sample the contour at the angles $\phi_n = \frac{2n\pi}{N}$.
- Update the weights of the energy functional using (5.47), (5.50), (5.52), and (5.54), (5.55), (5.56), (5.57), (5.58), and (5.59), and (5.60).
- Update the value of $\boldsymbol{\rho}$ iteratively, using (5.41).
- Repeat the previous step until the algorithm reaches to the equilibrium condition. The equilibrium condition is defined as the condition when the maximum absolute value of change in $\boldsymbol{\rho}$ at the previous step is less than 10^{-4} pixels.
- Return to the first step for the next frame.

Computational complexity: The computational complexity of the Ad-PAC algorithm is estimated using the number of floating point operations (flops) [54]. From (5.22), (5.23), (5.25), (5.26), (5.27), (5.36), (5.37), (5.39) and (5.41), one can see that the total number of flops required for each iteration of the algorithm is $70N$. From (5.47), (5.50), (5.52), and (5.54), (5.55), (5.56), (5.57), (5.58), and (5.59), and (5.60), one can further see that the total number of flops required to parameter adaptation is $61N$ plus an additional $30N$ flops required for cubic re-sampling [55], and $10N + 2$ flops to update the center of the contour. Additionally, to compute the Sobel gradients of a 380 by 365 frame, $N_G = 832200$ flops are required. Consequently, assuming N_{iter} as the number of iterations required to minimize the energy functional, the total number of $N_{flops} \approx 70N_{iter}N + 101N + N_G + 2$ is required for segmentation of each frame with the Ad-PAC algorithm. Note that since parameter adaption is performed only once per frame, it does not significantly affect the processing time. Assuming $N_{iter} = 5000$, $N = 64$, and 25 percent extra processing power required for the software overhead, with an average Intel Core i750 the segmentation of each 380 by 365 frame requires only 3×10^{-3} sec, which makes the algorithm suiTable for real time segmentation and tracking purposes. Note that the running time can be significantly reduced by using more quickly minimization techniques such as the dynamic programming approach described in [52].

5.5 Results

The experimental data was collected from 13 healthy subjects and with head of the bed elevated at 0, 30, 45, 60, and 90 degrees to simulate relative changes in blood volume. The IJV was imaged in the transverse plane using a porTable ultrasound (M-Turbe, Sonosite-FujiFilm) with a linear-array probe (6-15 Mhz). Each video has a frame rate of 30 fps, scan depth of 4cm, and a duration of 15 seconds (450 frames/clip). The study protocol was reviewed and approved by the Health Research Ethics Authority. Ad-PAC performance was compared to expert manual segmentation, Ad-PAC without parameter adaptation, Ad-PAC without temporal adaptation, and two current state-of-the-art polar AC algorithms introduced in Section II [50, 51]. Additionally, it was also compared to region growing (RG) [31] and its combination with AC (RGAC) [32], Speckle tracking driven AC (STAC) [29], and two classic AC algorithms - Chan-Vese [56] and Geodesic [57]. Each of these algorithms implemented with MATLAB and their parameters optimized using a small subset of videos with variable image quality. For each video, the first frame was manually segmented by an operator with subsequent frames segmented automatically.

Initial efforts involved noise filtration using a variety of median and bilateral filters however no performance improvement was noted for any of the algorithms. This is mainly due to the fact that speckle noise includes useful information that can improve the performance of AC algorithms. Hence, pre-processing techniques were not employed throughout this research.

The average contour point spacing was defined to be 10 pixels for the Ad-PAC and the other four algorithms $N = 64$. Image intensities were normalized to between 0 and 1. The parameters of Ad-PAC algorithm were empirically set to be $\alpha = 1$, $\beta = 0$, $\gamma = 0.05$, $\kappa = 0.8$, $\zeta = 150$, $\nu = 0.0012$, $\mu_1 = 10^{-4}$, $\mu_2 = 1$, and $\epsilon = 10^{-4}$. After segmentation of each frame, the maximum range R was readjusted to be $1.5\rho_{max}$, where ρ_{max} was the largest element of $\boldsymbol{\rho}$ obtained from the previous frame.

5.5.1 Evaluation of Extraction

Before we define the validation metrics, we need to define the following terms:

True positive (TP): The number of pixels correctly segmented as foreground (manual segmentation overlapping with algorithm segmentation) is True Positive (TP) and defined as

$$TP = |\mathbb{A} \cap \mathbb{M}|, \tag{5.64}$$

where $\mathbb{A}$ and $\mathbb{M}$ are the set of pixels inside the contour obtained from the algorithms and manual segmentation, respectively, $|\mathbb{A} \cap \mathbb{M}|$ the intersection of the area between them, and $|.|$ denotes the cardinality of the set.

False positive (FP): False positive (FP) is the number of pixels that are falsely segmented as foreground and is represented as

$$FP = |\mathbb{A} \cap \mathbb{M}^c|, \tag{5.65}$$

where superscript ^{c} denotes set complement, i.e., set of the pixels outside the contour.

True negative (TN): True negative (TN) is the number of pixels correctly labeled as background and defined as

$$TN = |\mathbb{A}^c \cap \mathbb{M}^c|, \tag{5.66}$$

False negative (FN) is the number of pixels falsely detected as background and defined as

$$FN = |\mathbb{A}^c \cap \mathbb{M}|, \tag{5.67}$$

Using these terms, *Sensitivity* and *specificity* which are also known as true positive and false positive rates, respectively, are obtained as

$$Sensitivity = \frac{TP}{TP + FN}, \tag{5.68}$$

$$Specificity = \frac{FP}{FP + TN}. \tag{5.69}$$

The DICE factor (DF), also known as Sorensen, is the most common metric used to determine the correlation between algorithm and manual segmentation results [58]. The DICE coefficient, DF, is defined as:

$$DF = \frac{2|\mathbb{A} \cap \mathbb{M}|}{|\mathbb{A}| + |\mathbb{M}|}, \tag{5.70}$$

and can be obtained from the above metric as

$$DF = \frac{2TP}{2TP + FP + FN}. \tag{5.71}$$

5.5.2 Influence of Initial Parameter Selection on the Performance of Ad-PAC

This section demonstrates the robustness of the algorithm for each parameter along with the relative importance of each parameter on the overall performance. This enables the identification and potential removal of weak features from the energy functional in order to improve computational efficiency. For this study, the average DICE factor, sensitivity, and specificity of three different clips versus the initial parameters α, β, γ, κ, and ν are shown in Figs. 5.5-5.10. In the all of these figures, one can easily see that the specificity is always very close to one indicating a relatively small rate of FP.

The three test videos suggest setting α to one supports optimal segmentation as shown in Fig. 5.5. Large values of α result in excessive contour shrinking while small values reduce contour smoothness.

The parameter β demonstrates optimal performance near zero as per Fig. 5.6. This strongly suggests that the continuity energy term is a weak feature and hence, can be removed from the energy functional.

In Fig. 5.7, all three videos provide their best performance at a γ between 0.04 and 0.08, hence, γ is set at 0.06. In two of the three test videos, the edge energy does not significantly improve the segmentation performance as the curves appear flat around $\gamma = 0$ likely resulting from indistinct edges and consequently, providing limited information to improve segmentation results.

Fig. 5.8 highlights that different videos demonstrate considerable variance in sensitivities versus κ. Sensitivity was relatively sTable for κ ranging between 0.4 and 0.9, hence κ was set to 0.8.

For the parameter ζ, the best performance was established between 125 - 175 as shown in Fig. 5.9. Hence, ζ equal to 150 seems to be an appropriate selection.

Finally Fig. 5.10 shows that the best performance is obtained when ν is between 0.0009 and 0.0015 resulting in $\nu = .0012$ as an appropriate selection.

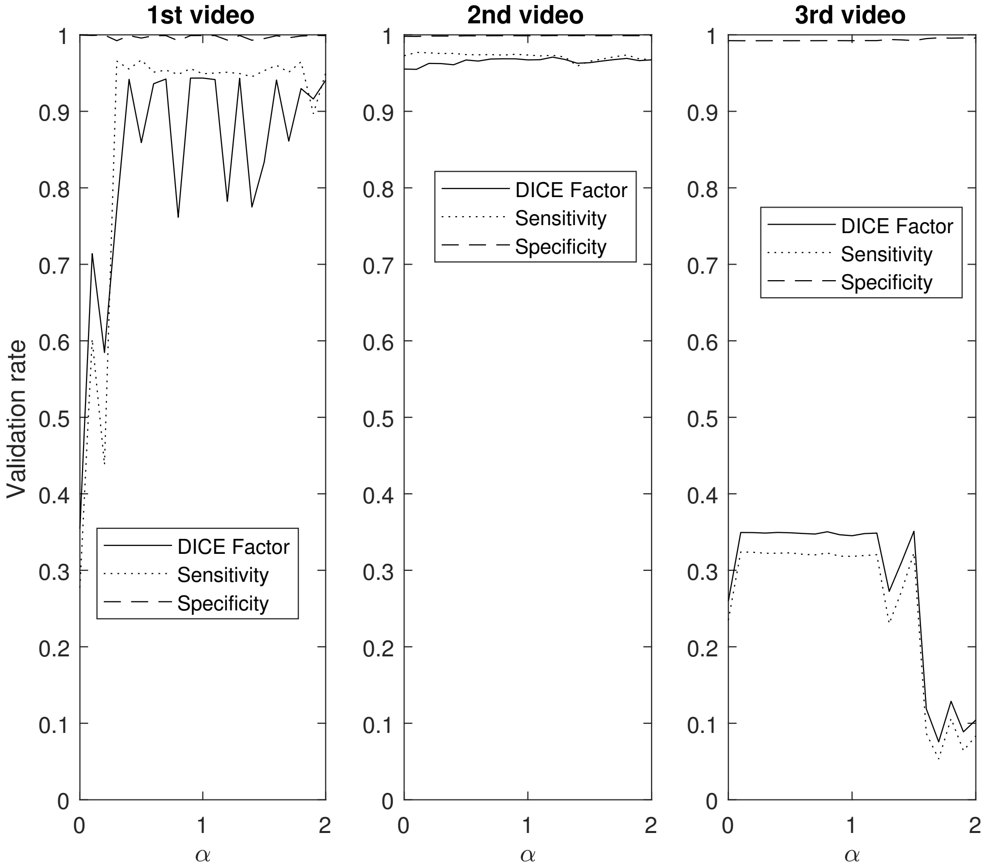

Figure 5.5: The validation rates in terms of DF, sensitivity, and specificity versus the parameter α.

5.5.3 Influence of Contour Points Spacing

Here, we study the effect of contour points spacing on the accuracy of the Ad-PAC algorithm. In this study, after segmentation of each frame, the contour is re-sampled and the new value of N is chosen to be P/Λ, where P is the perimeter of the segmented contour, and Λ is the contour points spacing. Fig. 5.11 presents the average DICE factor obtained from all videos for different values of Λ. From this figure, one can see that the average DICE factor degrades quickly when the contour spacing is large and it improves when the contour spacing decreases but it nears saturation at $\Lambda = 5$

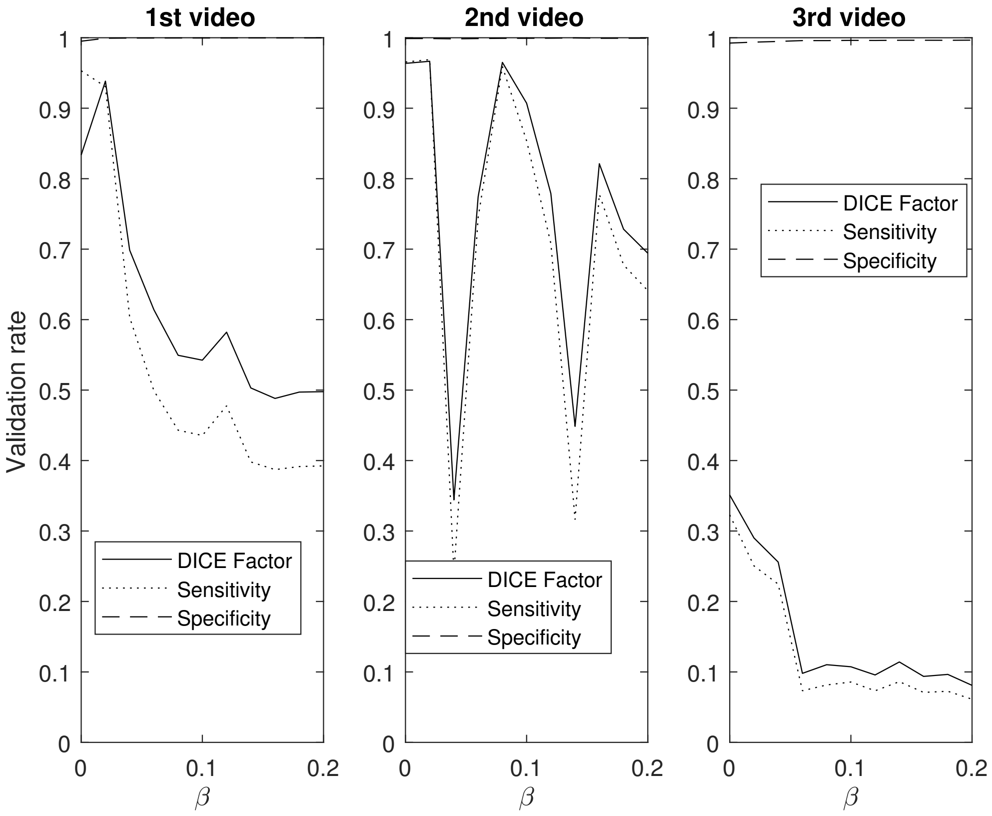

Figure 5.6: The validation rates in terms of DF, sensitivity, and specificity versus the parameter β.

pixels.

5.5.4 Tracking Performance

This section compares the tracking performance of the proposed Ad-PAC algorithm with the manual segmentation and other algorithms as per section V for two sample video as shown in Figs. 5.12 and 5.13, respectively. From both figures, it is evident that the proposed Ad-PAC algorithm outperforms the existing algorithms and produces results very close to the manual segmentation. Further supporting evidence that parameter adaption significantly improves the performance is evident in rows 3 and 4 row of Figs. 5.12 and 5.13. The segmented contour is not smooth without

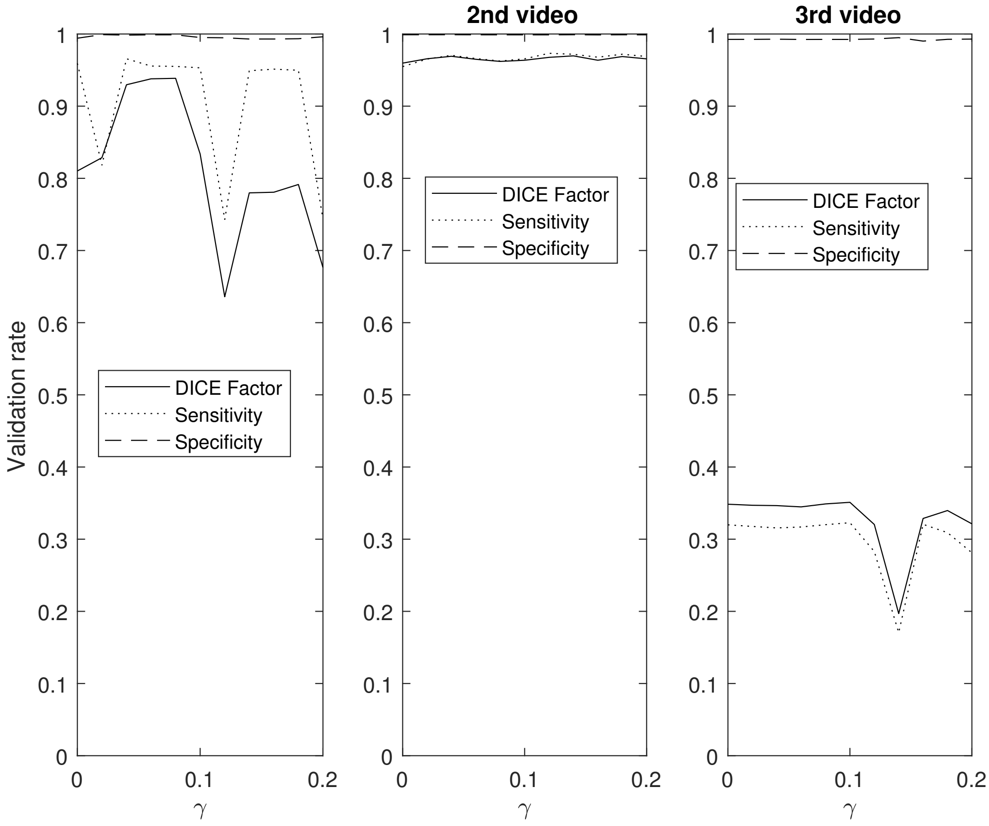

Figure 5.7: The validation rates in terms of DF, sensitivity, and specificity versus the parameter γ.

parameter adaptation (which is observed as spikes) suggesting that the weight given to the curvature energy term was not sufficiently large enough to compete with the other energy terms and consequently, dominated by them. Fig. 5.14 presents the DICE factors obtained from each algorithm, averaged across all 65 videos irrespective of IJV shape, intensity, speed of variation and quality. From this figure, it is clear that the proposed Ad-PAC algorithm outperforms all existing algorithms with its corresponding DICE factor greater than 0.64. Other algorithms perform significantly worse. In the following sub-sections, more detailed results are presented.

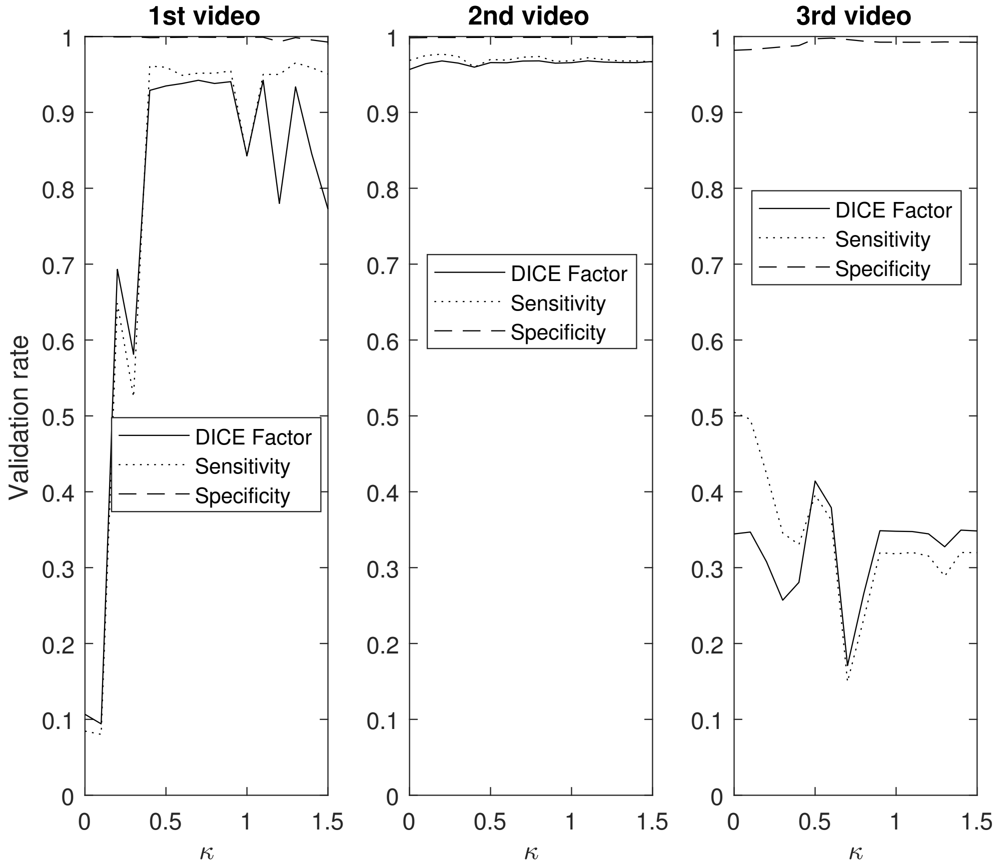

Figure 5.8: The validation rates in terms of DF, sensitivity, and specificity versus the parameter κ.

5.5.5 Influence of Image Quality

For this study, all videos were categorized, as good, average, and poor quality videos based on the blinded expert opinion. Fig. 5.15 illustrates the DICE results. In good quality ultrasound videos, as per Fig. 5.15-(a), the proposed Ad-PAC algorithm performs very close to the manual segmentation with a DICE factor consistently above 0.95. The minimum value of DICE factors for the other algorithms range from 0.91 down to 0.37 for the Geodesic algorithm [57].

In average quality videos, as shown in Fig. 5.15-(b), the performance of Ad-PAC algorithm drops as low as 0.65, however, it still outperforms the other AC algorithms.

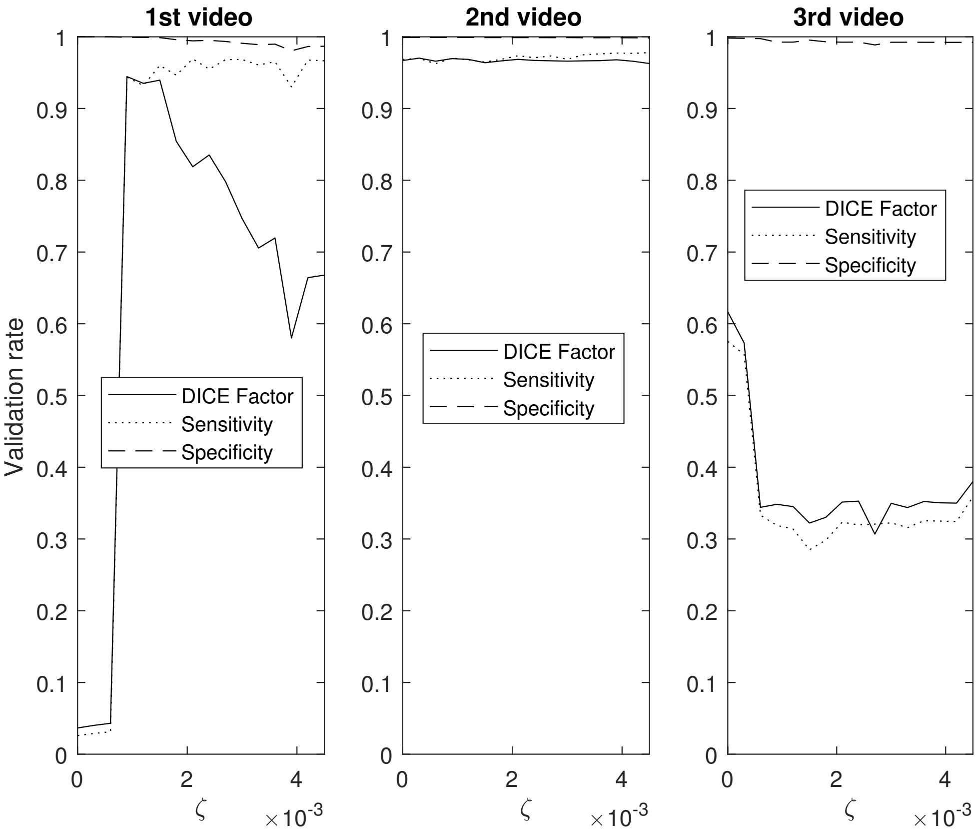

Figure 5.9: The validation rates in terms of DF, sensitivity, and specificity versus the parameter ζ.

Poor quality videos (Fig. 5.15-(c)) demonstrate the minimum DICE factor as being 0.55, still above other algorithms.

5.5.6 Influence of IJV Shape

The IJV shape also impacts the segmentation results. Oval objects tend to be more suiTable for polar representation whereas collapsed vessels tend to be much more challenging. The IJV represents a deformable model influenced by a number of factors including local anatomy, blood volume and blood flow. For this study, IJV videos are

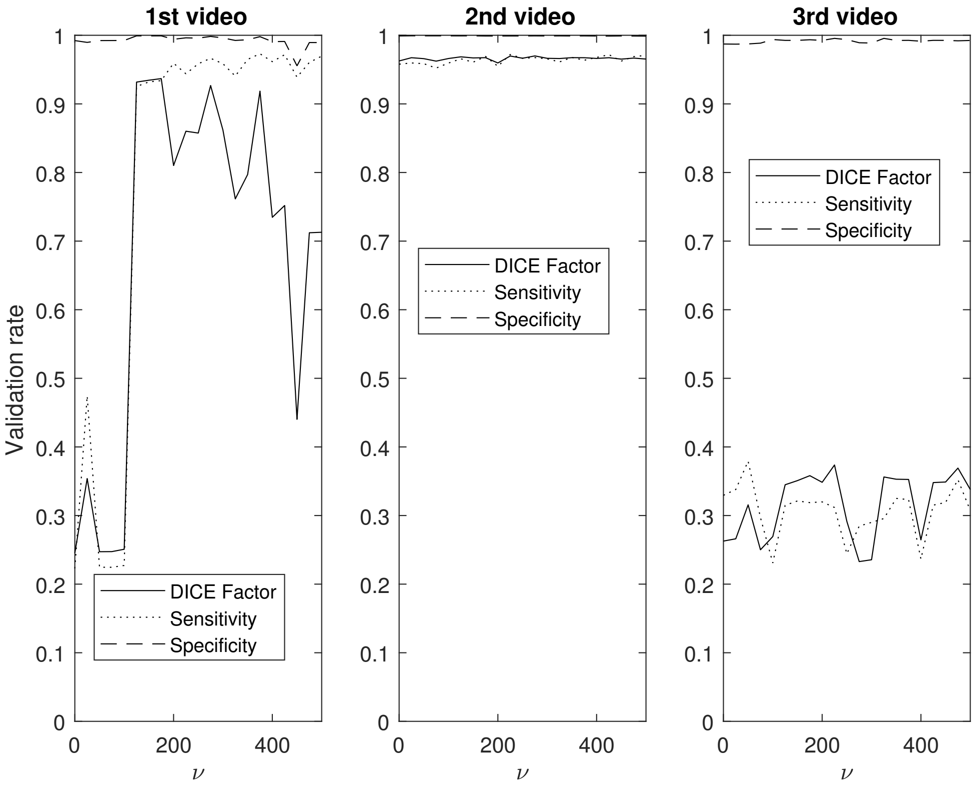

Figure 5.10: The validation rates in terms of DF, sensitivity, and specificity versus the parameter ν.

categorized into three categories being oval, 1+ apices, and fully collapsed. Fig. 5.16 presents the average DICE factor for the videos from each category. In Fig. 5.16-(a), it is evident that Ad-PAC performs close to manual segmentation when the IJV has an oval shape with a DICE coefficient greater than 0.90. The second best performance belongs to the proposed energy functional without temporal adaptation having an average DICE coefficient larger than 0.83. Fig. 5.16-(b) shows that the IJV with 1+ apices result in the Ad-PAC performance as low as 0.50 but above other algorithms. Again, the proposed energy functional without temporal adaptation is the second best algorithm with a minimum DICE factor as low as 0.48. Is is only when the IJV is fully collapsed does the Ad-PAC algorithm under-perform the algorithm without

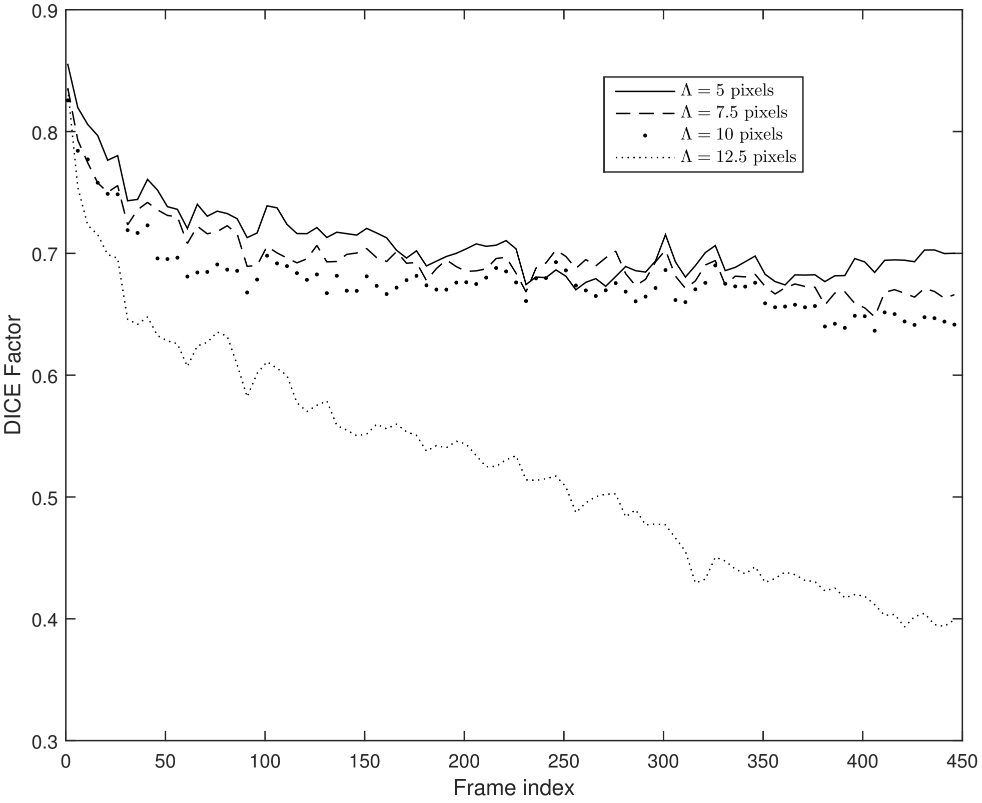

Figure 5.11: Influence of contour spacing Λ on the accuracy of Ad-PAC segmentation.

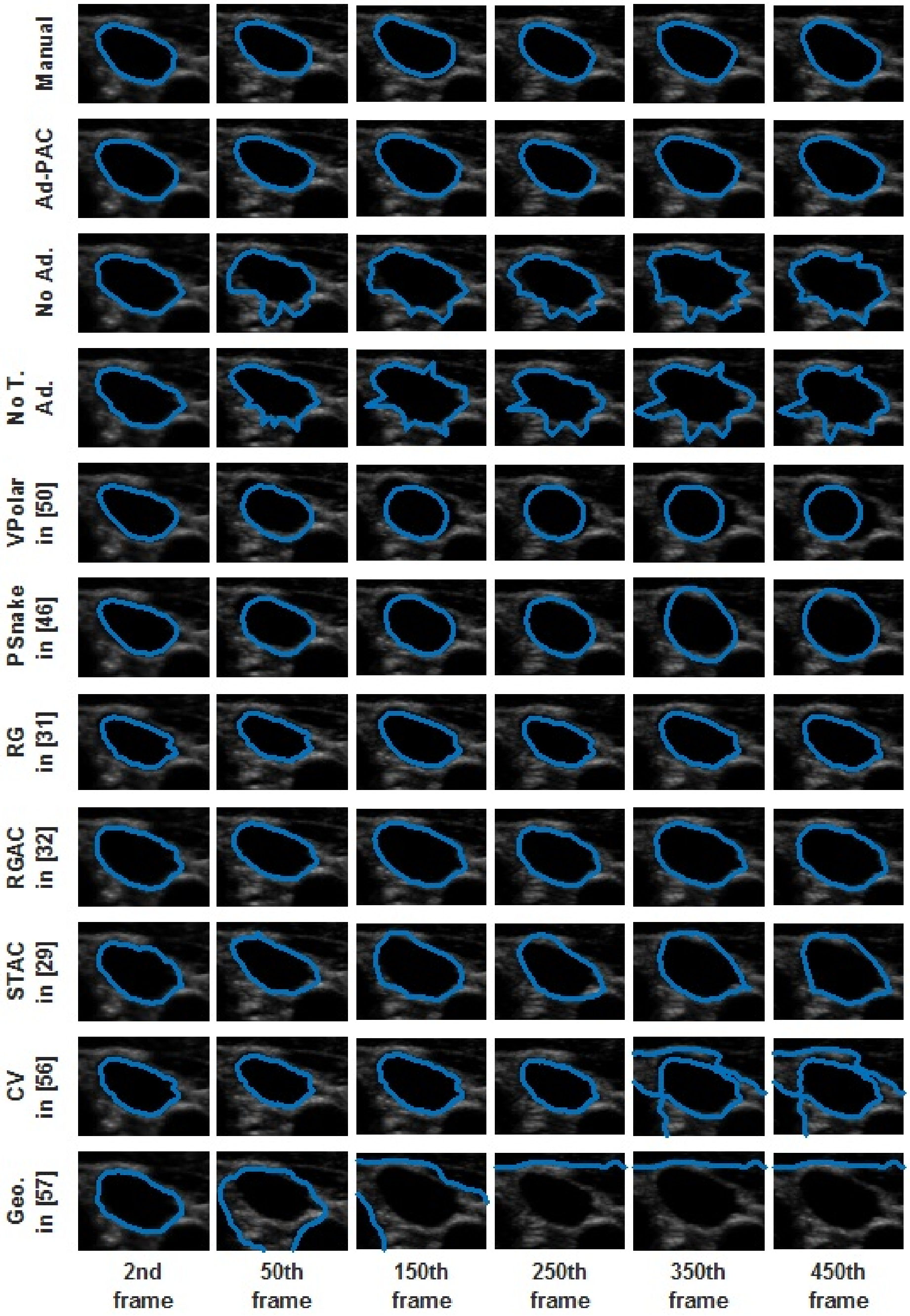

Figure 5.12: Tracking of the IJV in a good quality video for manual segmentation, Ad-PAC and eight other algorithms.

adaptation and in the worst case, the DICE factor drops to 0.19. This is a limitation of the polar contour model for fully collapsed objects such as the empty IJV.

5.5.7 Influence of IJV Variation

The CSA of the IJV undergoes a wide range of variation that typically present a challenge for AC models as they are relatively sensitive to this parameter. This often results in a failure to track and converge to the edges of the object. To study the influence of variation, the ultrasound videos were categorized into three groups i) less than 10 percent, ii) between 10 and 90 percent and iii) more than 90 percent variations. Note that, in the case of more than 90 percent variation, the IJV shape deforms from oval or 1+ apical shape to fully collapsed, resulting in this category resembling the one in Fig. 5.16-(c). The numerical results based on this categorization are shown in Fig. 5.17. As one can see from Fig. 5.16-(a), when the CSA of the IJV undergoes small variations, the average DICE factor is always greater than 0.94. In Fig. 5.16-(b) with the variation between 10 to 90 percent, the Ad-PAC algorithm still performs well with an average DICE factor of 0.64 and still outperforms the other algorithms. Finally from Fig. 5.16-(c), it is observed that when the IJV undergoes large variations, all algorithms gradually lose tracking. Ad-PAC algorithm does not always outperform Ad-PAC without adaptation in these scenarios.

5.6 Conclusion and Future Work

In this section, a novel adaptive polar active contour model (Ad-PAC) is developed for the segmentation and tracking of the internal jugular vein (IJV) in ultrasound imagery. In the proposed algorithm, the parameters of the energy functional are initialized and locally adapted to the contour features extracted in previous frames. We demonstrate that the extra processing required for parameter adaptation is negligible and that the proposed Ad-PAC algorithm performs well compared with manual segmentation while outperforming multiple existing algorithms across a broad range of image features including image quality, intensity, and temporal variation.

Although the proposed Ad-PAC algorithm still outperforms existing AC algorithms, as the future work, the cases of poor image quality or fully-collapsed IJV can be addressed by incorporating additional information into its energy functional. Furthermore, the focus of this Chapter centered on the energy functional and parameter adaptation with future work being directed at improving the speed and accuracy of the functional minimization through developing more efficient techniques. Finally, additional clinical research is required to fully evaluate the ability of the Ad-PAC algorithm to detect relative changes in circulating blood volume with the intent of predicting when patients with congestive heart failure are at risk of clinical deterioration and subsequent hospitalization.

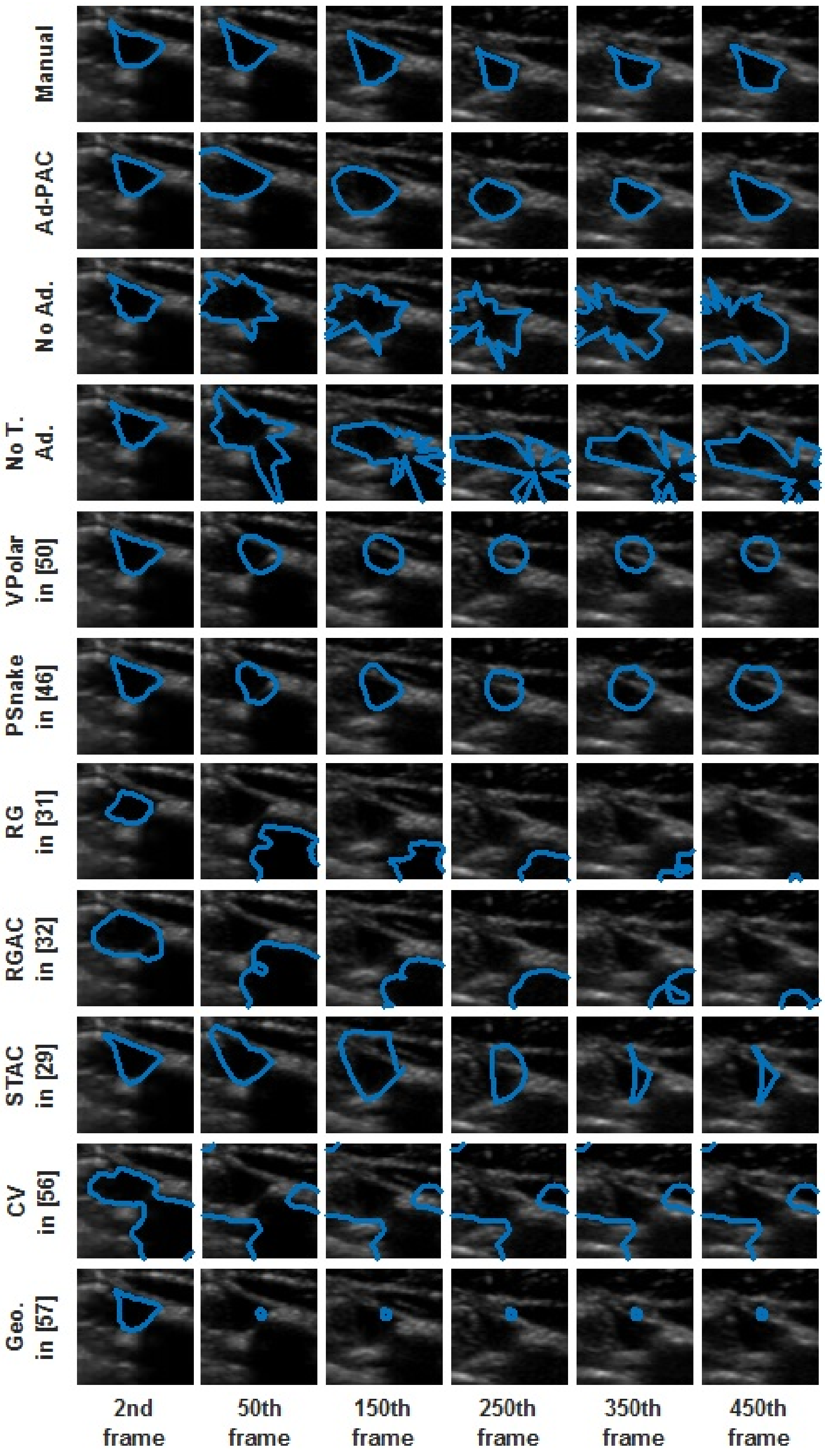

Figure 5.13: Tracking of the IJV in a poor quality video for manual segmentation, Ad-PAC and eight other algorithms.

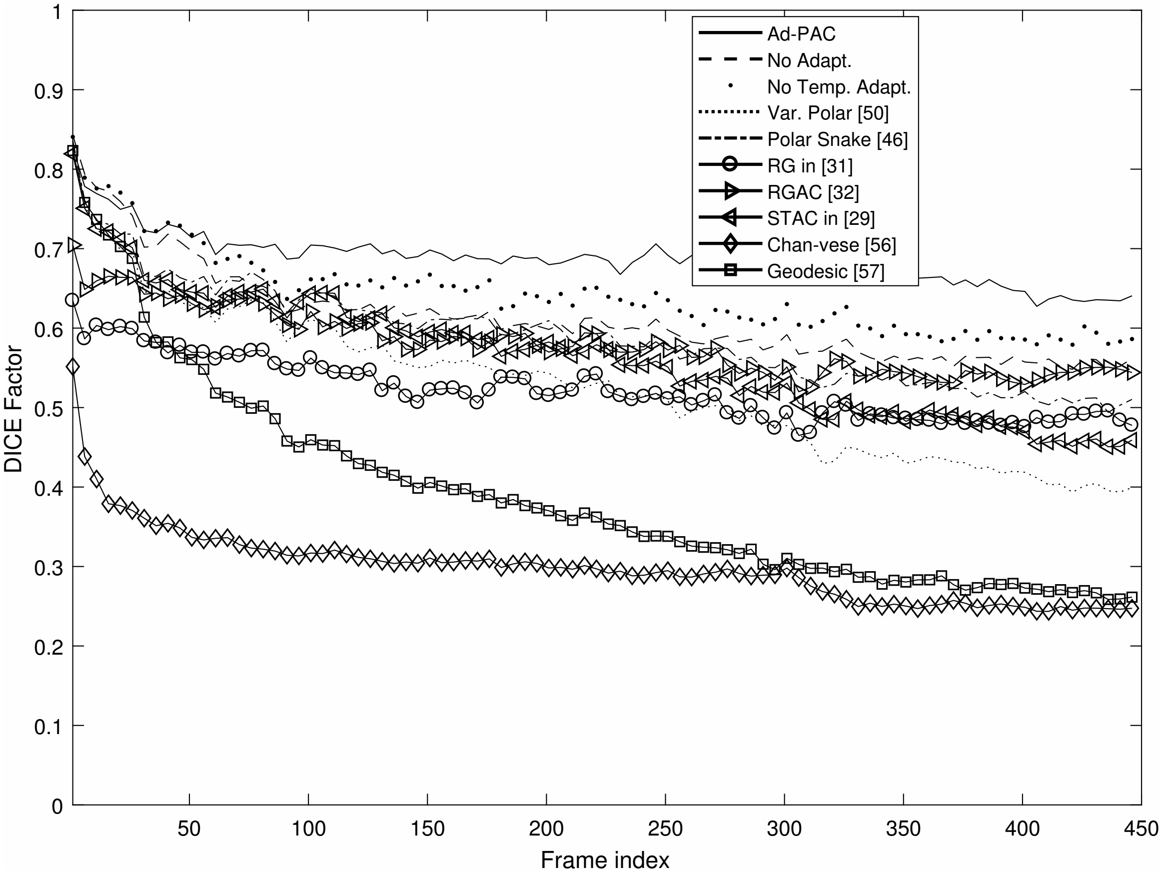

Figure 5.14: The mean level of agreement between algorithm and manual segmentation versus frame index.

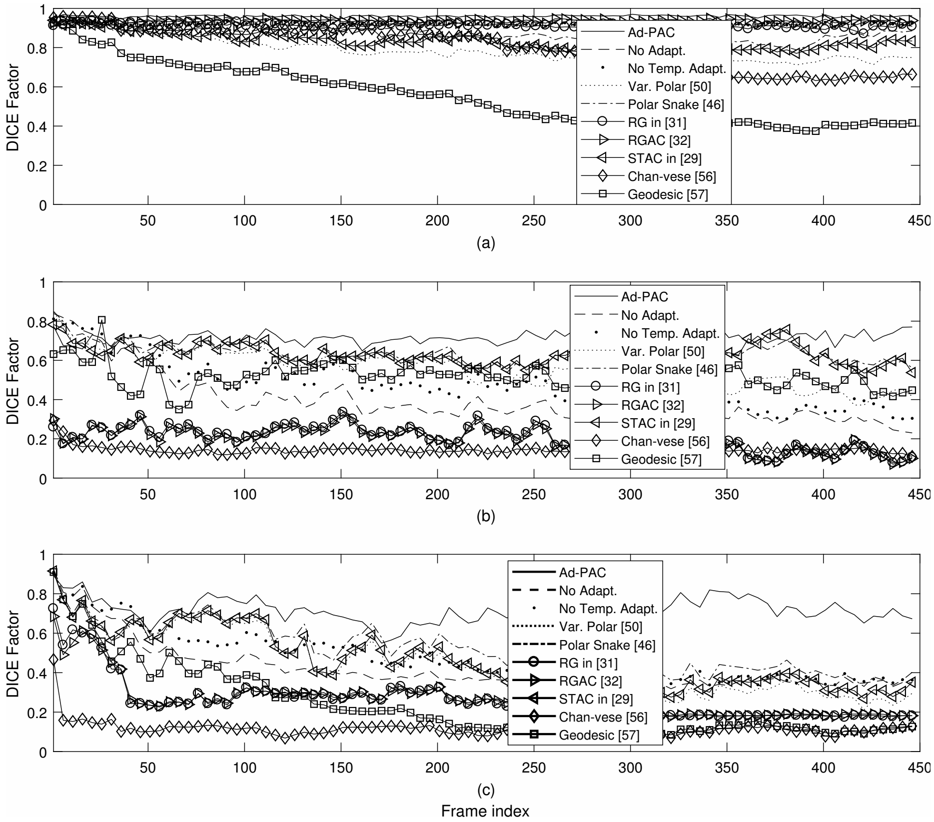

Figure 5.15: The average level of agreement with manual segmentation versus frame index for ultrasound videos with (a) good, (b) average, and (c) poor qualities.

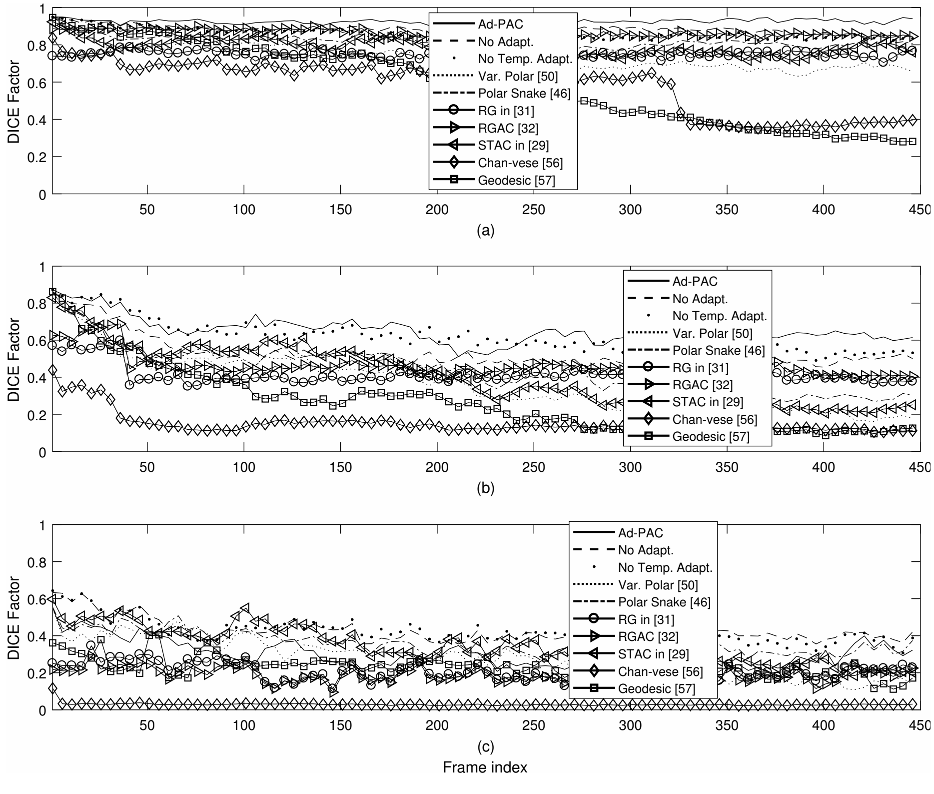

Figure 5.16: The average level of agreement with manual segmentation versus frame index for (a) oval shape, (b) 1+ apices shape, (c) fully collapsed videos.

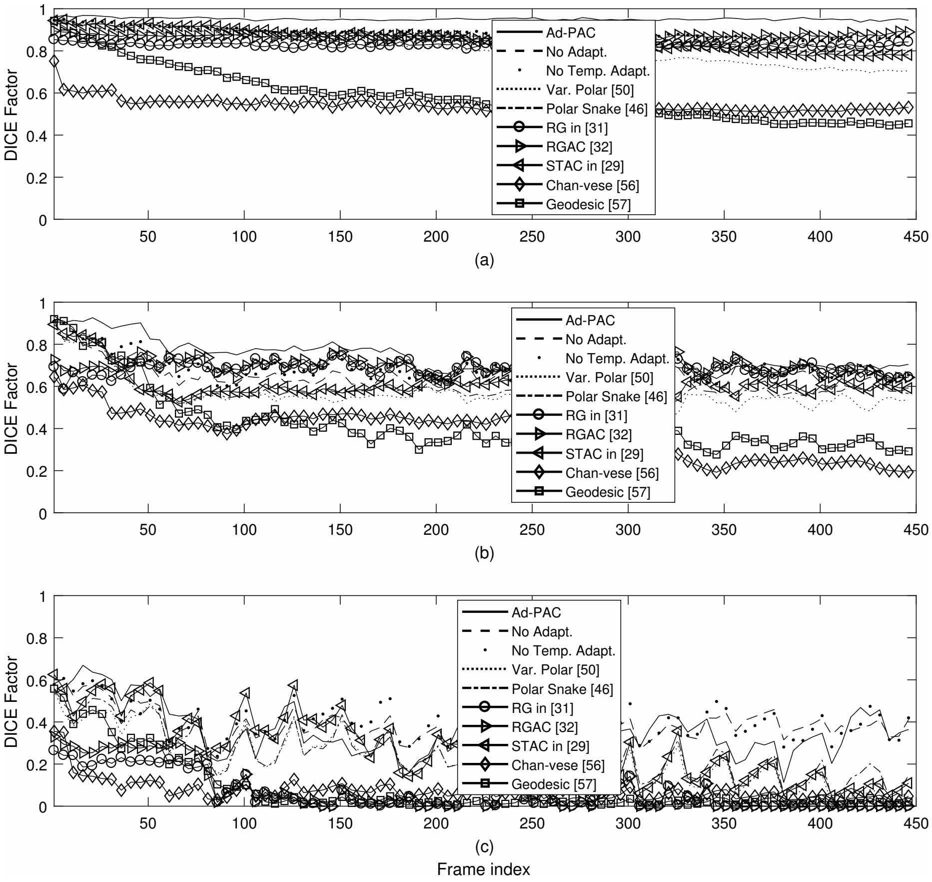

Figure 5.17: The average level of agreement with manual segmentation for IJV videos with (a) less than 10% variation, (b) 10-90% variation, (c) greater than 90% variation.

References

[1] Robert R Steuer, David H Harris, and James M Conis. A new optical technique for monitoring hematocrit and circulating blood volume: Its application in renal dialysis. *Dialysis & transplantation*, 22(5):260–265, 1993.

[2] Tadashi Kudo, Shigeharu Suzuki, and Takashi Iwabuehi. Importance of monitoring the circulating blood volume in patients with cerebral vasospasm after subarachnoid hemorrhage. *Neurosurgery*, 9(5):514–520, 1981. doi: 10.1227/00006123-198111000-00004.

[3] H. Kasuya, H. Onda, T. Yoneyama, T. Sasaki, and T. Hori. Bedside monitoring of circulating blood volume after subarachnoid hemorrhage. *Stroke*, 34(4):956–960, 2003. doi: 10.1161/01.str.0000064321.10700.63.

[4] M. Yashiro, Y. Hamada, H. Matsushima, and E. Muso. Estimation of filtration coefficients and circulating plasma volume by continuously monitoring hematocrit during hemodialysis. *Blood Purif Blood Purification*, 20(6):569–576, 2003. doi: 10.1159/000066957.

[5] Frank Bremer, Albert Schiele, Jan Sagkob, Thomas Palmaers, and Klaus Tschaikowsky. Perioperative monitoring of circulating and central blood volume in cardiac surgery by pulse dye densitometry. *Intensive Care Med Intensive Care Medicine*, 30(11):2053–2059, 2004. doi: 10.1007/s00134-004-2445-8.

[6] P Bose, F Regan, and S Paterson-Brown. Improving the accuracy of estimated blood loss at obstetric haemorrhage using clinical reconstructions. *BJOG: An International Journal of Obstetrics & Gynaecology*, 113(8):919–924, 2006.

[7] J. Kevin Bailey, John Mccall, Suzanne Smith, and Richard J. Kagan. Correlation of internal jugular vein/common carotid artery ratio to central ve-

nous pressure. *Journal of Burn Care & Research*, 33(1):89–92, 2012. doi: 10.1097/bcr.0b013e318234d965.

[8] Kasana Raksamani, Vachira Udompornmongkol, Suwannee Suraseranivongse, Manee Raksakietisak, and Benno Von Bormann. Correlation between cross-sectional area of the internal jugular vein and central venous pressure. *European Journal of Anaesthesiology*, 31(1):50–51, 2014. doi: 10.1097/eja.0b013e32835f9a50.

[9] Shashi Bala and Amit Doegar. Automatic detection of sickle cell in red blood cell using watershed segmentation. *Blood*, 4(6), 2015.

[10] Jean Serra and Pierre Soille. *Mathematical morphology and its applications to image processing*, volume 2. Springer Science & Business Media, 2012.

[11] Stefano Diciotti, Simone Lombardo, Massimo Falchini, Giulia Picozzi, and Mario Mascalchi. Automated segmentation refinement of small lung nodules in ct scans by local shape analysis. *IEEE Transactions on Biomedical Engineering*, 58(12): 3418–3428, 2011.

[12] Reyer Zwiggelaar, Yanong Zhu, and Stuart Williams. Semi-automatic segmentation of the prostate. In *Iberian Conference on Pattern Recognition and Image Analysis*, pages 1108–1116. Springer, 2003.

[13] Jun Xie, Yifeng Jiang, and Hung-tat Tsui. Segmentation of kidney from ultrasound images based on texture and shape priors. *IEEE transactions on medical imaging*, 24(1):45–57, 2005.

[14] Peter Karasev, Ivan Kolesov, Karl Fritscher, Patricio Vela, Phillip Mitchell, and Allen Tannenbaum. Interactive medical image segmentation using pde control of active contours. *IEEE transactions on medical imaging*, 32(11):2127–2139, 2013.

[15] Thiago Vallin Spina, Paulo AV de Miranda, and Alexandre Xavier Falcão. Hybrid approaches for interactive image segmentation using the live markers paradigm. *IEEE Transactions on Image Processing*, 23(12):5756–5769, 2014.

[16] Brian L Price, Bryan Morse, and Scott Cohen. Geodesic graph cut for interactive image segmentation. In *Computer Vision and Pattern Recognition (CVPR), 2010 IEEE Conference on*, pages 3161–3168. IEEE, 2010.

[17] Damien Grosgeorge, Caroline Petitjean, J-N Dacher, and Su Ruan. Graph cut segmentation with a statistical shape model in cardiac mri. *Computer Vision and Image Understanding*, 117(9):1027–1035, 2013.

[18] Dwarikanath Mahapatra and Joachim M Buhmann. Automatic cardiac rv segmentation using semantic information with graph cuts. In *2013 IEEE 10th International Symposium on Biomedical Imaging*, pages 1106–1109. IEEE, 2013.

[19] Leila Meziou, Aymeric Histace, and Frédéric Precioso. Alpha-divergence maximization for statistical region-based active contour segmentation with non-parametric pdf estimations. In *2012 IEEE International Conference on Acoustics, Speech and Signal Processing (ICASSP)*, pages 861–864. IEEE, 2012.

[20] Weiming Wang, Lei Zhu, Jing Qin, Yim-Pan Chui, Bing Nan Li, and Pheng-Ann Heng. Multiscale geodesic active contours for ultrasound image segmentation using speckle reducing anisotropic diffusion. *Optics and Lasers in Engineering*, 54:105–116, 2014.

[21] Paul A Yushkevich, Joseph Piven, Heather Cody Hazlett, Rachel Gimpel Smith, Sean Ho, James C Gee, and Guido Gerig. User-guided 3d active contour segmentation of anatomical structures: significantly improved efficiency and reliability. *Neuroimage*, 31(3):1116–1128, 2006.

[22] Bashir Al-Diri, Andrew Hunter, and David Steel. An active contour model for segmenting and measuring retinal vessels. *IEEE Transactions on Medical imaging*, 28(9):1488–1497, 2009.

[23] Nikos Paragios and Rachid Deriche. Geodesic active contours and level sets for the detection and tracking of moving objects. *IEEE Transactions on pattern analysis and machine intelligence*, 22(3):266–280, 2000.

[24] Pablo Mesejo, Andrea Valsecchi, Linda Marrakchi-Kacem, Stefano Cagnoni, and Sergio Damas. Biomedical image segmentation using geometric deformable models and metaheuristics. *Computerized Medical Imaging and Graphics*, 43:167–178, 2015.

[25] Zhen Ma, Renato M Natal Jorge, Teresa Mascarenhas, and João Manuel RS Tavares. Segmentation of female pelvic organs in axial magnetic resonance images using coupled geometric deformable models. *Computers in biology and medicine*, 43(4):248–258, 2013.

[26] Myungeun Lee, Wanhyun Cho, Sunworl Kim, Soonyoung Park, and Jong Hyo Kim. Segmentation of interest region in medical volume images using geometric deformable model. *Computers in biology and medicine*, 42(5):523–537, 2012.

[27] Peter J Yim and David J Foran. Volumetry of hepatic metastases in computed tomography using the watershed and active contour algorithms. In *Computer-Based Medical Systems, 2003. Proceedings. 16th IEEE Symposium*, pages 329–335. IEEE, 2003.

[28] Sahirzeeshan Ali and Anant Madabhushi. An integrated region-, boundary-, shape-based active contour for multiple object overlap resolution in histological imagery. *IEEE transactions on medical imaging*, 31(7):1448–1460, 2012.

[29] Kun Qian, Takehiro Ando, Kensuke Nakamura, Hongen Liao, Etsuko Kobayashi, Naoki Yahagi, and Ichiro Sakuma. Ultrasound imaging method for internal jugular vein measurement and estimation of circulating blood volume. *International journal of computer assisted radiology and surgery*, 9(2):231–239, 2014.

[30] Jens-Uwe Voigt, Gianni Pedrizzetti, Peter Lysyansky, Tom H Marwick, Helen Houle, Rolf Baumann, Stefano Pedri, Yasuhiro Ito, Yasuhiko Abe, Stephen Metz, et al. Definitions for a common standard for 2d speckle tracking echocardiography: consensus document of the eacvi/ase/industry task force to standardize deformation imaging. *Eur Heart J Cardiovasc Imaging*, page jeu184, 2014.

[31] Jie Wu, Skip Poehlman, Michael D Noseworthy, and Markad V Kamath. Texture feature based automated seeded region growing in abdominal mri segmentation. In *2008 International Conference on BioMedical Engineering and Informatics*, volume 2, pages 263–267. IEEE, 2008.

[32] E Karami, M Shehata, P McGuire, and A Smith. A semi-automated technique for internal jugular vein segmentation in ultrasound images using active contours. In *2016 IEEE-EMBS International Conference on Biomedical and Health Informatics (BHI)*, pages 184–187. IEEE, 2016.

[33] Sahirzeeshan Ali and Anant Madabhushi. An integrated region-, boundary-, shape-based active contour for multiple object overlap resolution in histological imagery. *IEEE transactions on medical imaging*, 31(7):1448–1460, 2012.

[34] Shanhui Sun, Christian Bauer, and Reinhard Beichel. Automated 3-d segmentation of lungs with lung cancer in ct data using a novel robust active shape model approach. *IEEE transactions on medical imaging*, 31(2):449–460, 2012.

[35] Julian Guerrero, Septimiu E Salcudean, James A McEwen, Bassam A Masri, and

Savvakis Nicolaou. Real-time vessel segmentation and tracking for ultrasound imaging applications. *IEEE transactions on medical imaging*, 26(8):1079–1090, 2007.

[36] Fabrice Moscheni, Sushil Bhattacharjee, and Murat Kunt. Spatio-temporal segmentation based on region merging. *IEEE transactions on pattern analysis and machine intelligence*, 20(9):897–915, 1998.

[37] Jie Chen, Guoying Zhao, Mikko Salo, Esa Rahtu, and Matti Pietikainen. Automatic dynamic texture segmentation using local descriptors and optical flow. *IEEE Transactions on Image Processing*, 22(1):326–339, 2013.

[38] Ghassan Hamarneh and Tomas Gustavsson. Deformable spatio-temporal shape models: extending active shape models to 2d+ time. *Image and Vision Computing*, 22(6):461–470, 2004.

[39] Ebrahim Karami, Mohamed S Shehata, and Andrew Smith. Tracking of the internal jugular vein in ultrasound images using optical flow. In *The 30th Annual IEEE Canadian Conference on Electrical and Computer Engineering (CCECE), Windsor, Canada*, pages 1–4. IEEE, 2017.

[40] Hongsheng Li, Tian Shen, Dimitrios Vavylonis, and Xiaolei Huang. Actin filament segmentation using spatiotemporal active-surface and active-contour models. In *International Conference on Medical Image Computing and Computer-Assisted Intervention*, pages 86–94. Springer, 2010.

[41] Steven C Mitchell, Johan G Bosch, Boudewijn PF Lelieveldt, Rob J Van der Geest, Johan HC Reiber, and Milan Sonka. 3-d active appearance models: segmentation of cardiac mr and ultrasound images. *IEEE transactions on medical imaging*, 21(9):1167–1178, 2002.

[42] Kang Li, Xiaodong Wu, Danny Z Chen, and Milan Sonka. Optimal surface segmentation in volumetric images-a graph-theoretic approach. *IEEE transactions on pattern analysis and machine intelligence*, 28(1):119–134, 2006.

[43] Mirko Ristivojevic and Janusz Konrad. Space-time image sequence analysis: object tunnels and occlusion volumes. *IEEE Transactions on Image Processing*, 15(2):364–376, 2006.

[44] Matthew B Smith, Hongsheng Li, Tian Shen, Xiaolei Huang, Eddy Yusuf, and Dimitrios Vavylonis. Segmentation and tracking of cytoskeletal filaments using open active contours. *Cytoskeleton*, 67(11):693–705, 2010.

[45] Wangmeng Zuo, Kuanquan Wang, David Zhang, and Hongshi Zhang. Combination of polar edge detection and active contour model for automated tongue segmentation. In *Image and Graphics (ICIG'04), Third International Conference on*, pages 270–273. IEEE, 2004.

[46] Christophe Collewet. Polar snakes: A fast and robust parametric active contour model. In *2009 16th IEEE International Conference on Image Processing (ICIP)*, pages 3013–3016. IEEE, 2009.

[47] Maximilian Baust and Nassir Navab. A spherical harmonics shape model for level set segmentation. In *European Conference on Computer Vision*, pages 580–593. Springer, 2010.

[48] E Karami, M Shehata, and A Smith. Segmentation and tracking of inferior vena cava in ultrasound images using a novel polar active contour algorithm. In *5th IEEE Global Conference on Signal and Information Processing, GlobalSIP2017*, pages 1–5. IEEE, 2017.

[49] George D Giannoglou, Yiannis S Chatzizisis, Vassilis Koutkias, Ioannis Kompatsiaris, Maria Papadogiorgaki, Vasileios Mezaris, Eirini Parissi, Panagiotis Diamantopoulos, Michael G Strintzis, Nicos Maglaveras, et al. A novel active contour model for fully automated segmentation of intravascular ultrasound images: in vivo validation in human coronary arteries. *Computers in biology and medicine*, 37(9):1292–1302, 2007.

[50] Maximilian Baust, Anthony J Yezzi, Gozde Unal, and Nassir Navab. A sobolev-type metric for polar active contours. In *Computer Vision and Pattern Recognition (CVPR), 2011 IEEE Conference on*, pages 1017–1024. IEEE, 2011.

[51] Auzuir Ripardo De Alexandria, Paulo Cesar Cortez, Jessyca Almeida Bessa, John Hebert da Silva Felix, Jose Sebastiao De Abreu, and Victor Hugo C De Albuquerque. psnakes: A new radial active contour model and its application in the segmentation of the left ventricle from echocardiographic images. *Computer methods and programs in biomedicine*, 116(3):260–273, 2014.

[52] Xiaoyi Jiang and Daniel Tenbrinck. Region based contour detection by dynamic programming. In *International Conference on Computer Analysis of Images and Patterns*, pages 152–159. Springer, 2013.

[53] Frederick N Fritsch and Ralph E Carlson. Monotone piecewise cubic interpolation. *SIAM Journal on Numerical Analysis*, 17(2):238–246, 1980.

[54] David S Watkins. *Fundamentals of matrix computations*, volume 64. John Wiley & Sons, 2004.

[55] Erik Meijering and Michael Unser. A note on cubic convolution interpolation. *IEEE Transactions on Image processing*, 12(4):477–479, 2003.

[56] Tony F Chan and Luminita A Vese. Active contours without edges. *IEEE Transactions on image processing*, 10(2):266–277, 2001.

[57] Vicent Caselles, Ron Kimmel, and Guillermo Sapiro. Geodesic active contours. *International journal of computer vision*, 22(1):61–79, 1997.

[58] Lee R Dice. Measures of the amount of ecologic association between species. *Ecology*, 26(3):297–302, 1945.

Chapter 6

Localization of the IJV in Ultrasound Videos Using Deep Learning

Recent studies show that the relative changes in circulating blood volume is correlated with the cross-sectional area (CSA) of the internal jugular vein (IJV) that can be estimated from the bed-side ultrasound images. However, the localization of the IJV in ultrasound images is a challenging task as only a trained operator can discriminate the IJV from its surrounding tissues. In this Chapter, we propose a novel algorithm based on three dimensional (3D) convolutional neural networks (CNNs) to automatically localize the IJV in ultrasound videos. To exploit the information in the IJV walls motion, the input of the proposed CNN is a video patch extracted from 15 consecutive B-mode gray-scale ultrasound frames. The proposed algorithm uses a 3D sliding window (SW) method to search over the video patches and find the patches that overlap with the IJV CSA. Then the results obtained from different patches are fused and a point inside the IJV is detected. The proposed algorithm can be further combined with semi-automatic IJV segmentation algorithms in the literature to form a fully automatic segmentation algorithm. After training the proposed 3D CNNs with different input sizes, we show that an input video size $90 \times 90 \times 15$ provides the most accurate result. Although there are no previous works on this subject and the proposed algorithm is the first algorithm proposed for automatic localization of the IJV, we show that its results are acceptable as the point localized by the proposed algorithm is very close to the center of the IJV and the proposed algorithm helps medical operators to find the location of the IJV even in the context of poor quality images.

6.1 Introduction

The ability to non-invasively monitor circulating blood volume is important for a variety of medical conditions including congestive heart failure (CHF) [1, 2, 3, 4, 5, 6]. While accurate estimation of circulating blood volume remains elusive particularly in disease states [7, 8, 9], recent research suggest that the relative changes in circulating blood volume is correlated with changes in the inferior vena cava (IVC) and internal jugular vein (IJV) [10, 11]. Advances in portable ultrasound technology in combination with the development of algorithms capable of automatically identifying and segmenting large vessels such as the IVC and IJV will create new opportunities in medicine to optimize management of conditions such as CHF [12, 13, 14, 15].

Manual segmentation of the IJV is a time-consuming task making it inappropriate for segmentation of large ultrasound videos. On the other hand, fully automatic segmentation algorithms require prior knowledge about the images and hence, are applicable for segmentation of arteries which have a round shape [16]; however, due to elastic and unpredictable shape of the IJV, automatic segmentation of the IJV has been an unsolved problem and so far only semi-automatic algorithms have been proposed for segmentation of the IJV [15, 17, 18, 19].

Despite the availability, portable ultrasound image quality remains operator-dependent requiring segmentation algorithms achieve satisfactory performance characteristics across a wide spectrum of images [19]. Fig. 6.1 shows multiple sonographic images of the IJV in healthy and CHF patients. In [20], combination of speckle tracking and an active contour was proposed for segmentation of the IJV as several points on the IJV contour are manually selected by an operator and these points are tracked by a template matching algorithm. The coarse contour obtained from the template matching is smoothed by a simple active contour. Unfortunately, this algorithm fails when frame-by-frame deformation is not negligible - a commonly encountered issue with portable ultrasounds due to lower frame-rates. In [15], authors explored the combination of region growing and active contours however this performed poorly when artifact obscured parts of the vessel wall. Advances were made in [19] in which the authors proposed an adaptive polar active contour algorithm where the parameters of the active contour are locally and temporally adapted.

Recent advances in deep learning has seen the use of convolutional neural networks (CNNs) in many applications within the field of image processing. CNNs extract features of images using multiple convolutional and fully connected layers which in turn can be further processed or utilized for classification and regression applications. One specific application of CNNs is semantic segmentation, an approach in which each pixel is classified as either foreground or background [21]. Our previous research showed that semantic segmentation fails when it is used for ultrasound images of the IJV, and that for most IJV videos no foreground pixels are detected. This is mainly because of the fact that the manual segmentation used as the ground truth for the training of the CNNs is not very accurate and the boundary pixels inside the IJV can be mistakenly labeled as background and vice versa. Hence, in our research, we decided to employ CNNs for automatic detection of a point inside the IJV. The result of this research can simply be further combined with a semi-automatic algorithm such as the one in [15], to form a fully automatic IJV segmentation algorithm.

In this Chapter, we propose a novel algorithm based on 3D CNN to automatically localize IJV in ultrasound videos (the reason to use 3D CNNs is that even an expert usually cannot localize the IJV from a single frame and hence, multiple frames are required to localize the IJV from its motion pattern. A 3D CNN learns both spatial and temporal IJV patterns). In the proposed algorithm, a 3D CNN classifies the video patches extracted from the ultrasound video using a 3D sliding window (3D SW) into three classes as Inside, Overlap, and Outside of IJV. The 3D SW slides through the ultrasound video in both space and time dimensions and divides the ultrasound video into video patches. In the next step, the labels obtained from different video patches of a video are fused to find the location of the IJV by finding a point inside the IJV. In summary, this Chapter contributes:

- A novel 3D CNN model is proposed to classify subsections of IJV videos into one of three classes: Inside, Overlap, and Outside. For this purpose, we implemented and trained several 3D CNNs with different architectures and then by testing them, we selected the model that provides the best classification accuracy among them.

- A 3D sliding window (space and time) designed to capture input data for the 3D CNN model.

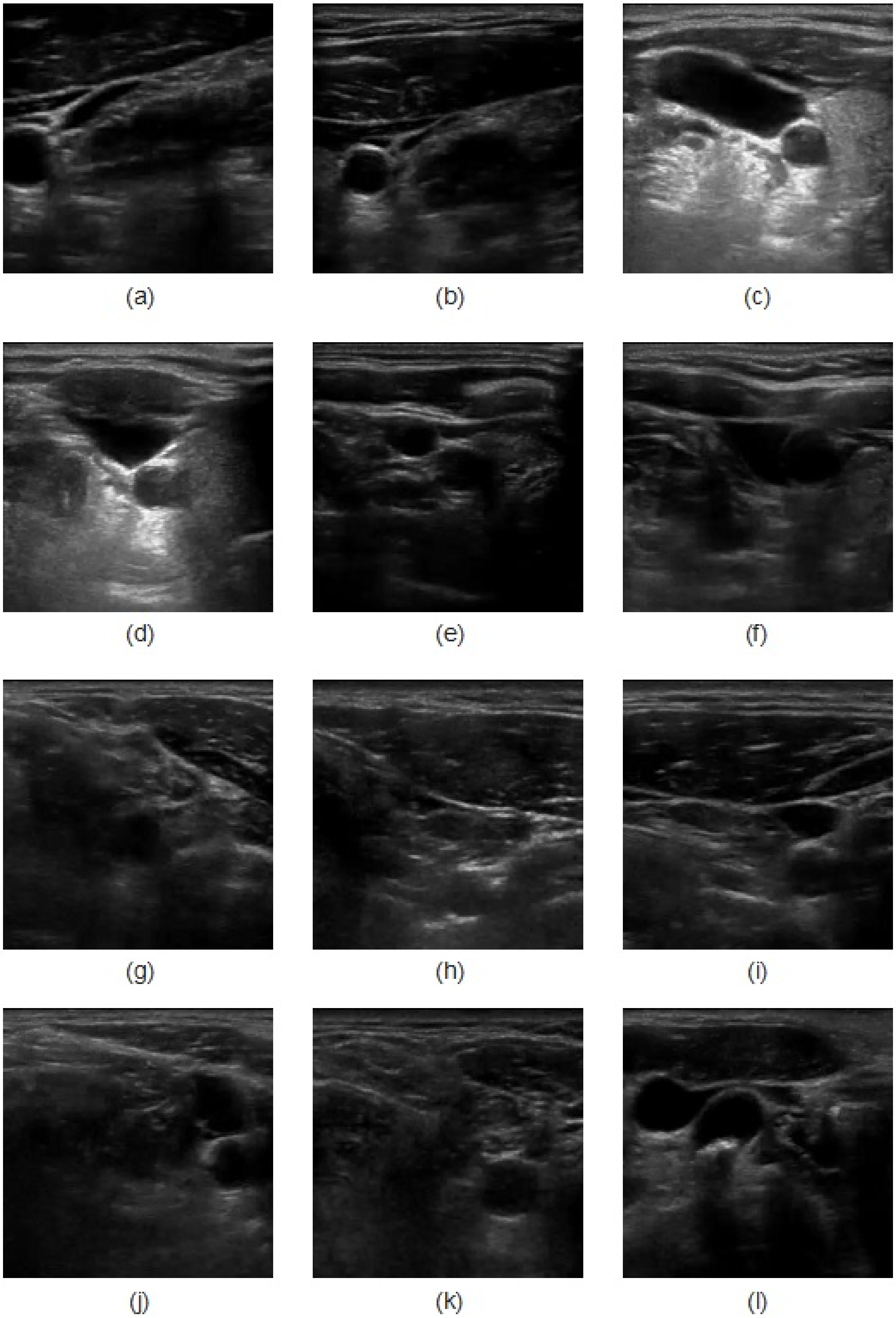

Figure 6.1: Sample IJV images from six healthy subjects ((a)-(f)), and six CHF patients ((g)-(l)).

- An efficient algorithm to fuse the labels that the trained 3D CNN produces for different video patches of a given video to find the exact location of the IJV in that video.

This Chapter is organized with Section 6.2 detailing the architecture of the 3D CNNs investigated in this research, Section 6.3 describing the data preparation and the training techniques, Section 6.4 discussed the proposed algorithm, Section 6.5 the results and Section 6.6 the conclusions.

6.2 The Architecture of the Proposed 3D CNNs

In this section, we discuss the 3D CNN architectures proposed for this research. In this research, we used CNNs with different patch sizes, number of frames in each video patch, and different number of convolutional encoder.

6.2.1 Layers Used to Built The Proposed 3D CNN

A CNN is a sequence of layers, where each layer extracts more features from the input data. The proposed 3D CNN performs a classification task and hence, to implement them we only need the layers needed in conventional classification CNNs as follows:

- Input layer: The only difference between a 3D CNN and a conventional 2D CNN is in its input layer size. In a conventional CNN the input layer size equals to the input image size which is $M_1 \times M_2 \times 3$ for color images, and $M_1 \times M_2 \times 1$ for gray scale images. In a 3D CNN that is used for video processing, the input layer size is $P \times Q \times 3 \times N$ for color videos and $P \times Q \times 1 \times N$ or equivalently $P \times Q \times N$ for gray scale videos, where N is the number of frames in the input video. Since the videos generated by a B-mode ultrasound machine are gray scale, in this research we use input layer size $P \times P \times N$, where $P \times P$ is the input patch size.

- Convolutional layer: A convolutional layer extracts the features from its input using a bank of 3D convolution filters with size of $F \times F \times C$. The size of output for each convolutional layer is controlled by two parameters as P for the zeros padded to each side of the images, and S as the stride factor.

- Rectifier linear unit (RELU) layer: RELU layer is the most commonly activation function used in CNNs and it simply thresholds the input at zero and does not change the input size.

- Pooling layer: It performs a spatial down-sampling operation where the rate of down-sampling is controlled with a stride factor.

- Fully connected (FC) layer, where each neuron in the previous layer is connected to one neuron in a FC layer. Due to the huge number of weights that connect the neurons in a FC layers to the neurons in the previous layers, FCs usually are defined with a dropout factor which indicates the ratio of the weights that are randomly selected and thrown away (or equivalently set to zero).

- Softmax Layer: A softmax layer receives the signals from the last fully connected layer and computes a probability for belonging to each class. In this research, we use the output of softmax layer for the proposed fusion algorithm.

- Classification Layer: Labels the input by finding the most likely class.

6.2.2 3D CNNs Architecture

Here, we briefly introduce the 3D CNN architectures implemented for this Chapter. For this research, we implemented 3D CNN with different input sizes and numbers of convolution encoders. Later after validating these models, we choose the model with the best classification accuracy for the IJV localization algorithm.

1. The C32N10L3 model, as shown in Fig. 6.2, has an input size $32 \times 32 \times 10$ and 3 convolutional layers. In Fig. 6.2, each of the first two blocks includes 32 $5 \times 5 \times 15$ convolutional filters with padding = 2 and stride = 1, followed by a RELU and a 3×3 max pooling layer with stride = 2. The third block has the same elements as the first two block but instead of 32 filter channels, it has 64 filter channels. The each of the fourth and fifth blocks has 64 neurons to combine the features extracted by the convolutional layers and the last block includes a 3-neurons fully connected layer that extract the information for the three classes followed by a softmax layer and finally a classification layer.

2. C32N30L3 model which has the same structure as C32N10L3 but with more frames, i.e, 30 frames, in its input.

3. Fig. 6.3 illustrates the C64N10L3 model which its input size is $64 \times 64 \times 10$ and has three convolutional layers. In Fig. 6.3, each of the first two blocks includes 96 $7 \times 7 \times 10$ convolutional filters with padding = 2 and stride = 1, followed by

a RELU and a 3 × 3 max pooling layer with stride = 2. The third block the same elements as the first two block but instead of 96 filter channels, it has 192 filter channels.

4. C64N15L3 model which has the same structure as C64N10L3 but with more frames, i.e, 15 frames, in its input.

5. C90N15L4, as shown in Fig. 6.4, has an input size 90 × 90 × 15 and four convolutional layers. In this figure, the first block includes 96 11 × 11 × 15 convolutional filters with Padding = 1 and stride = 2, followed by a RELU layer and a 3 × 3 max pooling layer with stride = 2. The second block includes 256 5 × 5 × 96 convolutional filters with Padding = 2 and stride = 1, followed by a RELU layer and a 3 × 3 max pooling layer with stride = 2. The third and fourth blocks include 384 3 × 3 × 256, and 256 3 × 3 × 384 convolutional filters, respectively, followed by a RELU layer. Each of the fully connected layers in the fifth and sixth blocks, includes 2048 neuron and a dropout rate 50%.

6. Fig. 6.5 illustrates the structure the C90N15L5 which has one convolutional layer more than the C90N15L4 model.

7. C90N15L6 model as shown in Fig. 6.6, has the same input size as C90N15L5 but with one additional convolutional layer.

8. C119N15L5 model which has the same parameters as C90N15L5 model but with the input size of 119 × 119 × 15.

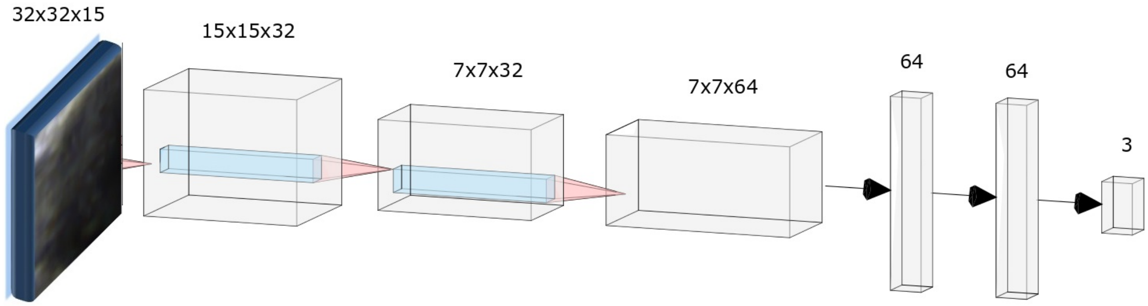

Figure 6.2: The architecture of the 3D CNN with video input size 32 × 32 × 15 and four convolutional encoders (C32N15L3).

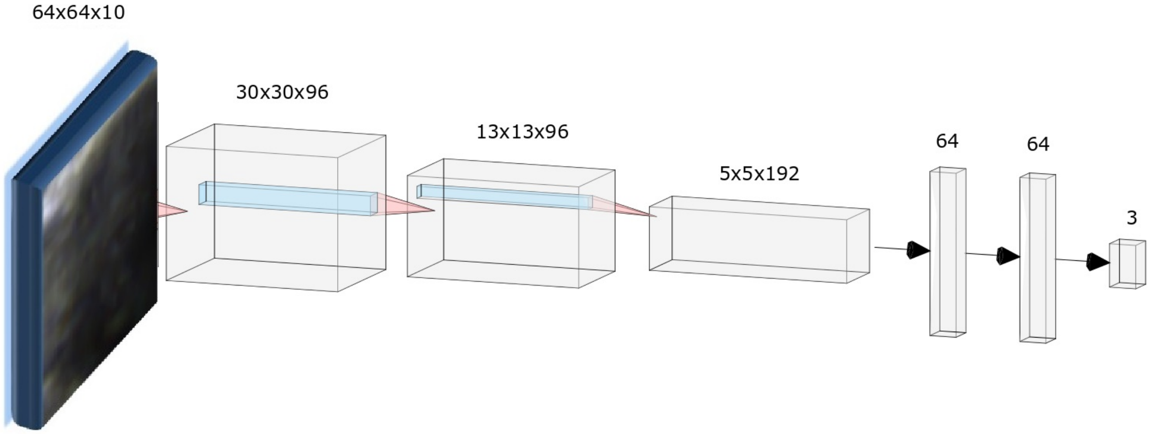

Figure 6.3: The architecture of the 3D CNN with video input size 32 × 32 × 15 and four convolutional encoders (C64N10L3).

All number of convolutional layers and filter sizes where chosen based on the input video size as for instance, in C32N10L3 and C32N30L3 models due it the smaller input size, only three convolutional layers are used. Note that by increasing the input size, although the amount of information in video patch and consequently the classification accuracy is increased, the spatial and temporal resolution of the localization algorithm is declined. For instance, the temporal resolution declines by increasing the number of frames in a the video patch as the location of the IJV is not the same in different frames.

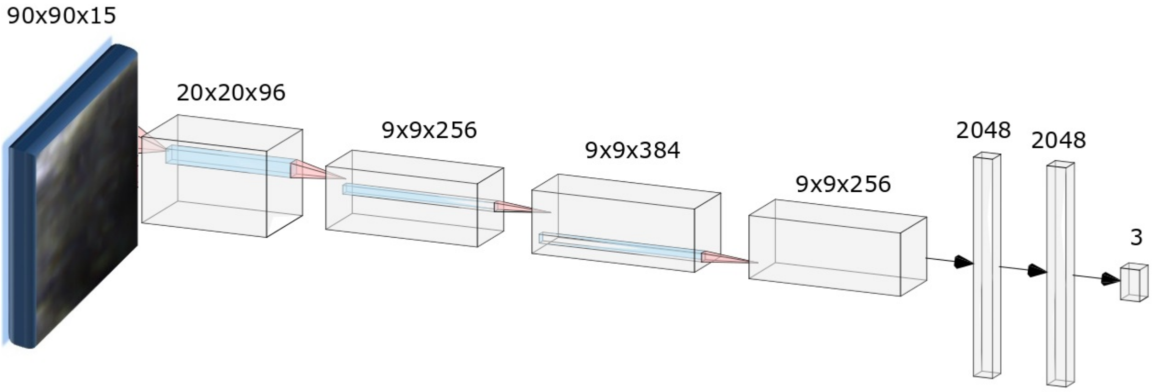

Figure 6.4: The architecture of the 3D CNN with video input size 90 × 90 × 15 and four convolutional encoders (C90N15L4).

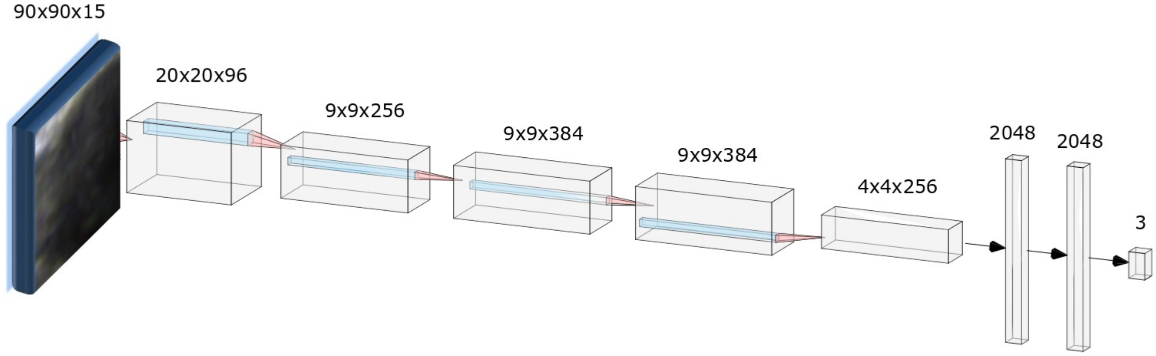

Figure 6.5: The architecture of the 3D CNN with image sequence input size 90×90×15 and five convolutional encoders (C90N15L5).

6.3 Data Preparation and Training of the CNNs

Two series of 68 and 140 IJV ultrasound videos were collected on 14 healthy subjects and 21 CHF patients respectively. Videos were collected with subjects lying, standing and at several angles of inclination in order to achieve different IJV size and fullness. The neck was imaged using a portable ultrasound (M-Turbo, Sonosite-FujiFilm) with a linear-array probe (6-15 Mhz), a frame rate of 30 fps and a frame size 480 × 640. Each video had a scan depth of 4-6cm and a duration of 15 seconds. All 68 videos from the healthy subjects were manually segmented frame-by-frame with 51 of these used to train the CNNs. All remaining segmented and unsegmented videos were used

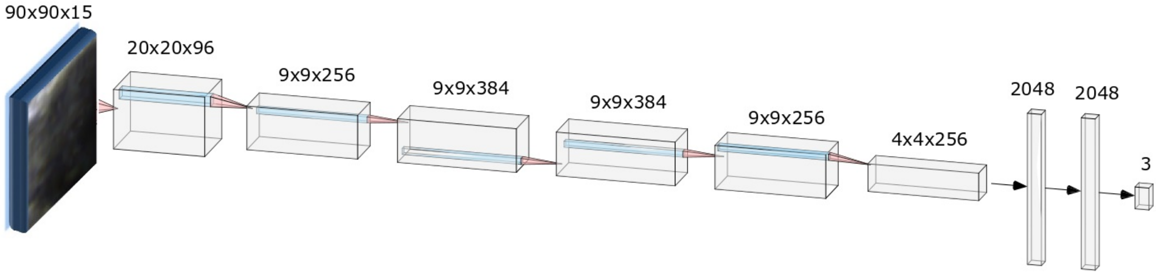

Figure 6.6: The architecture of the 3D CNN with image sequence input size 90×90×15 and six convolutional encoders (C90N15L5).

for testing and cross-validation of the trained CNNs as well as computing the accuracy of the proposed localization algorithm. This research was reviewed and approved by the local Health Research Ethics Authority.

6.3.1 Data Preparation

. Efficient training of the CNNs required the creation of a large training dataset from the 51 manually segmented videos. This was achieved using a 3D sliding window (SW) capturing a subset of spatial (x and y image axes) and temporal information from each ultrasound video.

Previously, we described the input of each 3D CNN as being a video patch including N, $P \times P$ image patches. To avoid a large correlation between training data sample, the 3D SW is shifted in intervals of 15 pixels in x and y dimensions and 10 frames over the third dimension (frame index). The labels are then created from the manually segmented videos using an equivalent 2D window whereas if the manually segmented IJV corresponding to the middle frame is completely inside the patch area, then the video patch is labeled as "Inside" and if it is completely outside the patch area, the path sequence is labels as "Outside", and otherwise, it is labeled as "Overlap".

To increase the amount of training data, we use data augmentation with scaling factors S =0.5 and 1. This not only increases the amount of the training data, but also helps with the class "Inside" as since IJV is usually larger that the selected patch sizes, with S =0.5, more video patches will fall under this class. In general, the majority of the video patches fall in the class "Outside" as typically a IJV occupies a small potion of the ultrasound video. On the contrary, for many of the IJV videos, the class "Inside" is not detected as typically the IJV only falls in this class if it is collapsed, i.e., when the subject is either dehydrated or in a standing position.

Fig. 6.7 illustrates one frame of the 90 × 90 × 15 video patch from the class "Inside", where a collapsed IJV is observed in the middle of the frame. This video belongs to a CHF patient in standing position. Fig. 6.8 depicts one frame from the same same dataset but from the class "Overlap" where part of the IJV is observed at the left side of the frame and Fig. 6.8 depicts one frame from class "Outside" where the entire IJV is outside the frame.

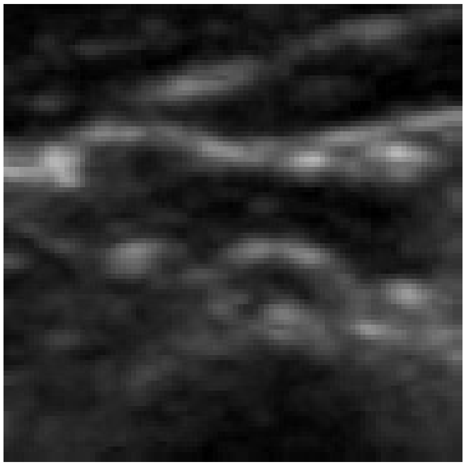

Figure 6.7: A sample ultrasound label patch where the IJV is entirely inside the patch.

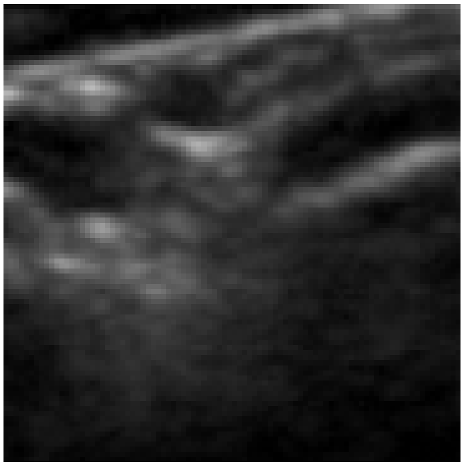

Figure 6.8: A sample ultrasound label patch where a part of the IJV is inside the patch.

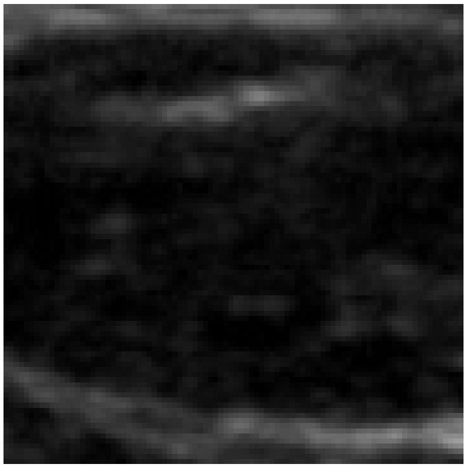

Figure 6.9: A sample ultrasound label patch where the IJV is entirely outside the patch.

6.3.2 Training the Implemented Models

After implementing the 3D CNNs models introduced in Section 6.2 and their corresponding datasets, we trained them on one CPU using MATLAB 2018b. The mini-batch size was set to 8 to avoid out of memory problems and the models trained over 100 Epochs. For each case, the parameters of the CNNs, such as the weights and bias factors, are randomly initialized with a zero-mean Gaussian distribution with variance of 0.01. The Nesterov accelerated gradient method with momentum 0.01 is used for the training [22].

Figs. 6.10-6.11 depict the activation map of the first and last convolutional layers of a trained C90N15L4 for the video patch depicted in Fig. 6.7.

6.4 The Proposed Algorithm

The proposed algorithm uses the output of the softmax layer, S, to find the center of the IJV. The output of the softmax layer is 3×1 vector where its elements show the probability that the patch belong to each of the three classes "Inside", "Overlap", and "Outside", respectively. In the proposed algorithm, we define a metric based on the first two elements of this vector as $Metric = 3s_1 + s_2$. Since the class "Inside" is more important than the class "Overlap", we give a larger weight to it. In other words, in a patch is labeled as "Inside", its center is expected to be closer to the center of the IJV than the center of a patch labeled as "Overlap". After we find this metric for all different video patches, we find the patches that their metric is larger than is a threshold and then we find the average of the center points for the selected patches. The proposed algorithm is summarized as below.

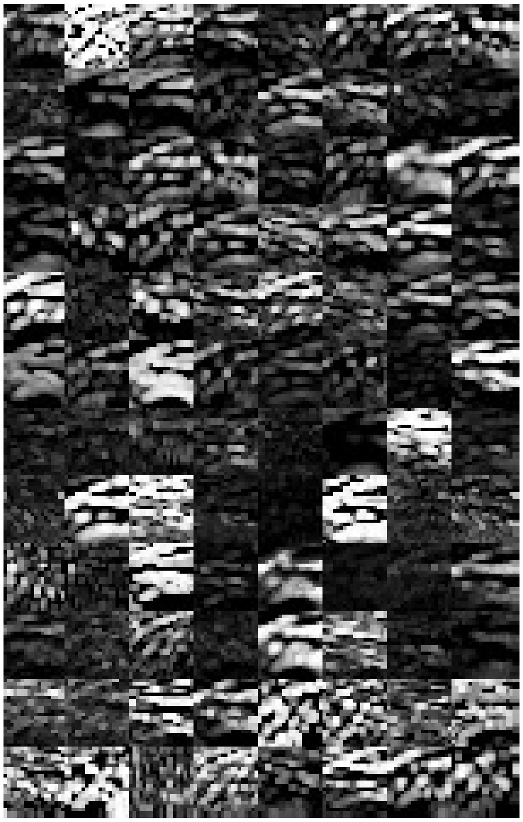

Figure 6.10: The activation map of the first convolutional layer in the trained C90N15L4.

Figure 6.11: The activation map of the fourth (last) convolutional layer in the trained C90N15L4.

The proposed algorithm

```
Input: An IJV ultrasound video including $N$ frames and a trained 3D CNN.
- Start from the top-left corner of the video and select the first video patch.
- Apply the selected video patch to the trained CNN and find the activation at the output vector of the softmax layer, i.e., $S$.
- Compute a metric for the patch as $Metric = 3s_1 + s_2$, where $s_1$ and $s_2$ are the first two elements of the vector $S$.
- Slide the window to right and then down by steps $P/2$ pixels and repeat the previous step until we have the output vectors of the softmax layer from all video patches.
- Find the center of the patches that their metrics are larger than a threshold $T$.In this research, we set $T = 0.999$ .
- Find the average of the center points computed in the previous step. This average indicate the coordinates of the IJV location.
```

6.5 Results and Discussion

In this section, first, we compare the classification accuracy for the implemented 3D CNNs to select the one with the best performance to employ it with the proposed algorithm.

6.5.1 Classification Accuracy

To calculate the classification accuracy of the implemented 3D CNNs, we first convert the test videos to the video patches using the 3D SW introduced in Section 6.3.1. Table 3 presents the classification accuracy of the implemented 3D CNNs for the video patches acquired from the 17 healthy subjects. Since the majority of the video patches belong to the class "Outside", the results of this class is overwhelming the other two classes and hence, in this table, we individually calculate and present the accuracy of the correct classification for each class. Note that since the performance of the localization algorithm is based on the first two classes, i.e., "Inside" and "Overlap", the accuracy of correct classification as "Outside" is not very important and this information can be ignored.

Table 6.1: The average classification accuracy for the healthy and CHF subjects.

Classes / Models	Inside	Overlap	Outside
C32N10X3	0.0	0.03	0.99
C32N30X3	0.0	0.06	0.99
C64N10X4	0.18	0.63	0.97
C64N15X4	0.19	0.69	0.97
C90N15X5	0.53	0.64	0.97
C90N15X4	**0.88**	**0.94**	0.99
C90N15X6	0.43	0.54	0.96
C119N15X5	0.54	0.63	0.97

From table 6.1, one can see that the best performance is obtained with the C90N15X4 model, while by adding more convolutional layers in the C90N15X5 and C90N15X6 models, the classification accuracy is declining. We can further see that, the performance of the C119N15X5 model is not better than the C90N15X5 model, while due to the larger patch size, its spatial resolution is expected to be worse than the C90N15L5 model. With the C32N10X3 and C32N30X3 models which have the smallest patch size in space dimension, the lowest accuracy is obtained since the information inside the patch is not sufficient, during the training process, the classes "Inside" and "Overlap" are overwhelmed by the class Outside and hence, during the validation, almost all patches are labeled as "Outside" providing an extremely low classification accuracy for the first two classes, and an high accuracy for the class Outside which is not important for us.

6.5.2 Performance of the Proposed Algorithm

As it is seen from the table 6.1, the C90N15X4 model presents the best performance among the studied CNNs, and hence, we build the proposed localization algorithm based on this model, and then compute the accuracy of the algorithm. In this section, we validate the performance of the proposed algorithm using two criteria. The first criterion is "if the result of the algorithm is a point inside IJV?". This is specially important when the algorithm is combined with a semi-automatic algorithm such as the one in [15] to form a fully automatic segmentation algorithm as the algorithm in [15] only needs a seed point inside the IJV. Furthermore, this result helps operators to find the location of the IJV in extremely low quality ultrasound video, where the IJV is hardly visible. The second criterion that we define here is the distance between the result of the algorithm and the center of the IJV manually located by expert. For each case, the center of the IJV was manually located by the an expert. Since there are no prior works on this subject and the prior algorithm is the first automatic algorithm to localize the IJV, in this section, there is not comparison with other algorithms. Table 6.2 indicates the result obtained from 12 randomly selected videos, six from the healthy subjects and six from the CHF patients. Note that the data from the healthy subjects is different from the ones used for training. From Table 6.2, one can see

Table 6.2: The average classification accuracy metric for the healthy and CHF subjects.

Metrics / Subject no.	Is inside?	Distance (mm)
1	yes	2
2	yes	1.2
3	yes	1.8
4	yes	0.9
5	yes	2.2
6	yes	2.3
7	yes	1.9
8	yes	3.8
9	no	33
10	yes	2.9
11	yes	1.8
12	yes	1.5

that with the data from the healthy subjects a slightly better performance is achieved and it is mainly because the CNNs have been trained with the data from the healthy subjects that is expected to follow the similar patterns with the test data, although the test and training data are from different subjects. In overall, in 94 percent of the healthy subjects, the result of the algorithm was a point inside the IJV while for the CHF patients is ratio was 0.91 percent. Furthermore, for the correctly located case, the average distance between the automatically detected point and center point manually located by an expert, for healthy subject and CHF patients was 1.81mm and 1.92mm, respectively. Fig. 6.12 shows the result of the algorithm for the patches depicted in Figs. 6.7-6.9. In this figure, the green rectangles are showing the patches that their metrics have exceeded the threshold, the yellow circle is the result of the algorithm which is a point inside the IJV, and the red cross is the center of the IJV manually located by the expert. Note that although the size of IJV for this case is smaller than the patch size, but since the window has been shifted by 45 pixels, the IJV has never fallen in the class "Inside" and therefore, only the metrics obtained for two patches from the class "Overlap" have exceeded the threshold. From this figure, one can see that the center of the IJV manually located by the expert is very close to the point located by the algorithm. Note that this is a very difficult case as even an expert needs to watch the entire video multiple times and consider the relative position of the carotid artery[1] to discriminate the IJV from the other tissues that have similar motion patterns as the IJV. Fig. 6.13 shows the result of the algorithm for a healthy subject with a collapsed IJV. From this figure, one can see that for this case, the metrics for the eight patches have exceeded the threshold and hence, even a more accurate result has been obtained. Fig. 6.14 shows the result of the algorithm for a healthy subject with a round IJV shape. From this figure, one can see that, the

---

[1] Carotid artery always has a circular shape and it is expected to be close to the IJV

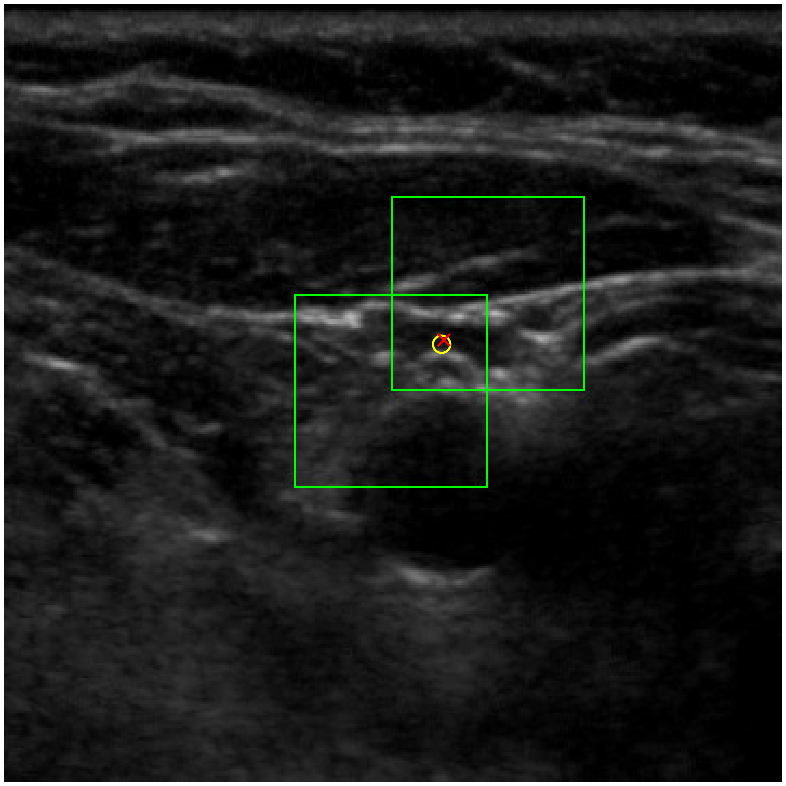

Figure 6.12: The results of the proposed algorithm for the video captured from a the CHF patient in standing position.

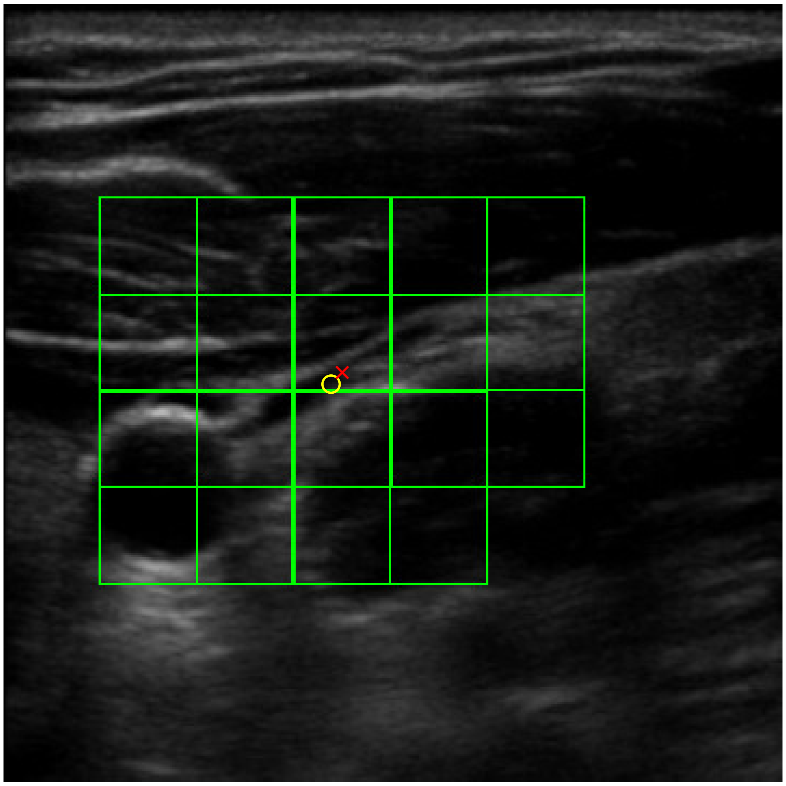

Figure 6.13: The results of the proposed algorithm for a healthy subject with collapsed IJV.

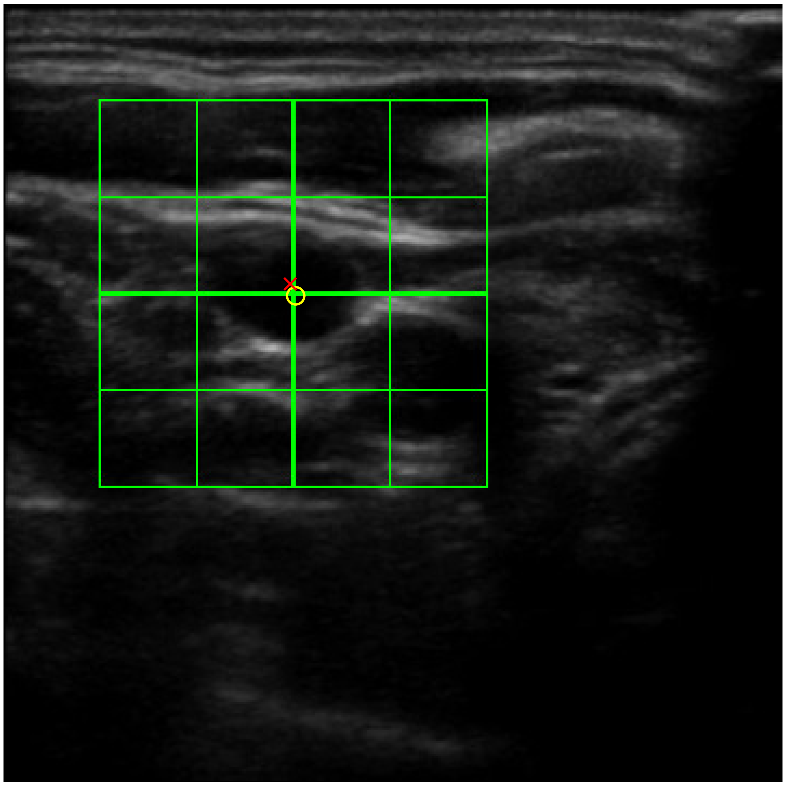

Figure 6.14: The results of the proposed algorithm for the video captured from a healthy subject with a round IJV shape.

metrics for nine patches have exceeded the threshold and the result of the algorithm is so close to the center of the IJV. Fig. 6.15 shows the result of the algorithm for a healthy subject where the IJV contour is partially missing (the part between the IJV and the carotid artery). From this figure, one can see that, the metrics for ten patches have exceeded the threshold. For this case, although the located point is inside the IJV, the distance between the point located by the algorithm and the center of the IJV is larger than previous cases. Fig. 6.16 shows the result for a case when the algorithm fails to localize the point inside the IJV. This case belong to a

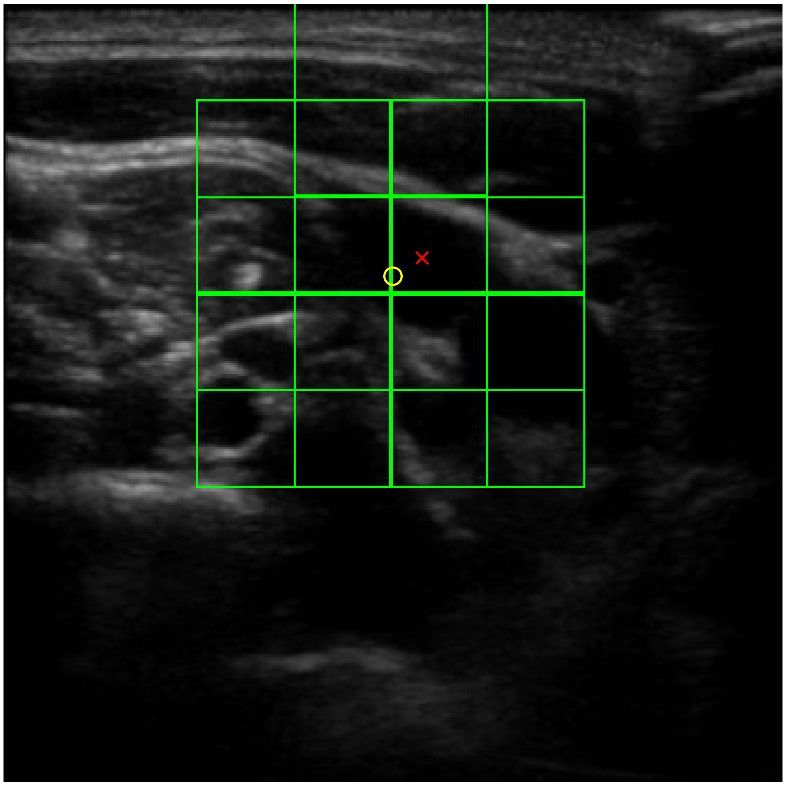

Figure 6.15: The results of the proposed algorithm for the video captured from a healthy subject with a the IJV with partially missing edges.

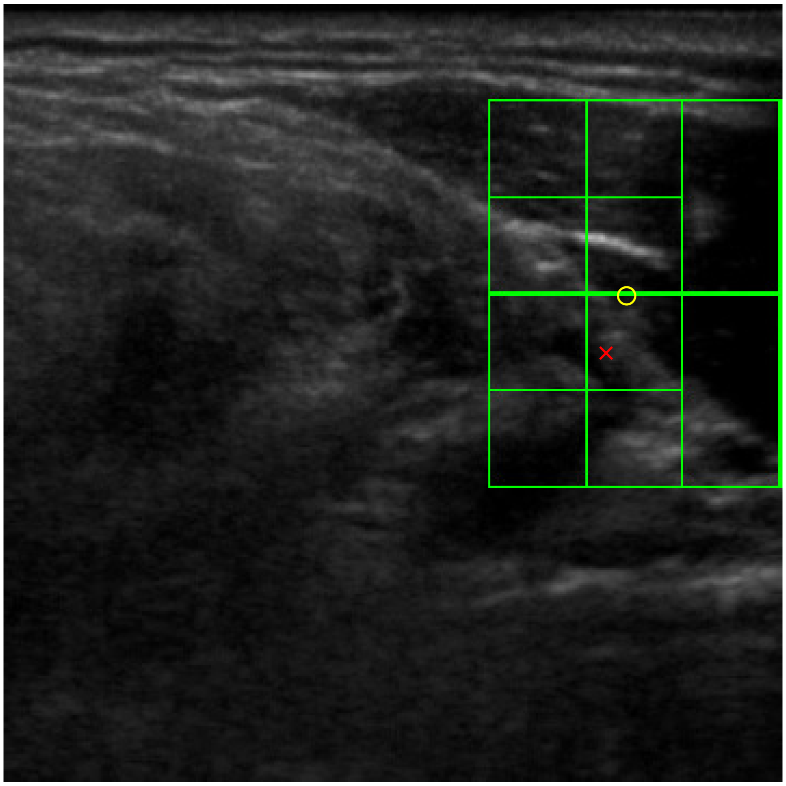

Figure 6.16: The results of the proposed algorithm for the video captured from a the CHF patient in standing position. In this case, the quality of the image is extremely low as even the point manually located by the expert is not for certain.

CHF patients in standing position, and as it is seen from the figure, the quality of the image is extremely low as not only the IJV, but also even the carotid artery is not seen in the image and the point located by the expert is not for certain. In overall, figures 6.12-6.16 show that even in the case of failure the point located by the proposed algorithm is always very close to the one manually located by the expert. Note that in these figures, we have shifted the window as 45 pixels in x and y dimensions to avoid confusion from having too many overlapped windows. However, it is obvious that by decreasing the steps that the window is shifted, the accuracy of the algorithm is improved because by detecting more patches from the classes Inside, and Overlap, a better resolution is obtained.

6.6 Conclusion and Future Work

In this Chapter, a novel algorithm is proposed for automatic localization of the internal jugular vein (IJV) in ultrasound videos. In the proposed algorithm, first a trained convolutional neural network (CNN) is used to detect if each part of the image fall into either of the three classes as , Inside, Overlap, and Outside. These labels show that if the IJV is entirely inside the IJV, has overlap with it, or is entirely outside it. The accuracy of the localization algorithm depends not only on the classification accuracy of the CNN, but also on the video patch size. After training CNNs with different input sizes, we obtained the best accuracy with input video patch size $90 \times 90 \times 15$, where 90×90 is each patch size, and 15 is the number of frames where the video patch has been extracted from them. The classes detected from the different parts of the IJV video were further fused to find a point inside the IJV. The proposed algorithm is used for the IJV videos from both healthy subjects and chronic heart failure (CHF) patients and it is shown that although the CNN has been trained for the data from healthy subjects, the algorithm still performs accurate for the videos captured from the CHF patients.

For the future work, we intend to use a more advanced fusion method by weighting the labels obtained from different patches and optimization of these weights. Furthermore, we intend to employ a multi-scale CNN to iteratively improve the accuracy of the localization by zooming into the exact location of the IJV.

References

[1] John E Strobeck, Jonathan Feldschuh, and Wayne L Miller. Heart failure outcomes with volume-guided management. *JACC: Heart Failure*, 6(11):940–948, 2018.

[2] Frank Bremer, Albert Schiele, Jan Sagkob, Thomas Palmaers, and Klaus Tschaikowsky. Perioperative monitoring of circulating and central blood volume in cardiac surgery by pulse dye densitometry. *Intensive Care Med Intensive Care Medicine*, 30(11):2053–2059, 2004. doi: 10.1007/s00134-004-2445-8.

[3] M. Yashiro, Y. Hamada, H. Matsushima, and E. Muso. Estimation of filtration coefficients and circulating plasma volume by continuously monitoring hematocrit during hemodialysis. *Blood Purif Blood Purification*, 20(6):569–576, 2003. doi: 10.1159/000066957.

[4] Robert R Steuer, David H Harris, and James M Conis. A new optical technique for monitoring hematocrit and circulating blood volume: Its application in renal dialysis. *Dialysis & transplantation*, 22(5):260–265, 1993.

[5] Tadashi Kudo, Shigeharu Suzuki, and Takashi Iwabuehi. Importance of monitoring the circulating blood volume in patients with cerebral vasospasm after subarachnoid hemorrhage. *Neurosurgery*, 9(5):514–520, 1981. doi: 10.1227/00006123-198111000-00004.

[6] H. Kasuya, H. Onda, T. Yoneyama, T. Sasaki, and T. Hori. Bedside monitoring of circulating blood volume after subarachnoid hemorrhage. *Stroke*, 34(4):956–960, 2003. doi: 10.1161/01.str.0000064321.10700.63.

[7] PW De Leeuw and A Dees. Fluid homeostasis in chronic obstructive lung disease. *European Respiratory Journal*, 22(46 suppl):33s–40s, 2003.

[8] Lakshmi Durairaj and Gregory A Schmidt. Fluid therapy in resuscitated sepsis: less is more. *Chest Journal*, 133(1):252–263, 2008.

[9] Cyril Charron, Vincent Caille, Francois Jardin, and Antoine Vieillard-Baron. Echocardiographic measurement of fluid responsiveness. *Current opinion in critical care*, 12(3):249–254, 2006.

[10] J. Kevin Bailey, John Mccall, Suzanne Smith, and Richard J. Kagan. Correlation of internal jugular vein/common carotid artery ratio to central venous pressure. *Journal of Burn Care & Research*, 33(1):89–92, 2012. doi: 10.1097/bcr.0b013e318234d965.

[11] Kasana Raksamani, Vachira Udompornmongkol, Suwannee Suraseranivongse, Manee Raksakietisak, and Benno Von Bormann. Correlation between cross-sectional area of the internal jugular vein and central venous pressure. *European Journal of Anaesthesiology*, 31(1):50–51, 2014. doi: 10.1097/eja.0b013e32835f9a50.

[12] Ebrahim Karami, Mohamed Shehata, and Andrew Smith. Semi-automatic algorithms for estimation and tracking of ap-diameter of the ivc in ultrasound images. *Journal of Imaging*, 5(1):1–14, 2019.

[13] Ebrahim Karami, Mohamed Shehata, and Andrew Smith. Estimation and tracking of ap-diameter of the inferior vena cava in ultrasound images using a novel active circle algorithm. *Computers in Biology and Medicine*, 98:16–25, 2018.

[14] E Karami, M Shehata, and A Smith. Segmentation and tracking of inferior vena cava in ultrasound images using a novel polar active contour algorithm. In *5th IEEE Global Conference on Signal and Information Processing, GlobalSIP2017*, pages 1–5. IEEE, 2017.

[15] E Karami, M Shehata, P McGuire, and A Smith. A semi-automated technique for internal jugular vein segmentation in ultrasound images using active contours. In *2016 IEEE-EMBS International Conference on Biomedical and Health Informatics (BHI)*, pages 184–187. IEEE, 2016.

[16] Konstantinos K Delibasis, Aristides I Kechriniotis, C Tsonos, and Nicholas Assimakis. Automatic model-based tracing algorithm for vessel segmentation and diameter estimation. *Computer methods and programs in biomedicine*, 100(2): 108–122, 2010.

[17] Ebrahim Karami, Mohamed S Shehata, and Andrew Smith. Tracking of the internal jugular vein in ultrasound images using optical flow. In *The 30th Annual IEEE Canadian Conference on Electrical and Computer Engineering (CCECE), Windsor, Canada*, pages 1–4. IEEE, 2017.

[18] Ebrahim Karami, Mohamed Shehata, and Andrew Smith. Ultrasound image segmentation techniques for tracking and measurement of the internal jugular vein. In *The 24th Annual Newfoundland Electrical and Computer Engineering Conference (NECEC), St. John's, Canada*, 2015.

[19] Ebrahim Karami, Mohamed S Shehata, and Andrew Smith. Adaptive polar active contour for segmentation and tracking in ultrasound videos. *IEEE Transactions on Circuits and Systems for Video Technology*, 2018. doi: 10.1109/TCSVT.2018.2818072.

[20] Kun Qian, Takehiro Ando, Kensuke Nakamura, Hongen Liao, Etsuko Kobayashi, Naoki Yahagi, and Ichiro Sakuma. Ultrasound imaging method for internal jugular vein measurement and estimation of circulating blood volume. *International journal of computer assisted radiology and surgery*, 9(2):231–239, 2014.

[21] Jonathan Long, Evan Shelhamer, and Trevor Darrell. Fully convolutional networks for semantic segmentation. In *Proceedings of the IEEE conference on computer vision and pattern recognition*, pages 3431–3440, 2015.

[22] Timothy Dozat. Incorporating nesterov momentum into adam. 2016.

Chapter 7

Overall Conclusions

In this dissertation, two image processing problems in conjunction with estimation and monitoring of circulating blood volume were addressed. In Chapter 2, a novel energy functional was proposed for segmentation of ultrasound images. The proposed functional is based on the third centralized moments that can efficiently separate speckle patterns reflected from different body tissues and hence, represents an efficient algorithm for processing ultrasound images and outperforms existing functionals that are traditional used with active contours.

In Chapter 3, a novel active circle algorithm was proposed for estimation and tracking the AP-diameter of the IVC. It was shown that the actual AP-diameter can be accurately modelled as the diameter of a circle fitted inside the IVC. The parameters of the active circle are automatically evolved based on a novel evolution functional. The results show that the proposed active circle algorithm performs very close to the AP-diameter manually measured by an expert.

The main problem with the active circle algorithm proposed in Chapter 3 is that the IVC AP-diameter is clinically defined as the largest vertical diameter of the IVC contour which deviates from its actual value. To overcome this problem and estimate the AP-diameter in the same way as its clinical definition, in Chapter 4, we proposed an active rectangle algorithm, where the clinically measured AP-diameter is modeled as the height of a thin vertical rectangle. The results showed that the AP-diameter estimated by the active rectangle algorithm is closer to its clinically measured value than the one estimated by the active circle and active ellipse algorithms

In Chapter 5, we propose a novel adaptive polar active contour (Ad-PAC) algorithm for the segmentation and tracking of the IJV in ultrasound videos. In the proposed algorithm, the parameters of the Ad-PAC algorithm are adapted based on the results of segmentation in previous frames. The Ad-PAC algorithm is applied to 65 ultrasound videos and shown that it significantly improves segmentation performance compared to existing segmentation algorithms.

In Chapter 6, we proposed a novel algorithm to automatically locate the vessel in ultrasound videos. The proposed algorithm is based on convolutional neural networks (CNNs) and is trained and applied for IJV videos. In this Chapter we show that although the proposed algorithm is trained for the data acquired from the healthy subjects, it can work for the data collected from coronary heart failure (CHF) patients without additional training.